

DESIGN AND SIMULATION OF A UHF BAND RADIO FREQUENCY  
QUADRUPOLE (RFQ) PROTON ACCELERATOR

by

Emre Çelebi

B.S., Physics, Boğaziçi University, 2012

M.S., Physics, Boğaziçi University, 2016

Submitted to the Institute for Graduate Studies in  
Science and Engineering in partial fulfillment of  
the requirements for the degree of  
Doctor of Philosophy

Graduate Program in Physics

Boğaziçi University

2023

## ACKNOWLEDGEMENTS

First of all, I would like to thank my thesis advisors Prof. Dr. Veysi Erkcan ÖZCAN and Assoc. Prof. Dr. Gökhan ÜNEL. Their wisdom, guidance, and patience allowed me to surpass many challenges I have presented with this work.

I can't thank enough my family, especially my parents Mevlidiye ÇELEBİ, Hayrullah ÇELEBİ, and my sister Elif ÇELEBİ for their love, care, and support.

I would like to thank my beloved girlfriend Ebru NAYİR. With her no conversation is mundane and no difficulty is insurmountable.

I would like to express my gratitude to the research assistants at Istanbul Bilgi University. They may be my former coworkers but they shall be my friend for the rest of the days.

The language used in this thesis has been improved using Generative Pre-trained Transformer(GPT) and Grammarly. I would like to thank the developers of these pieces of software.

I also can't thank enough Aytül ADIGÜZEL for her support and her friendship.

I would like to thank TÜBİTAK (The Scientific and Technological Research Council of Türkiye) for partially supporting the work presented in this thesis through projects 118E838 and 117F143.

Lastly, I wouldn't be exaggerating if I call KahveLAB a second home. I am proud to be a member of this awesome lab filled with amazing people.

## ABSTRACT

# DESIGN AND SIMULATION OF A UHF BAND RADIO FREQUENCY QUADRUPOLE (RFQ) PROTON ACCELERATOR

This thesis introduces DemirciPro, a computer program created to design and simulate low-energy beamlines, along with the UHF band radio frequency quadrupole (RFQ) designed as part of the Proton Testbeam At Kandilli (PTAK) project. The RFQ has undergone trial production and measurements, and this thesis documents its results.

DemirciPro is a computer program that is developed within KahveLAB. DemirciPro strives to design low-energy beamlines with a single robust interface. It simulates all the critical elements of a low-current beamline except for the ion source. Moreover, DemirciPro has the potential to govern other design and simulation codes using a single interface, thereby enabling the simulation of the whole beamline using industry-standard programs.

In this thesis, we provide a brief overview of the Proton Testbeam At Kandilli (PTAK) project, including the current test results of its components. We then delve into the details of RFQ, including its original RFQ vane-tip design and the novel design approach followed. We also present the findings of the completed trial production over the past years. Lastly, we compare the vane-tip measurements of test production with the design and discuss the effects of production errors on the simulation results.

## ÖZET

# BİR UHF BANDI RADYO FREKANS DÖRT KUTUPLUSU TASARIM VE BENZETİMİ

Bu çalışmada düşük enerji demet hattı tasarım ve benzetimi için geliştirdiğimiz bilgisayar programı DemirciPro ve Proton Testbeam At Kandilli (PTAK) projesi bünyesinde tasarlanan, deneme üretim ve ölçümleri tamamlanan UHF bandı radyo frekans dört kutuplusuna (RFQ) yer verilmiştir.

DemirciPro KahveLAB bünyesinde geliştirilmektedir. Bu bilgisayar programının genel özellikleri, güncel versiyonunda sahip olduğu yetileri ile birlikte sunulmuştur. DemirciPro, düşük enerji demet hattının tek arayüz ile tasarlanmasını hataya mahal vermeden sağlamayı hedefler. Düşük akımda çalışan bir demet hattı için iyon kaynağı hariç, bütün demet hattı elemanlarının benzetimini bünyesinde barındırır. Tasarım ve benzetim için kullanılan diğer programlarla yine tek bir arayüz ile etkileşerek bütün hattın benzetiminin endüstri standardı programlarla tekrarlanmasını sağlayabilmektedir.

Ayrıca PTAK projesi kısaca tanıtılmış olup, RFQ haricindeki elemanlarının güncel test sonuçlarına değinilmiştir. Bunun ile birlikte RFQ detaylı tanıtılmış, özgün kanat ucu tasarımı ve bu tasarıma ulaşma metodu detaylı anlatılmıştır. Geçen yıllarda tamamlanan deneme üretimine dair bulgular sunulmuş, üretim tasarımıyla karşılaştırılmış ve üretim hatalarının sonuçlara etkisi tartışılmıştır.

## TABLE OF CONTENTS

ACKNOWLEDGEMENTS . . . . .	iii
ABSTRACT . . . . .	iv
ÖZET . . . . .	v
LIST OF FIGURES . . . . .	ix
LIST OF TABLES . . . . .	xix
LIST OF SYMBOLS . . . . .	xx
LIST OF ACRONYMS/ABBREVIATIONS . . . . .	xxiii
1. RADIO FREQUENCY QUADRUPOLE ACCELERATORS . . . . .	2
1.1. History of Radio Frequency Quadrupoles . . . . .	2
1.2. RFQs in Turkey . . . . .	3
1.3. RFQ Operating RF Mode . . . . .	4
1.4. Parameters Describing a RFQ Cell . . . . .	5
1.5. Two Term Potential and Eight Term Potential . . . . .	7
1.6. LANL RFQ Design Schema . . . . .	11
1.6.1. Radial Matching Section . . . . .	12
1.6.2. Shaper Section . . . . .	12
1.6.3. Gentle Buncher Section . . . . .	12
1.6.4. Acceleration Section . . . . .	13
2. INTRODUCTION TO THE FINITE ELEMENT METHOD . . . . .	14
2.1. Galerkin Method . . . . .	14
2.1.1. Relaxed Form of the Equation . . . . .	16
2.1.2. 20 Node Isoparametric Brick Element . . . . .	18
2.1.3. Assembly of Global Stiffness Matrix and Forcing Boundary Con- ditions . . . . .	22
3. DEMIRCIPRO: A RFQ DESIGN SOFTWARE . . . . .	24
3.1. DemirciPro Features . . . . .	24
3.1.1. Ion Source Design and Simulation Using IBSIMU . . . . .	24
3.1.2. Low Energy Beam Transport (LEBT) Design and Simulation . . . . .	26

3.1.2.1.	Pepper-pot Diagnostic Instrument Design and Simulation . . . . .	28
3.1.3.	RFQ Design and Simulation with DemirciPro . . . . .	30
3.1.3.1.	Calculation of Inter-vane Electric Fields Using Finite Element Method . . . . .	36
3.1.3.2.	Simulation with External Files . . . . .	41
3.2.	The Future of DemirciPro . . . . .	49
4.	PROTON TESTBEAM AT KANDILLI (PTAK) AND 800 MHZ RFQ DESIGN . . . . .	51
4.1.	PTAK-RFQ Design Objectives and Limits . . . . .	52
4.2.	Initial Design with LANL Method . . . . .	54
4.3.	PTAK RFQ Design . . . . .	55
4.3.1.	Our Design Approach . . . . .	56
5.	PTAK TEST MODULE (MODULE-0) MEASUREMENTS . . . . .	60
5.1.	Vacuum Test . . . . .	61
5.2.	Beadpull Measurements . . . . .	61
5.3.	CMM Measurements . . . . .	65
5.3.1.	Comparison of Old and New CMM Measurements . . . . .	73
5.3.2.	Laser Scanner Measurements and Their Comparison to CMM Method . . . . .	76
5.4.	Visual Inspection of The Machined Parts . . . . .	79
5.4.1.	Initial Tests on an Advanced Microscope with Precise Motorized Stage . . . . .	79
5.4.2.	Tests with Stereo Microscope . . . . .	82
5.4.3.	Tests with a DIY Microscope . . . . .	84
6.	800 MHZ RFQ DESIGN ERROR STUDIES AND EFFECT OF CAVITY SURFACE ROUGHNESS ON CAVITY MODES . . . . .	89
6.1.	Error Studies . . . . .	89
6.1.1.	Vane Voltage, Frequency, and Input Beam Energy . . . . .	90
6.1.2.	Beam Dynamics Simulation with Machining Errors . . . . .	92
6.2.	Surface Roughness . . . . .	92

6.3. Progress on Module-1 and Module-2 . . . . .	94
7. CONCLUSION . . . . .	95
REFERENCES . . . . .	96
APPENDIX A: 20-NODE ISOPARAMETRIC BRICK INTERPOLATION FUNCTIONS . . . . .	101
APPENDIX A: PERMISSION OF FIGURES . . . . .	103

## LIST OF FIGURES

Figure 1.1.	The electrodes of both rod and vane types are depicted with some exaggeration along with their respective positions inside their RF cavities. . . . .	4
Figure 1.2.	Figure depicting comparison between a cylindrical cavity operating at the $TE_{21}$ mode and a cavity with vanes. . . . .	5
Figure 1.3.	Parameters that define a RFQ cell. . . . .	6
Figure 2.1.	The transformation from natural coordinates $(\xi, \eta, \zeta)$ . . . . .	18
Figure 2.2.	A depiction of a shared boundary for two adjacent elements. . . . .	20
Figure 3.1.	At the top: DemirciPro IBSIMU integration is shown as the design parameters, resulting in geometry with chosen electrodes and the IBSIMU simulation result being conveniently presented. At the bottom: The electrode setup pop-up window is shown with individual electrode geometry settings. . . . .	25
Figure 3.2.	Magnet design interface for Poisson-Superfish simulation input files. On the left solenoid, on the right quadrupole magnet parameters are presented. . . . .	27
Figure 3.3.	On the top: DemirciPro LEBT design and simulation interface is shown. For a test design, parameters, resulting geometry, and the DemirciPro simulation results can be seen together. A comparison of the LEBT simulation results obtained from DemirciPro and TRAVEL is presented on the bottom. . . . .	27

Figure 3.4.	DemirciPro pepper pot design, simulation & measurement interface. . . . .	29
Figure 3.5.	DemirciPro pepper pot measurement results. On the left, beamlet distributions zoomed to a particular region. On the center, the central region of beamlet distributions overlaid with fitted Gaussian function. On the right, red values show the truth information, whereas the blue values show measured values. . . . .	29
Figure 3.6.	DemirciPro's main page for RFQ design is shown with plot functionality and configuration window of this plot. The user can quickly adjust the interpolation points and see their effect on various parameters. . . . .	30
Figure 3.7.	DemirciPro internals window. . . . .	31
Figure 3.8.	DemirciPro's Superfish input interface. . . . .	32
Figure 3.9.	Interface for drawing RFQ vanes. . . . .	33
Figure 3.10.	3D view of the RFQ vanes . . . . .	33
Figure 3.11.	DemirciPro beam-dynamics tab. . . . .	34
Figure 3.12.	3D representation of the particles with DemirciPro. . . . .	35
Figure 3.13.	The solution of the toy problem. . . . .	36
Figure 3.14.	Quarter of RFQ cell has meshed with 20 node brick elements in a regular fashion. The nodes are not shown in this figure. . . . .	37

Figure 3.15. A cell mesh connection matrix with zero-valued matrix elements is shown with black pixels, and others are represented with white pixels. . . . .	38
Figure 3.16. Algorithm for conjugate gradient (CG) method. . . . .	39
Figure 3.17. The difference between DemirciPro and CST potential calculation results for a test cell (Cell 180 from Table 3.1) is plotted as a histogram. The voltage difference between vanes is 200 Volts, yet CST and DemirciPro results differ by less than 0.2 volts apart from a few data points. . . . .	40
Figure 3.18. Difference between interpolation and 8TP divided with the 8TP. The relative errors of tri-linear(black line) and tri-cubic interpolation (red line) are presented together. The relative errors with absolute values larger than 0.2 were discarded, as most of these stem from sample points with 8TP values close to zero. (The imported file has 1 mm separation between data points.) . . . . .	43
Figure 3.19. $z, x$ projection of the coordinates with $E_z$ error greater than 0.00002 kV/mm for tri-linear method (black upper triangles) and tri-cubic method (red lower triangles). . . . .	45
Figure 3.20. $x, y$ projection of the coordinates with $E_z$ error greater than 0.00002 kV/mm for tri-linear method (black upper triangles) and tri-cubic method (red lower triangles). . . . .	46
Figure 3.21. The sampled area in $x - y$ plane depicted in middle of a cell with dotted square. Test geometry is a 352 MHz RFQ, designed with LANL method. . . . .	47

Figure 3.22.	The CST simulation of the PTAK RFQ provided the electric field values $E_x$ , $E_y$ , and $E_z$ . These values are presented in the x-y cross-sections at a distance of 2 mm from the beginning of the RFQ where $m=1$ . Inter-vane voltage difference is 33 kV. . . . .	47
Figure 3.23.	CST simulation results with different meshing strategies compared.	48
Figure 3.24.	$E_y$ values for $x = 0$ mm plotted. For both types of meshing, the center seems to be placed to $x = 0$ mm, $y = -0.0355$ mm. . . . .	48
Figure 4.1.	PTAK beam line with virtually added RFQ. . . . .	51
Figure 4.2.	PTAK Microwave Discharge Ion Source design . . . . .	52
Figure 4.3.	SF representation of Quarter RFQ crossection. . . . .	53
Figure 4.4.	Power per meter & Vane voltage comparison. . . . .	54
Figure 4.5.	PARMTEQM simulation result for the minimum design. The total length of this design was roughly 92 cm. . . . .	55
Figure 4.6.	On the left, the problem at hand is depicted. On the right, the method of tackling the problem is presented. Red dots represent the upper limit for modulation ( $m$ ) values that are taken from the minimum design. . . . .	56
Figure 4.7.	One of the first promising results where the 24% of the particles were accelerated. The total length was roughly 1 meter and the intervane voltage was 35 kV. . . . .	57

Figure 4.8.	The particle simulation results are plotted on the top, and the design parameters are presented in the bottom graph. In the final design, the total length is roughly 98cm. In addition, 30% of particles are accelerated, and the estimated power usage is 58 kW . . .	58
Figure 4.9.	A parameter view from DemirciPRO . . . . .	59
Figure 5.1.	The 3D o-ring and its placement in the RFQ are presented on the left, and a picture from the vacuum test is presented on the right.	61
Figure 5.2.	The pins and parts were added to the RFQ body to achieve repeatable relative positioning presented. These pins and holes were produced with tight tolerances, and hole positions were determined after vane alignment. . . . .	62
Figure 5.3.	Solder wire was used instead of RF seal. . . . .	63
Figure 5.4.	Experimental setup for bead pull measurement . . . . .	64
Figure 5.5.	On the left bead pull measurements, on the right Calculated Quadrupole (bold yellow) and Dipole (bold red and bold blue) moments along the $z$ -axis . . . . .	64
Figure 5.6.	Blue lines are the design vane tip coordinates, whereas the red lines are the CMM measurements for the top vane after a fit performed with $F_{shifted}(z, a, b)$ function. We brought the measurement and design values into the same coordinate system by performing this fit . . . . .	65

- Figure 5.7. Blue lines are the design values for vane tip coordinates. In red we are displaying the difference of measurement from this design values which corresponds to machining errors of the top vane tip. . . . . 66
- Figure 5.8. Blue lines are the design values for vane tip coordinates. In red we are displaying the difference of measurement from this design values which corresponds to machining errors of the corresponding vane. . . . . 66
- Figure 5.9. The figure shows how errors in machining vary when we consider the first and second derivatives of the vane with respect to its position along the z-axis. The vane tip coordinates are approximated using a cubic spline then the derivatives are calculated. The relationship between the machining errors changes with both orders of derivatives in a complex manner, as shown in these figures. . . . . 67
- Figure 5.10. Top: Mean values of Machining Errors on the Grid vs. Derivatives. Bottom: 3D representation of the prediction surface constructed from the top plot. . . . . 68
- Figure 5.11. Standard deviation values of Machining Errors on the Grid vs. Derivatives. . . . . 69
- Figure 5.12. Count values of Machining Errors on the Grid vs. Derivatives. . . . . 69
- Figure 5.13. Left: Top vane errors and errors after prediction subtracted from measurement overlaid together. Right: Error Histograms from before and after prediction subtraction are shown separately. . . . . 70

Figure 5.14. From top to bottom: Left, bottom, right vane machining errors displayed before and after prediction constructed with top vane data. The improvement is marginal, if it exists at all. These results suggest that the behavior of errors is different between vanes; therefore, the production process is not identical. . . . . 71

Figure 5.15. Difference of top and bottom CMM measurements after both fitted on the design values of the vane displayed. There are periodic and bowing-like behavior present. . . . . 72

Figure 5.16. Difference of right and left CMM measurements after both fitted on the design values of the vane displayed. There are periodic and bowing-like behavior present. . . . . 72

Figure 5.17. In blue, ideal vane geometry is represented, and in red, the difference between old and new CMM measurements is displayed. Notice the plot labeled bottom vane has some large periodic differences around 0.2 meters . . . . . 74

Figure 5.18. Bottom vane plot zoomed around 0.2 meters. . . . . 74

Figure 5.19. On the left column, errors are presented with blue, high-pass filtered errors with red, and low-pass filtered values represented with black for each vane. On the right column, error and high-pass filtered error values are histogrammed for each vane. . . . . 75

Figure 5.20. 3D laser scan process. . . . . 76

Figure 5.21. Cloud Compare software result on full part geometry. Colors represent the distance to the design surface. . . . . 77

- Figure 5.22. The successive selection of surfaces used in the fit procedure is presented. In the top two plots, blue areas indicate that the measurement result falls within the reference geometry, and red areas indicate that the result falls outside the reference geometry. In the final stage, the data points selected for further error analysis are shown in the bottom figure. . . . . 78
- Figure 5.23. Difference of Laser scan with CMM measurements shows that the resolution of the Laser scan is worse than 100 microns. . . . . 78
- Figure 5.24. Sample part placed on a motorized microscope stage. . . . . 79
- Figure 5.25. Reflection and transmission microscopy images. In the reflection mode, the best images are obtained when the surface in the focused plane is parallel to it. Transmission mode excels at the very tip, yet there is no other useful information can be received. . . . . 80
- Figure 5.26. One example image is when the focus plane lowered to the tip region. As one might observe, only a small part of the surface is in focus, and the rest of the image is not sharp at all. In the bottom left, grey values from a row of pixels (marked with a white line) are graphed. . . . . 80
- Figure 5.27. The difference in the stage height is 0.550 mm compared to the image presented in figure 5.26. . . . . 81
- Figure 5.28. Points that are selected from each image stacked together. . . . . 81
- Figure 5.29. The 3D image in the Figure 5.28 when the underlying images cleaned with erosion method. . . . . 82

Figure 5.30. Stereo microscope setup: Left ocular of the Olympus SX30 microscope was removed, and the PS3 webcam sensor (optics are removed) was placed in its place (wrapped in aluminum foil so that we can protect the sensor from stray light). Images acquired via a script. A laser pointer is aligned on the left ocular so that focused laser light can be seen in the image (not shown here). . . . .	83
Figure 5.31. Image acquired in 4x mode of the microscope. Laser light and the machining marks on the vane tip can be observed. We tested if we could use a laser to assess whether the region of interest was in focus quickly. . . . .	83
Figure 5.32. Same image as Figure 5.31 but the white light source is turned off.	84
Figure 5.33. DIY camera adaptor for microscope objective. . . . .	85
Figure 5.34. A human hair image taken with the DIY microscope. . . . .	85
Figure 5.35. An image of a straight region on the part. The image shows that straight parts are manufactured with very little surface irregularities compared to vane tips . . . . .	86
Figure 5.36. An image from the vane tip where the center of the image is sharply focused. . . . .	86
Figure 5.37. An image from the vane tip where the center of the image is not properly focused. . . . .	87
Figure 5.38. An image from the vane tip where the right top of the image is in focus. . . . .	87

Figure 6.1.	Toutatis calculation of the PTAK RFQ sync-phase value with respect to $z$ presented with the blue line. The PARMTEQM results are presented with the red line. We suspect that the discrepancy between PARMTEQM and Toutatis sync-phase calculation makes Toutatis lose track of accelerated particles. . . . .	89
Figure 6.2.	On the left column, acceleration percent versus inter-vane voltage is presented. In the middle column, acceleration percent versus input beam energy is presented. In the right column, acceleration percent versus operating frequency and output beam energy versus operating frequency are shown together. . . . .	90
Figure 6.3.	Acceleration percent vs. input current . . . . .	91
Figure 6.4.	Current of accelerated particles vs. input current . . . . .	91
Figure 6.5.	Frequency shift of fundamental modes induced by surface roughness . . . . .	93
Figure 6.6.	Quality factor change of fundamental modes induced by surface roughness. . . . .	93
Figure 6.7.	In this picture, both OFC parts and aluminum dummies are presented in their current state. . . . .	94

## LIST OF TABLES

Table 2.1.	Element nodes and their coordinates in natural coordinate system.	22
Table 3.1.	Definitions of the RFQ cells used for comparison. Minimum bore radius and cell length are in cm. . . . .	41
Table 3.2.	Comparison of the multipole coefficients calculated by available software. The errors ( $\epsilon_{tot}$ ) are always calculated relative to CHRG3D except for DEMIRCI, which also reports relative to PARMTEQM in parentheses. . . . .	42
Table 5.1.	The ratio of errors with an absolute value less than 10 micrometers to all is tabulated for unfiltered errors, and the errors after the high pass filter is applied. . . . .	76
Table 6.1.	Comparison of Toutatis simulation results in Ideal geometry vs. machining errors present in the first half of ideal geometry. In this table, results presented without scaling . . . . .	92

## LIST OF SYMBOLS

$A$	Acceleration efficiency
$A_i$	Element stiffness matrix
$A_{jk}^i$	Element stiffness matrix components
$A_n$	The multi-pole terms for RMS
$A_{nm}$	The multi-pole coefficients
$a$	Minimum bore radius for the RFQ cell
$B$	Focusing strength
$B_z$	Magnetic field in beam direction
$B_r$	Radial component of magnetic field
$b_k^i$	Boundary condition terms for i-th element, where the $k$ indicate node indices
$\vec{b}_i$	Vector form of the $b_k^i$
$C$	Connection matrix
$C_{mn}$	RFQCOEF's naming convention for 8TP coefficients
$c$	Speed of light
$D_i, D_j, D_k$	Number of nodes used in a mesh construction.
$\vec{E}$	The time-independent part of the electric field.
$E_0$	where the average peak axial accelerating field
$E_x, E_y, E_z$	Cartesian components of the electric field.
$F(z)$	Interpolated function of the CMM results.
$F_{shifted}(z, a, b)$	Interpolated function of the CMM results with shift
$F_{shift,tilt}(z, a, b, c)$	Interpolated function of the CMM results with shift and tilt
$f$	Frequency
$f_\Omega$	Small longitudinal oscillation frequency
$I_{2m}$	Modified Bessel function of order $2m$
$i_{global}$	Global index
$i$	Element index
$i_{element}$	Node index in an element

$k$	Wave parameter
$k_{rms}$	Wave parameter for RFQ radial matching section
$l_{cell}$	Length of a RFQ cell
$L$	Length of the RMS section
$M$	The mass of a macro-particle
$m$	Modulation parameter of the RFQ cell
$m_0$	Rest mass of the particle
$N_j$	Interpolation function
$N_j(\xi, \eta, \zeta)$	$j$ -th node's interpolation function in natural coordinates
$n_c$	Number of nodes on the imaginary line between electrodes
$n_e$	Number of nodes along the electrode surface
$n_z$	Number of nodes in $z$ direction
$p$	Total number of nodes in the global FEM problem
$Q$	Charge of the macro-particle
$q$	Charge of the ion
$r$	Radial position in cylindrical coordinates
$r_0$	Mean aperture of the vanes
$r^i$	Weighted residual for $i$ -th element
$T$	Transit-time factor
$TE_{i,j,k}$	Transverse electric mode
$U^i$	Test function
$V(x, y, z)$	Electrostatic potential
$V_0$	Potential difference of adjacent vanes
$V_e^j$	Value of the solution on the $j$ -th node coordinate.
$W$	Energy of an arbitrary ion in the beam
$W_s$	Synchronous particle energy
$w$	Weight function
$w_k^i$	Weight function of $i$ -th elements $j$ -th node
$x_j^i$	The value of the $i$ -th elements $j$ -th node
$x_j, y_j, z_j$	the node coordinate values in the problem's coordinates
$z_b$	Geometric length of the bunch

$\alpha$	Vane taper angle
$\beta$	The speed of the ion relative to the speed of light.
$\gamma$	Lorentz factor
$\gamma_s$	Lorentz factor of the synchronous particle
$\epsilon_{tot}$	Relative error
$\zeta$	Natural coordinate
$\eta$	Natural coordinate
$\theta$	Angular position in cylindrical coordinates
$\lambda$	RF wavelength in vacuum
$\lambda_\omega$	Small oscillation wavelength in the longitudinal direction
$\xi$	Natural Coordinate
$\rho$	Vane tip radius
$\sigma_0$	phase advance per focusing period for zero current
$\Phi_s$	Seperatrix length
$\phi$	Phase of an arbitrary ion in the beam.
$\phi_{sync}$	Phase of the synchronous particle
$\chi$	Focusing efficiency
$\Omega$	Volume of the problem
$\Omega^i$	Volume of $i$ -th element.
$\omega$	Angular frequency

**LIST OF ACRONYMS/ABBREVIATIONS**

2D	Two Dimensional
3D	Three Dimensional
8TP	Eight Term Potential
AC	Alternating Current
BNCT	Boron-Neutron Capture Therapy
CAD	Computer Aided Design
CLI	Command Line Interface
CMM	Coordinate-Measuring Machine
CNC	Computer Numerical Control
CST	Computer Simulation Technology
DC	Direct Current
DIY	Do It Yourself
DTL	Drift Tube Lineac
FEM	Finite Element Method
FODO	Focus Defocus Lattice
GB	Gentle Buncher
GUI	Graphical User Interface
IS	Ion Source
LANL	Los Alamos National Lab
LEBT	Low Energy Beam Transport
OFC	Oxygen Free Copper
PIXE	Proton-Induced X-ray Emission Analysis
PTAK	Proton Testbeam At Kandilli
RF	Radio Frequency
RFQ	Radio Frequency Quadrupole
RMS	Radial Matching Section
SF	Superfish
SS	Shaper Section

TTP	Two Term Potential
UHF	Ultra High Frequency
USSR	Union of Soviet Socialist Republics
VNA	Vector Network Analyzer
VS	Vane Shape

# 1. RADIO FREQUENCY QUADRUPOLE ACCELERATORS

## 1.1. History of Radio Frequency Quadrupoles

The challenge of focusing the beam at low particle velocities confronted ion linear accelerators (linac) prior to the wide acceptance of radio frequency quadrupoles (RFQ) as pre-accelerators. The magnetic beam optics is ineffective at the low  $\beta$  region since the force exerted on the charged particle in a magnetic field depends on the particle velocity. High-energy linacs, therefore, resorted to accelerating the initial beam to injection energy using a Cockcroft-Walton type DC accelerator for moderate beam currents and emittances. The accelerated beam would be bunched with a radio frequency (RF) buncher to be injected into the following accelerating structure, usually to a drift tube linac (DTL). However, this non-adiabatic buncher could cause an increase in beam emittance due to the space charge effect when the beam rapidly compressed longitudinally [1].

AC quadrupole focusing and beam stability of charged particles traveling inside the quadrupole were investigated by W. Paul and H. Steinwedel before the inception of RFQ accelerators for the quadrupole mass analyzer [2]. The quadrupole electrodes in this device were straight, devoid of any modulation, and no acceleration in the beam direction was present. The device could select ions of a specific charge-to-mass ratio based on the bias voltage, AC voltage magnitude, and frequency. The stability condition was insensitive to ion velocity.

In 1969, Kapchinskiy and Teplyakov (K-T) introduced the concept of the RFQ accelerator in a seminal publication. K-T proposed modulation of the quadrupole electrodes to enable acceleration while maintaining the transverse stability [3]. Additionally, in a separate publication, K-T proposed adiabatic bunching in RFQs [4]. The first experimental RFQ test was conducted in 1974, and a beam of protons accelerated

from 100 keV to 620 keV with roughly 50% transmission efficiency. The input beam current was reported as 200 mA [5].

Los Alamos National Lab (LANL) was the first institution outside the USSR to undertake research on RFQ accelerators. The proof-of-concept experimental setup is detailed in [6], which also introduced the LANL RFQ accelerator design. The design schema incorporated two new sections, namely radial matching and shaper, in addition to the K-T approach. Furthermore, the publication discussed the PARMTEQ (Phase and Radial Motion in Transverse Electric Quadrupoles) code and its results on the experimental design. The first experiments using this design occurred in 1980, with a 30 mA proton beam achieving 87% transmission efficiency, compatible with the PARMTEQ simulation. The input proton energy was 100 keV, and the final energy was 640 keV [7].

As RFQ technology matured, these devices superseded DC injectors in many high-energy linac applications [8]. In addition, they found many uses in medicine and nuclear physics [9]. One remarkable example of the RFQ's versatility and robustness was demonstrated by the BEAR-RFQ (The Beam Experiment Aboard Rocket) that functioned in space and operated successfully in the lab upon return to earth [10]. The RFQ's compactness, ease of operation, and reliability in the stringent conditions of space flight are evident from this impressive feat.

## 1.2. RFQs in Turkey

The Prometheus project in Turkey created the first RFQ (Radio Frequency Quadrupole) that was designed and produced in the country. The goal of this project was to build a 352 MHz RFQ that could produce a 1.5 MeV proton beam while being shorter than 2 meters and having a 99% transmission rate for the input beam [11]. In addition, this project aimed to transfer knowledge to Turkey and provide education in the field of accelerator physics to Turkish students.

Proton Testbeam At Kandilli (PTAK) projects includes the second RFQ that was designed and manufactured in Turkey. The RFQ will operate at 800 MHz, the highest frequency normal conducting RFQs designed for. The PTAK project aims to facilitate a 2 MeV beam proton beam line for particle detectors as well as conduct proton-induced X-ray emission analysis (PIXE) and boron-neutron capture therapy (BNCT). The designs for almost all components have been completed, and the majority of the components have been manufactured, installed, and tested [12]. The first 2 MeV beam measurements are expected to be realized before the end of 2023.

### 1.3. RFQ Operating RF Mode

RFQs are classified into two types based on the electrode geometry. For low-frequency operation and ions of heavy nuclei (i.e., U, Pb), a rod-type RFQ is typically preferred. The RF cavity of this type of RFQ contains four electrodes with varying diameters along the length of the RFQ. Figure 1.1 presents a schematic illustration of rod-type RFQ. The tuning of the electrodes primarily determines the operating frequency of rod-type RFQs.

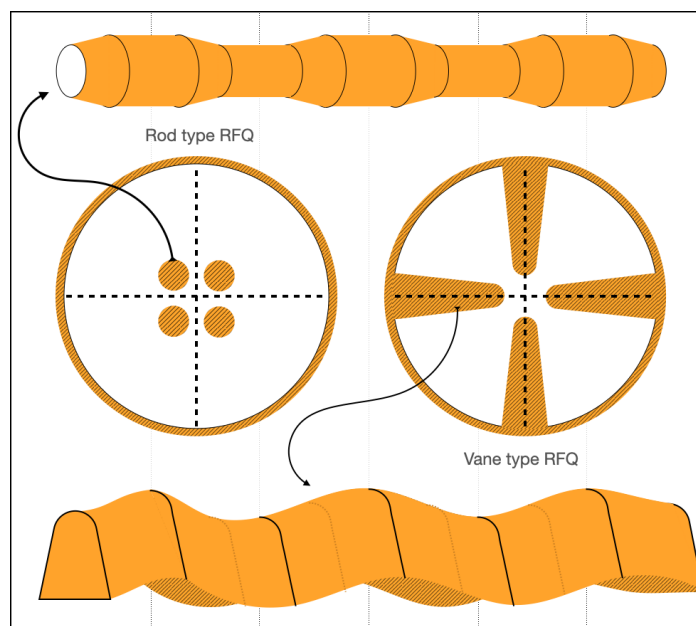


Figure 1.1. The electrodes of both rod and vane types are depicted with some exaggeration along with their respective positions inside their RF cavities.

The most common RFQ type for proton accelerators and light ions (i.e.,  $H^+$ ,  $He^{+2}$ ,  $Li^{+3}$ ) is the vane-type RFQ. This type of RFQ can be considered as a cylindrical cavity operating at  $TE_{210}$  mode (Figure 1.1). This design includes four electrodes known as vanes, around which oscillating magnetic fields induce electrical potential at the vane tips (Figure 1.2). Although vane-type RFQs are more efficient in terms of RF power and easier to cool down, their cavity design is more demanding due to the proximity of dipole mode resonant frequencies to the  $TE_{210}$  operation frequency. Additionally, the misalignment of vane positions can exacerbate this issue.

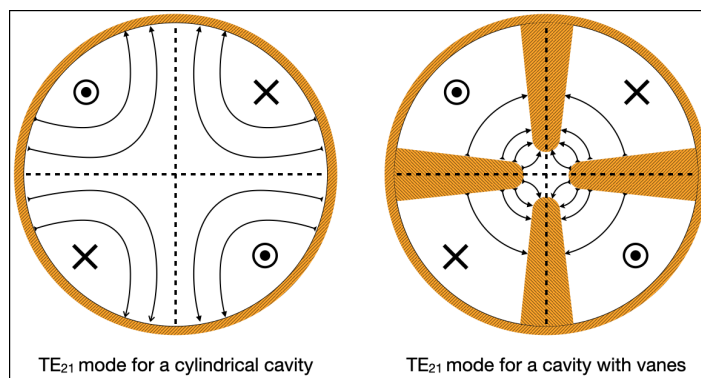


Figure 1.2. Figure depicting comparison between a cylindrical cavity operating at the  $TE_{21}$  mode and a cavity with vanes.

#### 1.4. Parameters Describing a RFQ Cell

The input ion beam particles are exposed to an electric field, which is determined by the vane voltage, frequency of the RFQ, and the geometry of the vanes. This vane geometry is mentally divided into substructures, or cells, to facilitate in-depth study and analysis. A cell is a section that starts with a local minimum distance between the vertical or horizontal vanes and ends with the next maximal distance on that vane (Figure 1.3).

Assuming that the gap between vanes is much smaller than the RF wavelength, the electric field within this gap can be simplified to a static solution multiplied by a periodic time-dependent term. The modulating structure generates electric fields that

are capable of providing energy to particles in the  $z$ -direction. Granted that we have acceleration in the  $z$  direction, we also need particles to be closely packed and follow a trajectory in an envelope where it is smaller than the aperture created by the cells.

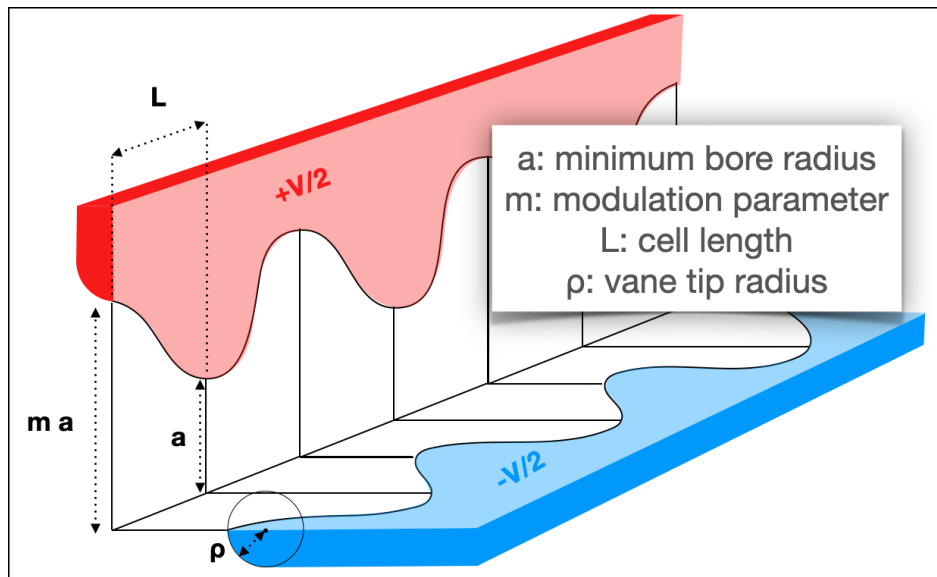


Figure 1.3. Parameters that define a RFQ cell.

Due to the natural tendency of packed ions to disperse, it is necessary to implement focusing mechanisms to keep them on the desired path. The quadrupole geometry of the accelerator decouples the movement on the horizontal ( $x$ ) and vertical ( $y$ ) axis so that they can be thought independent for low currents. Carefully chosen design parameters can result in effective focusing-defocusing lattices (FODO) on  $x$  &  $y$  axis that can keep the particles in the beam line.

The RFQ must also serve the purpose of bunching the DC beam generated by the source. The modulations on the vanes can create both accelerating and decelerating fields in the beam direction, which enables both bunching and acceleration to occur simultaneously. However, the DC beam must be prepared for the time-dependent focusing structure for optimal acceptance. This is ensured by slowly increasing the quadrupole focusing strength at the beginning of the RFQ. Then bunching can be achieved by gradually increasing the modulation from a state of no modulation while simultaneously controlling the length and aperture of the cells within the accelerator's

design. By carefully manipulating these factors, a phase advance and bunch formation can be established.

### 1.5. Two Term Potential and Eight Term Potential

In a vacuum RF cavity operating under the standing wave mode, the solutions to Maxwell's equations can be simplified to the Helmholtz equation, which can be expressed as

$$\nabla^2 \vec{E} + k^2 \vec{E} = 0, \quad (1.1)$$

where  $k$  represents the wave number, defined as  $2\pi/\lambda$ , with  $\lambda$  representing the RF wavelength in a vacuum, and  $\vec{E}$  representing the time-independent component of the electric field. If the distance between vanes is small compared to the RF wavelength in a vacuum, then the term related to the gradient created by these vanes is larger than the second term in the Helmholtz equation. As an approximation, we can assume the  $\vec{E}$  obeys Laplace's equation, which is

$$\nabla^2 \vec{E} = 0. \quad (1.2)$$

We can express the following vector identity for the electric field as

$$\nabla \times (\nabla \times \vec{E}) = \nabla(\nabla \cdot \vec{E}) - \nabla^2 \vec{E}. \quad (1.3)$$

By using the divergence of the electric field for the vacuum,  $\nabla \times \vec{E} = 0$ , and assuming the approximation  $\nabla^2 \vec{E} = 0$  holds we can write the equation as

$$\nabla \times (\nabla \times \vec{E}) = 0. \quad (1.4)$$

In this context, solutions for  $\vec{E}$  can be written as the gradient of a scalar potential  $\vec{E} = -\nabla V$  since  $\nabla \times \nabla V = 0$ . For a zero beam current assumption, we can express the equation as

$$\nabla \cdot \vec{E} = -\nabla^2 V = 0. \quad (1.5)$$

In this form, the electric potential can be represented as

$$V(x, y, z, t) = V(x, y, z) \sin(\omega t), \quad (1.6)$$

where the  $\omega$  is the angular frequency, and the  $V(x, y, z)$  obeys the Laplace's equation

$$\nabla^2 V(x, y, z) = 0, \quad (1.7)$$

with the boundary conditions defined by electrode surface and potential [13].

K-T proposed a subset of solutions to Laplace's equation in cylindrical coordinates to define the potential, using symmetries of an RFQ cell [3]. This solution can be expressed as

$$\begin{aligned} V(r, \theta, z) = & \frac{V_0}{2} \left[ \sum_{m=1}^{\infty} A_{0m} \left(\frac{r}{r_0}\right)^{2m} \cos(2m\theta) \right. \\ & \left. + \sum_{n=1}^{\infty} \sum_{m=0}^{\infty} A_{nm} I_{2m}(nkr) \cos(2m\theta) \cos(nkz) \right], \end{aligned} \quad (1.8)$$

where  $r$  and  $\theta$  are cylindrical coordinates for which  $z$  represents the beam direction,  $V_0$  is the inter-vane voltage,  $k$  is the wave parameter given by  $k = 2\pi/\lambda\beta$ , with  $\lambda$  being the RF wavelength and  $\beta$  being the speed of the ion relative to the speed of light. Also,  $r_0$  is the mean aperture of the vanes,  $I_{2m}$  is the modified Bessel function of order  $2m$  and the  $A_{nm}$  are the multipole coefficients whose values, depending on the vane geometry, should be obtained.

K-T choose following two terms to define potential(TTP) within an RFQ cell which is expressed as

$$V(r, \theta, z) = \frac{V_0}{2} [A_{01} r^2 \cos(2\theta) + A_{10} I_0(kr) \cos(kz)]. \quad (1.9)$$

In this simple form, one can infer the values of  $A_{01}$  and  $A_{10}$  using the vane tip positions at the start of a cell. Specifically,

$$A_{01} = \frac{V}{2a^2} \frac{I_0(ka) + I_0(kma)}{m^2 I_0(ka) + I_0(kma)} \quad (1.10)$$

and

$$A_{10} = \frac{V}{2} \frac{m^2 - 1}{m^2 I_0(ka) + I_0(kma)}. \quad (1.11)$$

Also the dimensionless terms, acceleration efficiency( $A$ ) and focusing efficiency ( $\chi$ ), can be defined as

$$A = \frac{m^2 - 1}{m^2 I_0(ka) + I_0(kma)} \quad (1.12)$$

and

$$\chi = \frac{I_0(ka) + I_0(kma)}{m^2 I_0(ka) + I_0(kma)}. \quad (1.13)$$

The TTP expression is analytically differentiable, leading to the development of a well-defined expression for the electric field in Cartesian coordinates, expressed as

$$E_x = -\frac{\chi V}{a^2}x - \frac{kAV}{2}I_1(kr)\frac{x}{r}\cos(kz), \quad (1.14)$$

$$E_y = +\frac{\chi V}{a^2}y - \frac{kAV}{2}I_1(kr)\frac{y}{r}\cos(kz), \quad (1.15)$$

$$E_z = +\frac{kAV}{2}I_0(kr)\sin(kz). \quad (1.16)$$

In RF accelerator design, a hypothetical particle with the nominal energy gain following the designed trajectory is defined as the synchronous particle. In an RFQ, the synchronous particle trajectory follows the center of the vanes along the  $z$  direction. The rest of the particle coordinates are defined with respect to this ideal particle. With the help of the electric field expression, the energy gain in a cell for the synchronous particle  $W_s$  can be given by

$$\Delta W_s = qE_0 T l \cos(\phi_s), \quad (1.17)$$

where  $E_0$  is the average peak axial accelerating field, given by  $E_0 = \frac{2AV_0}{\beta\lambda}$ ,  $T$  is the transit time factor ( $T = \frac{\pi}{4}$ ),  $l$  is the cell length,  $q$  is the charge of the particle, and  $\phi_s$  is the phase of the synchronous particle. The differential equations governing the energy and phase differences between an arbitrary ion and the synchronous ion can be expressed as

$$\frac{d}{dz}(W - W_s) = qE_0 T (\cos(\phi) - \cos(\phi_s)), \quad (1.18)$$

$$\frac{d}{dz}(\phi - \phi_s) = -\frac{2\pi(W - W_s)}{m_0 c^2 \lambda \beta_s^3 \gamma_s^3}. \quad (1.19)$$

By combining these equations, we can derive the equation of motion for an arbitrary ion relative to the synchronous ion, which is given by

$$\frac{d}{dz}(\beta_s^3 \gamma_s^3 \frac{d}{dz}(\phi - \phi_s)) = -\frac{2\pi q E_0 T}{m_0 c^2 \lambda} (\cos(\phi) - \cos(\phi_s)), \quad (1.20)$$

where  $m_0$  is the mass of the ion,  $q$  is the charge of the ion,  $\gamma_s$  is the Lorentz factor of the synchronous particle,  $\lambda$  is the free-space wavelength,  $W$  and  $\phi$  represent the energy and phase of an arbitrary ion [14].

For small oscillations, the equation of motion can be approximated to give the small oscillation wavelength  $\lambda_\Omega$  in the longitudinal direction. Specifically, the equation is given by

$$\frac{d^2}{dz^2}(\phi - \phi_s) = \frac{2\pi q E_0 T}{\beta_s^3 \gamma_s^3 m_0 c^2 \lambda} \sin(\phi_s)(\phi - \phi_s), \quad (1.21)$$

and the small oscillation wavelength is calculated as

$$\lambda_\Omega = 2\pi \left( -\frac{2\pi q E_0 T}{\beta_s^3 \gamma_s^3 m_0 c^2 \lambda} \right)^{-\frac{1}{2}}. \quad (1.22)$$

In the case of large oscillations, the length of the stable region  $\Phi_s$  is around the synchronous phase (known as the separatrix length) and can be determined solving the equation

$$\tan(\phi_s) = \frac{\sin(\Phi_s) - \Phi_s}{1 - \cos(\Phi_s)}, \quad (1.23)$$

by numerical methods [15]. In summary, energy gain of particles that arrive earlier than the synchronous particle is lower, while the particles that arrive later have a higher energy gain. This restoring effect allows particles to be accelerated in unison with the intended synchronous particle.

The particles' transverse stability can be discussed in terms of phase advance per focusing period for zero current, denoted as  $\sigma_0$ , and defined as

$$\sigma_0^2 = \frac{1}{8\pi^2} \left( \frac{qV_0 \lambda^2 \chi}{m_0 c^2 a^2 \gamma} \right)^2 + \frac{\pi q A V_0 \sin(\phi_s)}{2\beta^2 m_0 c^2 \gamma^3}, \quad (1.24)$$

with the lower stability condition of  $\sigma_0^2 > 0$ .

For  $-\frac{\pi}{2} < \phi_s < 0$  (synchronous acceleration condition), the second term takes negative values. Effectively, it reduces the focusing strength. Considering the dependence on acceleration efficiency  $A$ , defocusing increases with the modulation. With a the non-relativistic approximation, another parameter called focusing strength  $B$  is defined by

$$B = \frac{qV_0 \lambda^2 \chi}{m_0 c^2 a^2}. \quad (1.25)$$

In the low  $\beta$  region of the RFQ, the focusing strength is not dependent on the particle's velocity. Therefore, this parameter can be kept constant in the design phase, ensuring simple transverse motion in the low beta region.

The TTP approach is commonly employed for designing RFQ accelerators due to its well-understood effects on the beam. However, the vane geometry defined TTP equipotential surface is hard to manufacture. Furthermore, the small separation between vanes limits the maximum achievable electric field, making the RFQ difficult to operate. Usually, a simpler geometry with a constant vane tip radius within the cells is used in RFQ designs (Figure 1.3).

The TTP is not accurate in defining the inter-vane potential of this new geometry. With the simplified geometry, the acceleration of the particles differs from the designed values; therefore, more accurate potential representation is needed for both simulation and finalizing the design. The LANL team proposed to extend the potential description using eight terms in total [13]. These terms can be expressed as

$$\begin{aligned}
 V(r, \theta, z) = \frac{V_0}{2} & [A_{01} \left(\frac{r}{r_0}\right)^2 \cos(2\theta) + A_{03} \left(\frac{r}{r_0}\right)^6 \cos(6\theta) \\
 & + A_{10} I_0(kr) \cos(kz) \\
 & + A_{10} I_4(kr) \cos(4\theta) \cos(kz) \\
 & + A_{21} I_2(2kr) \cos(2\theta) \cos(2kz) \\
 & + A_{23} I_6(2kr) \cos(6\theta) \cos(2kz) \\
 & + A_{32} I_4(3kr) \cos(4\theta) \cos(3kz) \\
 & + A_{30} I_0(3kr) \cos(3kz)].
 \end{aligned} \tag{1.26}$$

However, eight-term potential (8TP) is not straightforward to calculate as TTP. The PARMTEQ code, for example, uses tabulated values of cell parameters and their corresponding 8TP coefficients to update the initial TTP-based design and later for RFQ beam dynamics simulation.

## 1.6. LANL RFQ Design Schema

In simple terms, the LANL schema extends the adiabatic bunching (gentle bunching) and acceleration proposed by K-T by adding a Radial Matching Section and a Shaper Section. The addition of these section increases beam capture while keeping the length of the resulting RFQ within practical limits.

### 1.6.1. Radial Matching Section

In a radio-frequency quadrupole (RFQ) accelerator, the polarity of the vanes changes periodically, leading to time-varying focusing forces. A DC beam will occupy a constant transverse phase in time; therefore, the beam needs to be prepared for time-dependent focusing to reduce particle loss. To mitigate this issue, a Radial Matching Section (RMS) can be added to the RFQ to increase the focus strength gradually from zero to the desired value. Ken Crandall proposed the potential function for the RMS section in reference [16]. It is described as

$$V_{RMS}(r, \theta, z) = \frac{V_0}{2} \sum_{n=0}^3 A_n (I_{2n} k_{rms} r \cos(k_{rms} z) + 3^{-(2n+1)} I_{2n}(3k_{rms} r) \cos(3k_{rms} z)) \cos(2n\theta). \quad (1.27)$$

Here,  $k_{rms}$  denotes  $\pi/L$ , where  $L$  represents the length of the RMS section, and coordinate  $z = 0$  corresponds to the end of the section. The terms  $A_n$  are computed from the vane tip positions and transverse curvature tips at the end of the RMS. Once the  $A_n$  terms are determined, the vane geometry is also defined for RMS.

### 1.6.2. Shaper Section

The Gentle Buncher (GB) section is an essential component of RFQ accelerators that allows for the adiabatic bunching of the beam. However, the length of the GB section becomes impractical, and a solution to this is the inclusion of a Shaper Section (SS) in the accelerator design. The SS typically begins with a phase angle of  $-\pi/2$  and a vane modulation of  $m = 1$ . These values then increase linearly with respect to the coordinate  $z$  until they reach the starting values for the GB section. The inclusion of the SS allows for short designs with excellent transmission efficiencies for RFQ designs.

### 1.6.3. Gentle Buncher Section

The Gentle Buncher (GB) section is responsible for bunching and accelerating the beam to the desired energy and phase for entering the acceleration section. To prevent

longitudinal emittance growth due to bunch formation, K-T proposed introduced adiabatic bunching strategy where the bunch-length and small oscillations frequency kept constant throughout the bunching section [6]. The geometrical length of the bunch can be determined from the length of the separatrix ( $\Phi_s$ ) and is given by

$$z_b = \frac{\beta\lambda\Phi_s}{2\pi}, \quad (1.28)$$

and small longitudinal oscillation frequency is expressed as

$$f_\Omega = \frac{\beta c}{\lambda_\Omega}. \quad (1.29)$$

These two values are calculated at the beginning of acceleration section and cell parameters computed backwards until the start energy of the GB is reached. These two relations defines  $\phi_s$  and  $A$  for a given  $\beta$ , together with other design choices (i.e., constant  $B$  and  $r_0$ ), all the cell parameters in the GB section can be defined.

#### 1.6.4. Acceleration Section

In the acceleration section, the main objective is to increase the energy of the bunched particles to their designated exit energy. Typically, in this section,  $\phi_s$  and  $m$  are kept constant throughout the section. It is worth noting that as the value of  $\beta$  increases, the cell length also increases. Also higher particle velocities poses the magnetic lenses as a more viable solution for constructing the focusing structure. As a result, the acceleration section is typically designed to achieve medium beam energies, where other accelerators such as DTL can work more efficiently to accelerate the particles to higher energies.

## 2. INTRODUCTION TO THE FINITE ELEMENT METHOD

The finite element method (FEM) is a numerical method to solve differential equations with either Dirichlet or mixed boundary conditions [17]. We employed FEM to compute the electric fields created by an RFQ cell.

As outlined in chapter 1, the static component of the inter-vane potential satisfies Laplace’s equation. The inter-vane potential solution can be used to simulate beam dynamics for low-current beams. Additionally, we can correct electromagnetic forces by separately computing space and image charge effects and integrating them into the simulation as “kicks” at specified intervals to suit higher current designs. In both instances, the computation of potential is a critical step in our approach to studying beam dynamics.

There are differences between the potential generated with simplified geometry and the TTP used in the design phase. In order to represent the potential field accurately, PARMTEQ uses tabulated values to interpolate the 8T potential values for a given cell. These tables were constructed using CHARGE3D, which calculates charge densities on the electrode surface that gives the correct potential difference between electrodes. In contrast, the RFQ simulation code Toutatis [18] uses the finite difference method and solves Poisson’s equation instead of modeling effects separately. RFQCOEF [19] also calculates 8TP values, but it relies on the FEM. We opted to incorporate the same FEM approach to solving Laplace’s equation based on its speed, flexibility, and simplicity.

### 2.1. Galerkin Method

Let us start by imagining the volume of the problem  $\Omega$  divided into non-overlapping elements with sub-volumes  $\Omega^i$ . Here, the superscript notation  $i$  denotes that a

given quantity belongs to the  $i$ -th element. It is important to note that this notation is unrelated to exponentiation or power and should not be confused with superscripts used in other contexts. Specifically, we do not use Einstein notation in this chapter and do not use the variable  $i$  in contexts where it represents exponentiation or power.

Each element is associated with several nodes, which can be located within the element volume or on its boundary. These nodes are associated with a corresponding interpolation function  $\mathbf{N}_j$ .

The solution within an arbitrary element can be defined as

$$V(x, y, z) = \sum_{j=1}^n v_j N_j(x, y, z), \quad (2.1)$$

where,  $j$  is the node index for the element,  $n$  is the number of nodes, and  $v_j$  represents the value of the solution at the  $j$ -th node coordinate.

Now let us assume we have a test function  $U^i$  for the  $i$ -th element. If  $U^i$  is a solution, then it satisfies the equation

$$\nabla^2 U^i = 0. \quad (2.2)$$

On the other hand, if  $U^i$  does not satisfy the above equation, there exist points within the domain  $\Omega^i$  where the term  $\nabla^2 U^i$  has non-zero values. By multiplying the term  $\nabla^2 U^i$  with a weight function  $W^i$  of our choice (which is defined in  $i$ -th element) and then integrating it, we can obtain the weighted residual given by

$$r^i = \iiint_{\Omega^i} W^i \nabla^2 U^i dx dy dz. \quad (2.3)$$

It follows that if the  $U^i$  is a solution, then

$$r^i = 0. \quad (2.4)$$

The equation above will always hold, regardless of the choice of weight function  $W^i$ .

### 2.1.1. Relaxed Form of the Equation

Since we divided the volume of the problem into elements, we need to ensure the continuity of the test functions across elements. Especially in this form, the solution must be square integrable between shared element borders. For discretization to work for various element types, the problem needs to be relaxed, which is also called the weak form of the problem.

Using Gauss's divergence theorem, we can rewrite the equation  $r^i = 0$  as

$$0 = \iiint_{\Omega^i} W^i \nabla(\nabla U^i) dx dy dz, \quad (2.5)$$

$$0 = \oint_{\Gamma^i} W^i \nabla U^i \cdot \hat{n} ds - \iiint_{\Omega^i} \nabla W^i \cdot \nabla U^i dx dy dz, \quad (2.6)$$

where  $\Gamma^i$  denotes the volumes boundary surface and  $\hat{n}$  is the normal vector of the surface. The equation now has a relaxed continuity requirement for the  $U^i$ . The test function can be constructed by node values and associated functions for the element  $i$ , such that

$$U^i_{(x,y,z)} = \sum_{j=1}^n u_j^i N_j^i(x, y, z). \quad (2.7)$$

When we substitute  $U^i_{(x,y,z)}$  into the relaxed form of the equation, we get

$$\oint_{\Gamma^i} W^i \nabla \sum_{j=1}^n u_j^i N_j^i(x, y, z) \cdot \hat{n} ds - \iiint_{\Omega^i} \nabla W^i \cdot \nabla \sum_{j=1}^n u_j^i N_j^i(x, y, z) dx dy dz = 0. \quad (2.8)$$

However, we still need to specify the function space in which the weight function  $w$  belongs. In the Galerkin method, we choose the basis functions of the weight function for the  $i$ -th element to be the same as the interpolation functions for that element, i.e.,

$$w_k^i = N_k^i \text{ for } k = \{0, 1, \dots, n\}. \quad (2.9)$$

Any function  $W^i$  that is defined in this basis can be construct from  $w_k^i$  as

$$W^i = \sum_{k=1}^n c_k^i N_k^i. \quad (2.10)$$

Furthermore, we can move the divergence in to summation as

$$\nabla \sum_{k=1}^n c_k^i N_k^i = \sum_{k=1}^n c_k^i \nabla N_k^i. \quad (2.11)$$

If we replace the  $W^i$  in eq(2.8) with the definition in eq(2.10) and move summation over  $k$  and  $c_k^i$  out of both integrals, we arrive at the equation

$$\begin{aligned} \sum_{k=1}^n c_k^i \iiint_{\Omega^i} \nabla N_k^i(x, y, z) \cdot \nabla \sum_{j=1}^n u_j^i N_j^i(x, y, z) dx dy dz = \\ \sum_{k=1}^n c_k^i \oint_{\Gamma^i} N_k^i(x, y, z) \nabla \sum_{j=1}^n u_j^i N_j^i(x, y, z) \cdot \hat{n} ds. \end{aligned} \quad (2.12)$$

For the above equation to hold true for all choices of  $W^i$ , the equation

$$\begin{aligned} \iiint_{\Omega^i} \nabla N_k^i(x, y, z) \cdot \nabla \sum_{j=1}^n u_j^i N_j^i(x, y, z) dx dy dz = \\ \oint_{\Gamma^i} N_k^i(x, y, z) \nabla \sum_{j=1}^n u_j^i N_j^i(x, y, z) \cdot \hat{n} ds, \end{aligned} \quad (2.13)$$

for  $k \in \{0, \dots, n\}$

must hold true. Furthermore, we can take the summation on the left-hand side of the equation outside the integral and rewrite the equation as

$$\begin{aligned} \sum_{j=1}^n u_j^i \iiint_{\Omega^i} \nabla N_k^i(x, y, z) \cdot \nabla N_j^i(x, y, z) dx dy dz = \\ \oint_{\Gamma^i} N_k^i(x, y, z) \nabla \sum_{j=1}^n u_j^i N_j^i(x, y, z) \cdot \hat{n} ds, \end{aligned} \quad (2.14)$$

for  $k \in \{0, \dots, n\}$ .

Now, the problem can be expressed in the form of a matrix equation as

$$A_i \vec{x}_i = \vec{b}_i, \quad (2.15)$$

where the elements of the matrix  $A^i$  and elements of the vectors are defined as

$$A_{kj}^i = \iiint_{\Omega^i} \nabla N_k^i(x, y, z) \cdot \nabla N_j^i(x, y, z) dx dy dz, \quad (2.16)$$

$$x_j^i = u_j^i, \quad (2.17)$$

$$b_k^i = \oint_{\Gamma^i} N_k^i(x, y, z) \nabla \sum_{j=1}^n u_j^i N_j^i(x, y, z) \cdot \hat{n} ds. \quad (2.18)$$

Here,  $A^i$  is called the element stiffness matrix, and  $x_j^i$  is the value of the  $i$ -th elements  $j$ -th node, and  $b_k^i$  is the  $k$ -th vector element of the right-hand side vector. With a

suitable choice of element type and their interpolation function, one can ensure that interpolation functions sufficiently are continuous at the shared element borders. For a shared border between two elements, the normal vector of the border for one element will be equal to the other element’s normal vector multiplied by  $-1$ . Therefore, when we assemble these elements and create the equation for the entire problem volume  $\Omega$ , these contributions will cancel out for each other if the mesh created properly.

**2.1.2. 20 Node Isoparametric Brick Element**

In our study, we utilized the 20-node isoparametric brick elements to define the volume  $\Omega$ . Depiction of an element can be found in the right plot of Figure 2.1. However, working with the element’s volume and boundary in this form can be challenging. To make the elements more manageable, usually, a natural coordinate system is defined and mapped to the element volume in the problem’s coordinates. A 20-node brick element is defined as a cube in its natural coordinates as depicted in the left plot of Figure 2.1. The node coordinates are given in Table 2.1.

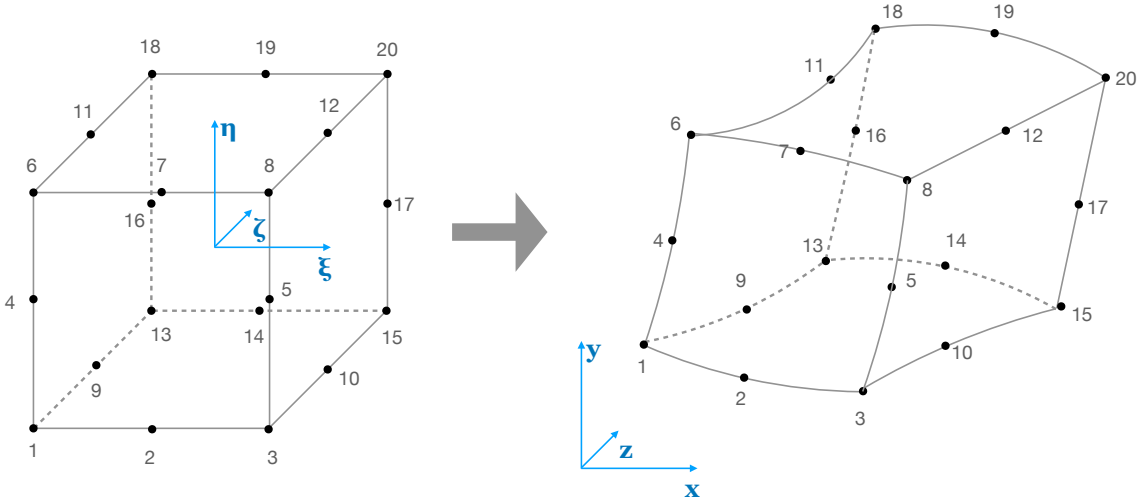


Figure 2.1. The transformation from natural coordinates  $(\xi, \eta, \zeta)$  to the problem’s coordinates  $(x, y, z)$  is illustrated with a moderate exaggeration.

Element in natural coordinates depicted on the left plot.

The element's volume is determined by its interpolation function and the positions of its nodes. The map from natural coordinates to problem coordinates is given by

$$\begin{aligned} x &= \sum_{j=1}^n x_j N_j(\xi, \eta, \zeta), \\ y &= \sum_{j=1}^n y_j N_j(\xi, \eta, \zeta), \\ z &= \sum_{j=1}^n z_j N_j(\xi, \eta, \zeta), \end{aligned} \quad (2.19)$$

where  $x_j, y_j, z_j$  are the node coordinate values in the problem's coordinates,  $N_j(\xi, \eta, \zeta)$  is the  $j$ -th nodes interpolation function in the natural coordinates.

The interpolation functions in the natural coordinates are given as

$$\begin{aligned} N_j &= \frac{1}{8}(1 + \xi\xi_j)(1 + \eta\eta_j)(1 + \zeta\zeta_j)(\xi\xi_j + \eta\eta_j + \zeta\zeta_j - 2) \\ &\quad \text{for } j \in \{1, 3, 6, 8, 13, 15, 18, 20\}, \\ N_j &= \frac{1}{4}(1 - \zeta^2)(1 + \xi\xi_j)(1 + \eta\eta_j) \text{ for } j \in \{9, 10, 11, 12\}, \\ N_j &= \frac{1}{4}(1 - \xi^2)(1 + \eta\eta_j)(1 + \zeta\zeta_j) \text{ for } j \in \{2, 7, 14, 19\}, \\ N_j &= \frac{1}{4}(1 - \eta^2)(1 + \xi\xi_j)(1 + \zeta\zeta_j) \text{ for } j \in \{4, 5, 16, 17\}. \end{aligned} \quad (2.20)$$

These interpolation functions are tabulated explicitly in appendix A.

To illustrate the boundary of the elements in the problem coordinates using the map equations 2.19 and the interpolation functions 2.20, let us consider the surface  $\xi = 1$  in the natural coordinates. When we calculate the interpolation functions, we will see that only nonzero interpolation functions are

$$\begin{aligned} N_j &= \frac{1}{8}(1 + \xi\xi_j)(1 + \eta\eta_j)(1 + \zeta\zeta_j)(\xi\xi_j + \eta\eta_j + \zeta\zeta_j - 2) \\ &\quad \text{for } j \in \{3, 8, 15, 20\}, \\ N_j &= \frac{1}{4}(1 - \zeta^2)(1 + \xi\xi_j)(1 + \eta\eta_j) \text{ for } j \in \{10, 12\}, \\ N_j &= \frac{1}{4}(1 - \eta^2)(1 + \xi\xi_j)(1 + \zeta\zeta_j) \text{ for } j \in \{5, 17\}. \end{aligned} \quad (2.21)$$

The remaining interpolation functions are associated with nodes on the  $\xi = 1$  surface. The nodes that do not lie on this surface also do not contribute to its mapping to problem space. This observation is not limited to this surface only; it applies to other

surfaces such as  $\xi = -1$ ,  $\eta = 1, -1$ , and  $\zeta = 1, -1$ . Consequently, neighboring elements that share a border have the same border definition since both elements have the same node coordinates on that border. Figure 2.2 shows the border of two neighboring elements. Furthermore, the solution at the shared boundary itself is also continuous.

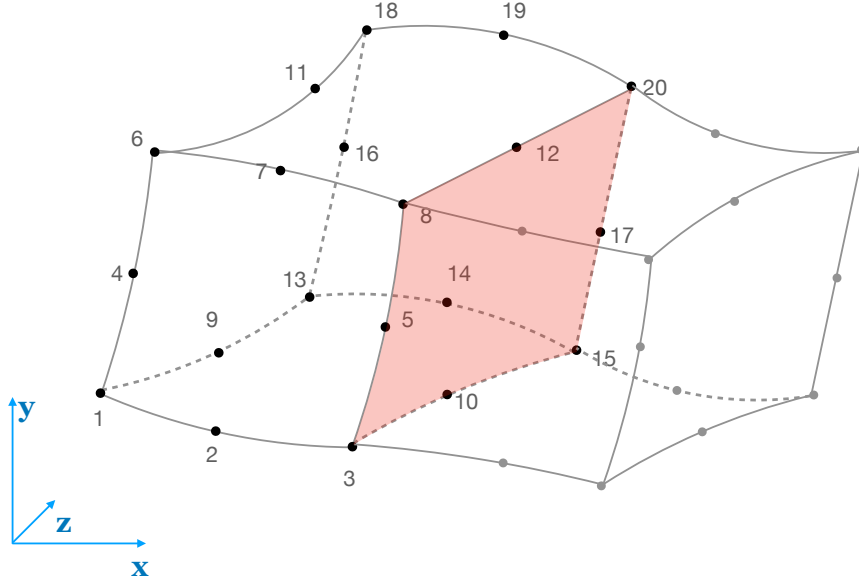


Figure 2.2. A depiction of a shared boundary for two adjacent elements.

The map from natural coordinates to the problem's coordinates is defined, while the inverse map is not. In fact, for interpolation purposes, numerical methods are usually employed to evaluate a solution for a point inside complicated elements like this. However, to find the elements of matrix  $A^i$ , we need to evaluate the corresponding integrals defined in the problem coordinates. It is best to convert these integrals into ones evaluated in the natural coordinate system. Using the Jacobian Matrix given by

$$J(\xi, \eta, \zeta) = \begin{bmatrix} \frac{\partial x}{\partial \xi} & \frac{\partial x}{\partial \eta} & \frac{\partial x}{\partial \zeta} \\ \frac{\partial y}{\partial \xi} & \frac{\partial y}{\partial \eta} & \frac{\partial y}{\partial \zeta} \\ \frac{\partial z}{\partial \xi} & \frac{\partial z}{\partial \eta} & \frac{\partial z}{\partial \zeta} \end{bmatrix}, \quad (2.22)$$

we can write the equation as

$$\begin{bmatrix} \frac{\partial N}{\partial \xi} \\ \frac{\partial N}{\partial \eta} \\ \frac{\partial N}{\partial \zeta} \end{bmatrix} = J(\xi, \eta, \zeta) \begin{bmatrix} \frac{\partial N}{\partial x} \\ \frac{\partial N}{\partial y} \\ \frac{\partial N}{\partial z} \end{bmatrix}. \quad (2.23)$$

Then the inverse relation can be expressed as

$$\begin{bmatrix} \frac{\partial N}{\partial x} \\ \frac{\partial N}{\partial y} \\ \frac{\partial N}{\partial z} \end{bmatrix} = J^{-1}(\xi, \eta, \zeta) \begin{bmatrix} \frac{\partial N}{\partial \xi} \\ \frac{\partial N}{\partial \eta} \\ \frac{\partial N}{\partial \zeta} \end{bmatrix}. \quad (2.24)$$

Using inverse Jacobian, by changing the volume element  $dx dy dz$  to  $\|J\|d\xi d\eta d\zeta$  and with the help of Jacobian determinant, we can transform the integrals in equation 2.16 into natural coordinates as

$$\begin{aligned} A_{jk}^i &= \iiint_{\Omega^i} \nabla N_k^i(x, y, z) \cdot \nabla N_j^i(x, y, z) dx dy dz, \\ &= \int_{-1}^1 \int_{-1}^1 \int_{-1}^1 J^{-1} \nabla N_k^i(\xi, \eta, \zeta) \cdot J^{-1} \nabla N_j^i(\xi, \eta, \zeta) |J| d\xi d\eta d\zeta. \end{aligned} \quad (2.25)$$

In this form, everything needed to evaluate the inside of the integral and volume of the integral is defined in elements' natural coordinates.

However, it is necessary to resort to numerical integration schemes to evaluate this integral. In our studies, we used Gaussian quadrature with the three-point rule in three dimensions. Although more efficient methods can be implemented, we used this widely known and straightforward method. The method can be summarized as

$$\begin{aligned} \int_{-1}^1 \int_{-1}^1 \int_{-1}^1 F(\xi, \eta, \zeta) d\xi d\eta d\zeta &= \int_{-1}^1 \int_{-1}^1 \sum_{a=1}^3 F(\xi_a, \eta, \zeta) d\eta d\zeta, \\ &= \int_{-1}^1 \sum_{a=1}^3 \sum_{b=1}^3 F(\xi_a, \eta_b, \zeta) d\zeta, \\ &= \sum_{a=1}^3 \sum_{b=1}^3 \sum_{c=1}^3 F(\xi_a, \eta_b, \zeta_c), \end{aligned} \quad (2.26)$$

where,

$$\begin{aligned} \xi_1, \eta_1, \zeta_1 &= -\sqrt{\frac{3}{5}} \ \& \ w_1 = \frac{5}{9}, \\ \xi_2, \eta_2, \zeta_2 &= 0 \ \& \ w_2 = \frac{8}{9}, \\ \xi_3, \eta_3, \zeta_3 &= \sqrt{\frac{3}{5}} \ \& \ w_3 = \frac{5}{9}. \end{aligned} \quad (2.27)$$

With the Gaussian quadrature method, we can calculate the element stiffness matrix for  $i$ -th element  $A^i$  by calculating its matrix elements  $A_{kj}^i$  separately.

Table 2.1. Element nodes and their coordinates in natural coordinate system.

Node Number	$\xi$	$\eta$	$\zeta$
1	-1	-1	-1
2	0	-1	-1
3	1	-1	-1
4	-1	0	-1
5	1	0	-1
6	-1	1	-1
7	0	1	-1
8	1	1	-1
9	-1	-1	0
10	1	-1	0
11	-1	1	0
12	0	1	0
13	-1	-1	1
14	0	-1	1
15	1	-1	1
16	-1	0	1
17	1	0	1
18	-1	1	1
19	0	1	1
20	1	1	1

### 2.1.3. Assembly of Global Stiffness Matrix and Forcing Boundary Conditions

To solve the problem on the global level, we need to assign a global index  $i_{global}$  to each node in the problem volume. While the node numbering in the global index can affect the performance of numerical methods employed to solve  $A\vec{x} = \vec{b}$  type problems, any indexing is viable for our purpose even if it is not optimal for the solution method.

To construct the global stiffness matrix  $A$ , we can construct a connection matrix  $C$  with the elements as

$$C_{i_{element},j_{node}} = k_{global}, \quad (2.28)$$

where  $i_{element}$  is the element index,  $j_{node}$  is the node index in the element, and  $k_{global}$  is the global node index.

Next, we start with a  $p \times p$  zero-filled matrix, where  $p$  is the number of nodes in the global problem, and add each element's stiffness matrix element value to the corresponding entry in the global stiffness matrix  $A$ , using the map defined by the connection matrix  $C$ . Since our problem has Dirichlet boundary conditions, and contributions from shared element surfaces cancel each other out, we can use a straightforward method described in reference [20]. First, we assume  $\vec{b}$  is a vector with elements valued as zero. Then, we modify the matrix equation by using the known values of nodes on the problem boundary.

Specifically, we remove the rows corresponding to these nodes from the matrix equation and calculate the contribution of their known values to the remaining rows of equations. We add these calculated contributions to the other side of the equation, resulting in a new matrix equation for our problem which can be expressed as

$$A_{final}x_{final}^{\vec{}} = b_{final}^{\vec{}}. \quad (2.29)$$

This equation represents an approximation of our problem as a linear algebra equation where numerous computer algorithms can be employed for the solution. The use of numerical methods described so far is best achieved using a computer program for designing an RFQ. In the next chapter, such a software program is described.

### 3. DEMIRCIPRO: A RFQ DESIGN SOFTWARE

The design endeavor of an RFQ is a challenging one. It can easily require hundreds of parameters to be set. Typically, these accelerators are designed for bunching the beam quasi-adiabatically, minimizing particle loss to only a few percent. Previous chapters have outlined an approach to achieving this, utilizing assumptions and simplifications with LANL style (RMS, Shaper, Gentle Buncher, accelerator) that reduce the design parameters to about 20. However, even after this reduction, an Ion Source (IS), low energy beam transport (LEBT), and possibly some measurement apparatus may need to be designed to obtain an input beam for the RFQ. Therefore, it is helpful to have an integrated design environment for the entirety of the low-energy beam-line rather than to have scattered studies done in multiple codes.

DemirciPro was born out of such necessities. It is an RFQ and simulation code that we develop from the ground up. The main objective of DemirciPro is to provide reliable results with ease of use. It brings together multiple software tools in a single design and simulation environment. DemirciPro is written in the C++ programming language and utilizes the ROOT [21] library for its GUI.

#### 3.1. DemirciPro Features

This section outlines the current capabilities of DemirciPro. A detailed explanation and results of the studies for IS, LEBT, and Pepper-pot beam measurement design capabilities can be found in [22]. The author's contribution to these sections is limited; thus, we will refrain from in-depth discussions about them in this section.

##### 3.1.1. Ion Source Design and Simulation Using IBSIMU

The beam parameters of the IS are essential for the rest of a beam line. It is relatively easy to degrade the beam along the beam line. For example, the emittance

can increase in different acceleration sections, which is difficult, if not impossible, to recover [23]. An ion source, therefore, must be designed such that its output beam allows some budget for possible degradations. The use of software capable of simulating charge particle dynamics is required in that sense.

Our team opted to use IBSIMU [24], an open-source code that utilizes the finite difference method to solve the Poisson equation in 3D and simulate the effects of ion optics. Ion sources are often designed with cylindrical symmetry, and utilizing this symmetry can significantly reduce computing requirements. Therefore, we developed an interface in DemirciPro that allows users to design and simulate these ion sources in IBSIMU, all within a single interface. This way, users can focus more on simulation and design optimization.

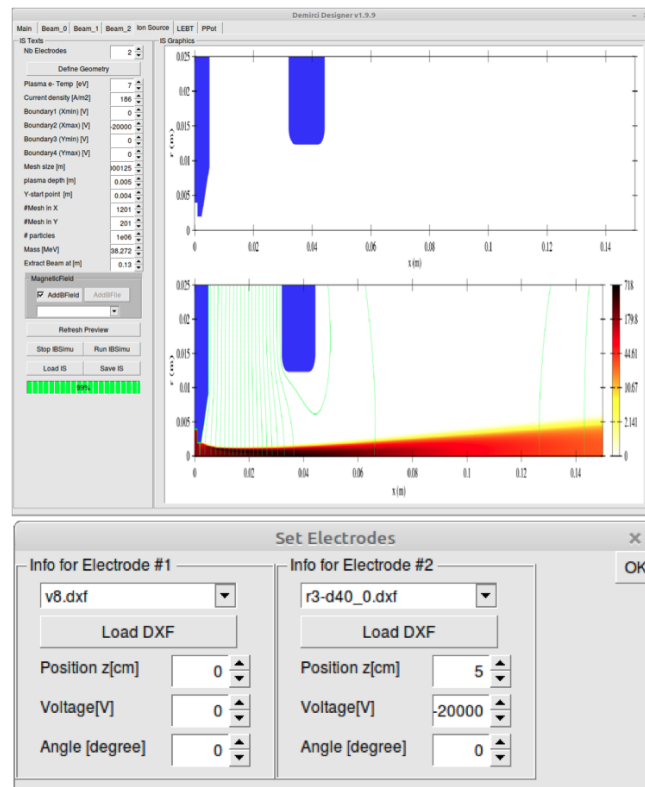


Figure 3.1. At the top: DemirciPro IBSIMU integration is shown as the design parameters, resulting in geometry with chosen electrodes and the IBSIMU simulation result being conveniently presented. At the bottom: The electrode setup pop-up window is shown with individual electrode geometry settings.

Figure 3.1 shows a screenshot of the DemirciPro GUI with the IS section (tab) selected. Ion charge and mass values are taken from the DemirciPro internal variables. The negative electrode's boundary conditions are set to Dirichlet, while the positive electrode is set to Neumann-type boundary conditions, which are the default settings in IBSIMU. Users can select electrodes from a pool of available electrode geometries or import computer-aided design (CAD) files to add new electrodes. Position along the z-axis, rotation, and applied voltage can be separately defined for the electrodes.

Also, magnetic field maps can be imported to account for the effects of residual magnetic fields on the simulation. The imported file should contain the position on the z-axis, distance to the beam axis  $r$ , and magnetic field values  $B_z$  &  $B_r$ . Then the simulation can be run using a defined number of macro particles, and results can be exported to the ".DST" file format to be used again with DemirciPro or other codes such as Travel/Path manager [25]. Furthermore, DemirciPro can save the entire design, reducing the burden of accounting for all the files and parameters for the user.

### 3.1.2. Low Energy Beam Transport (LEBT) Design and Simulation

A Low Energy Beam Transport (LEBT) section is needed to match the beam to RFQ acceptance efficiently. There are two ways the LEBT section can be realized; one is based on electrostatic lenses, and the other one is based on magnet components. Magnet-based designs are commonly used to steer and focus the beam. Therefore, we chose the DemirciPro LEBT design interface to be based on magnet components. The effect of magnets on the beam is simulated using transfer matrices. However, the space charge effects are not yet included in our simulations, although the work is ongoing.

The latest version of DemirciPro includes solenoid, quadrupole, and dipole magnets. Each component can be defined with a physical bounding box and effective magnetic field boundary. The magnetic field measurement or the simulation results can be uploaded for these components, making it possible to simulate the effects of production flaws or design choices made in the magnets. To further ease the design, DemirciPro

incorporates parametric magnet design for the solenoid and quadrupole magnets (Figure 3.2). Furthermore, magnet design parameters can easily be set, changed, saved, and simulated with Poisson Superfish Suite [26]. Consequently, initial studies on magnet and LEBT design were carried out cohesively, further streamlining the process. These magnets can be positioned and set up using a single control panel shown in Figure 3.3.

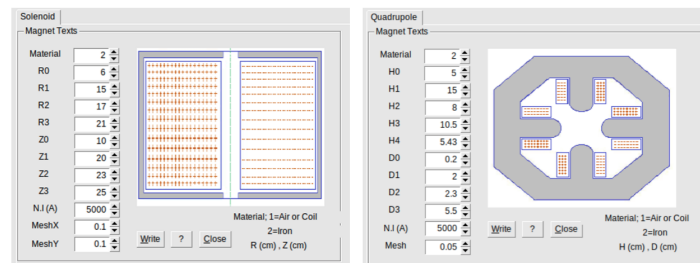


Figure 3.2. Magnet design interface for Poisson-Superfish simulation input files. On the left solenoid, on the right quadrupole magnet parameters are presented.

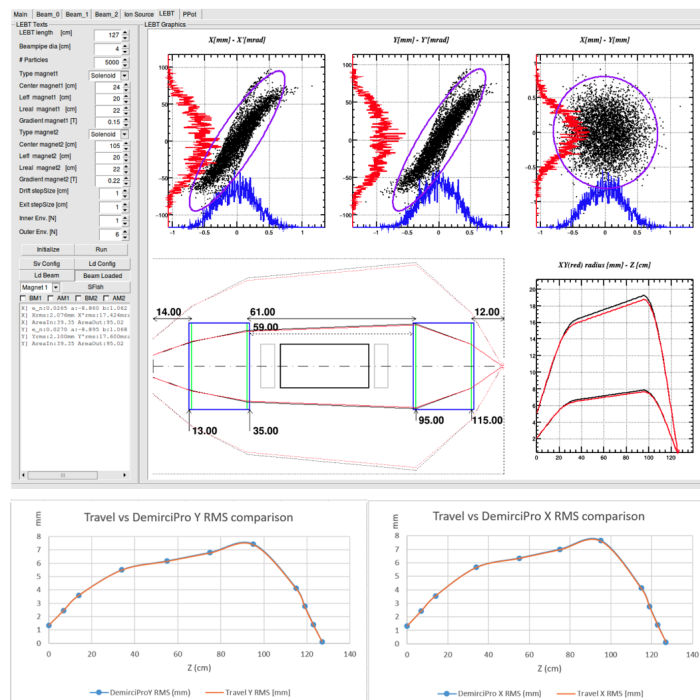


Figure 3.3. On the top: DemirciPro LEBT design and simulation interface is shown.

For a test design, parameters, resulting geometry, and the DemirciPro simulation results can be seen together. A comparison of the LEBT simulation results obtained from DemirciPro and TRAVEL is presented on the bottom.

DemirciPro LEBT design interface can work with DST files, including the particle data at the entrance of the LEBT, or a random beam can be generated internally using the Twiss parameters. The user needs to enter the diameter of the beam pipe together with the LEBT section length. The former is used for flagging lost particles, and the latter for the calculation of the final result. Particle distributions in DST format can be obtained for any position in the beam direction; however, we decided to only write these DST files at the start and end of each magnet to save computer resources. The simulation results of the design, together with its geometric layout, are presented in the same interface. The user can select the quantiles to be used as inner and outer envelopes, and using these settings, the user can efficiently assess the beam behavior. A comparison between DemirciPro and Travel results for a test design can be found in Figure 3.3.

3.1.2.1. Pepper-pot Diagnostic Instrument Design and Simulation. DemirciPro has recently added a new feature, the pepper-pot (PP) diagnostic instrument design and simulation interface. This instrument is used to characterize the beam that will enter the RFQ and to compare the results of LEBT simulations and measurements. This instrument's main component consists of a conductive plaque with a grid of holes machined on, a scintillator screen, an imaging device, and appropriate optics. The PP is used to characterize beam emittance. Furthermore, if the plaque is displaced out of the beam-line same scintillator screen can be used for beam size and position measurement.

Pepper-pot plate samples the original beam into beamlets. These beamlets drift under vacuum to the scintillator screen for a designed distance. Emitted beamlet pattern imaged with the help of optics and an image sensor. Then this image analysis starts by associating each local peak position on the image with a hole. The emittance is calculated using hole positions, drift distance, and peak positions.

The DemirciPro Pepper-pot design tab, shown in Figure 3.4, allows the user to enter the design parameters and quickly observe the simulated beam plots before and

after the pepper-pot as on the scintillator screen. The particles arrived at to screen position binned to pixels. After that, the analysis runs on these binned values and can be overlaid with the truth information as in the rightmost plot in Figure 3.5. This workflow allows the user to optimize the pepper-pot design and characterize expected measurement errors. When a pepper-pot image is acquired, the same design parameters can be loaded and run on this image to measure the emittance of the beam.

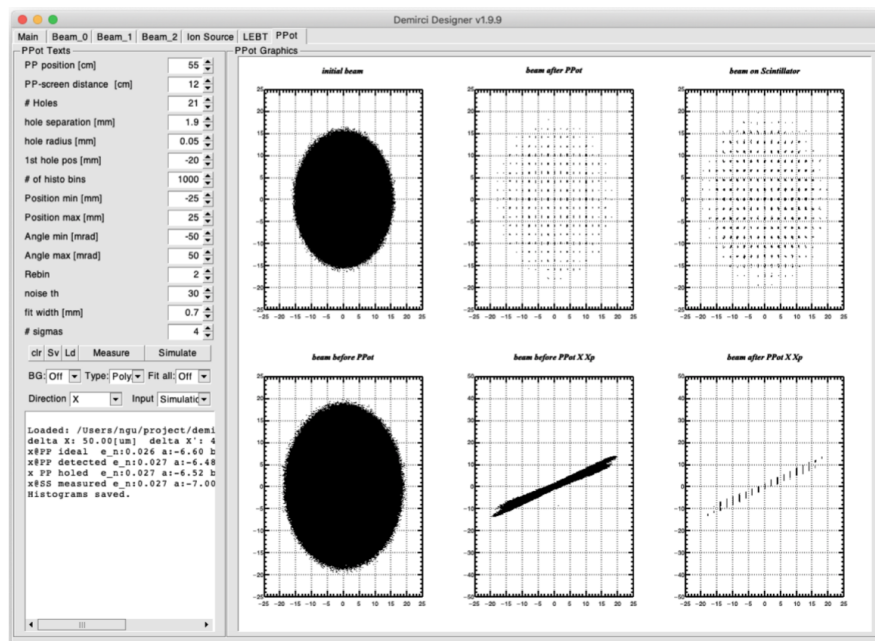


Figure 3.4. DemirciPro pepper pot design, simulation & measurement interface.

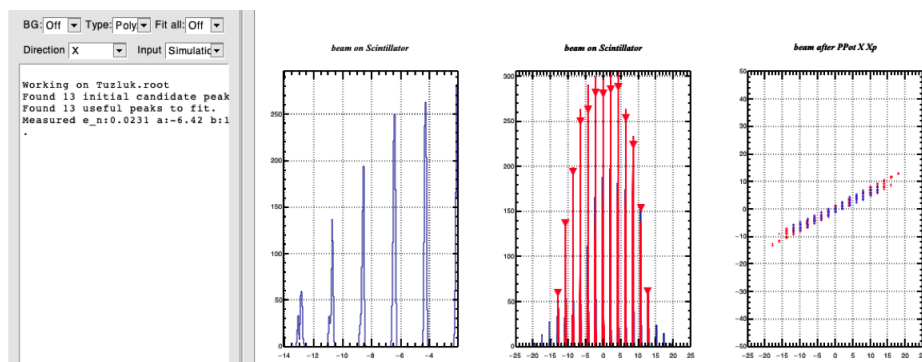


Figure 3.5. DemirciPro pepper pot measurement results. On the left, beamlet distributions zoomed to a particular region. On the center, the central region of beamlet distributions overlaid with fitted Gaussian function. On the right, red values show the truth information, whereas the blue values show measured values.

### 3.1.3. RFQ Design and Simulation with DemirciPro

DemirciPro offers a command line interface (CLI) and a graphical user interface (GUI) for RFQ design and simulations. They share the DemirciPro library, so the calculations use identical functions and classes. We will discuss the features of the GUI, but basic calculations would also give the same results as CLI.

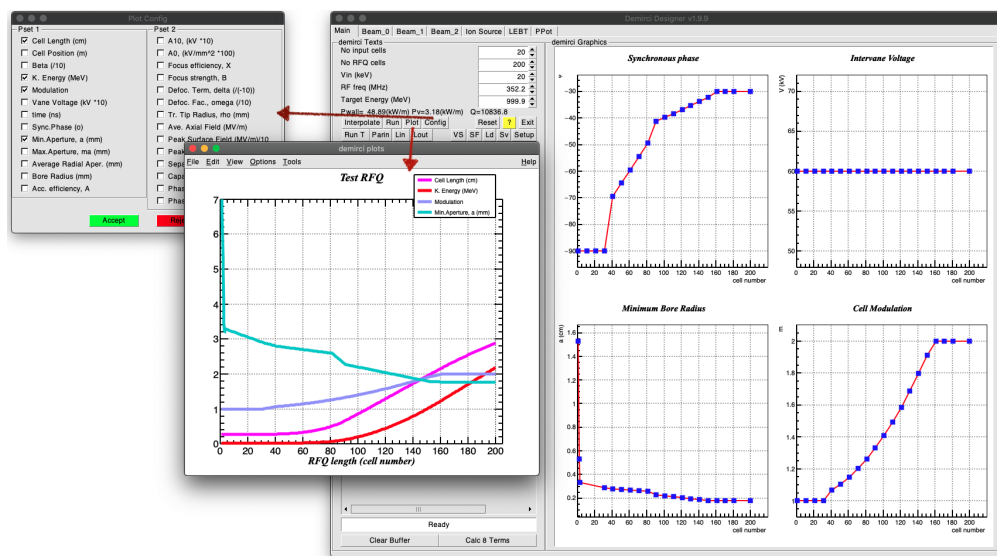


Figure 3.6. DemirciPro’s main page for RFQ design is shown with plot functionality and configuration window of this plot. The user can quickly adjust the interpolation points and see their effect on various parameters.

In Figure 3.6, one can see the main interface For RFQ design. At the right-most window, there are four interactive plots. Again in the same window, some basic design parameters are listed. The user first decides on the number of RFQ cells needed and then decides the number of interpolation points that will be displayed in the four plots. Then user sets some internal values used in the calculations by clicking the setup button and editing the parameters shown in Figure 3.7.

With the parameters set, the user continues to edit the positions of the interpolation points in the synchronous phase, inter-vane voltage, minimum bore radius ( $a$ ), and cell modulation ( $m$ ) plots by simply clicking and dragging them. Then by clicking

the “interpolate” button, the cell values are linearly interpolated using the points on these graphs. The interpolation is shown as a red line, and the interpolation points are shown with blue markers on these graphs. It is important to note that the interpolation values in the synchronous phase and cell modulation should be strictly increasing, whereas the minimum bore radius values should be strictly decreasing. If this is not the case, the user is warned with a pop-up window.

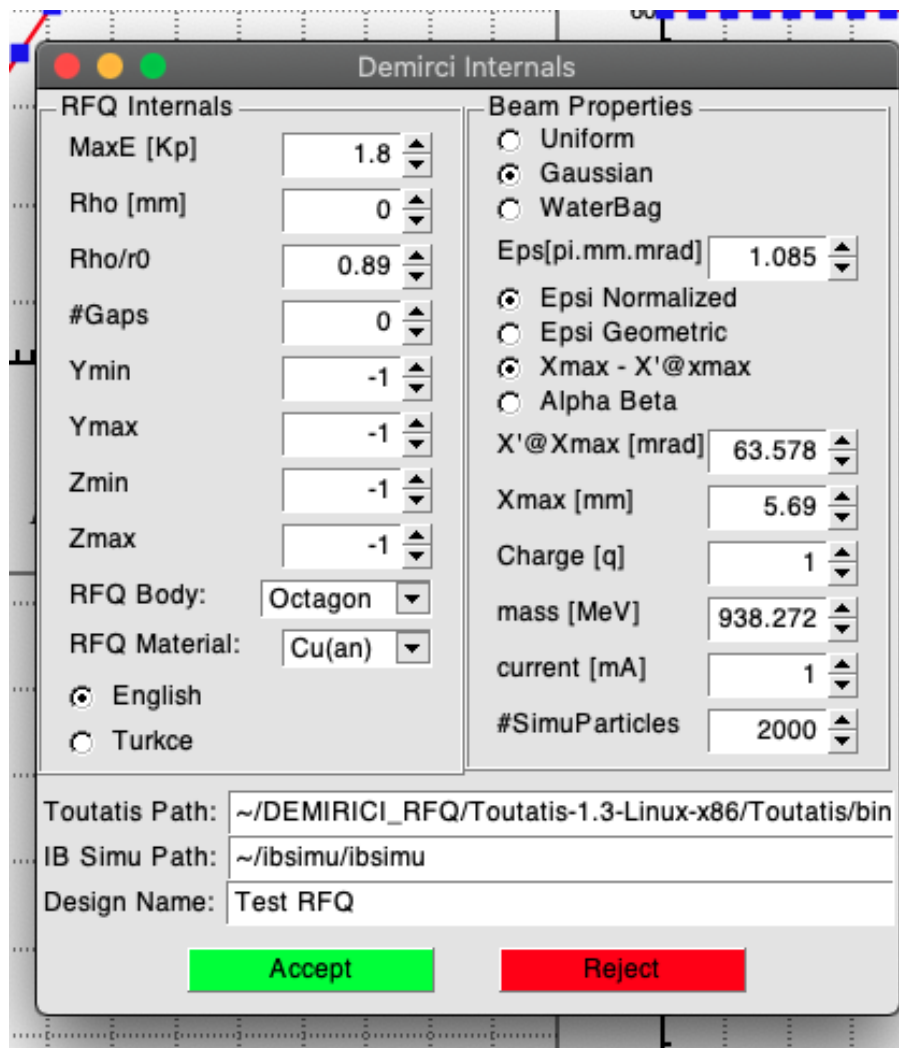


Figure 3.7. DemirciPro internals window.

Following a user update of the interpolation points, the user proceeds with the “run” button to finish the remaining calculations. The results of these calculations can be viewed in a separate window with the help of the “plot” button. The parameters

displayed can be changed via the plot configuration window. This workflow allows the user to start with a more straightforward design and iterate over to the final design. In addition, the user can import values from a text file created by another design code and explore improvements in DemirciPro.

DemirciPro also has an interface for creating Superfish input files for cavity design. The interface (Figure 3.8) can be accessed by clicking the “SF” button. The Superfish input file structure defines each section of the cavity geometry relative to previous sections. For example, modifying one line or arc segment can require recalculating the endpoints of the remaining segments. However, DemirciPro simplifies this process by allowing users to modify parameters easily and generate a new geometry input for Superfish.

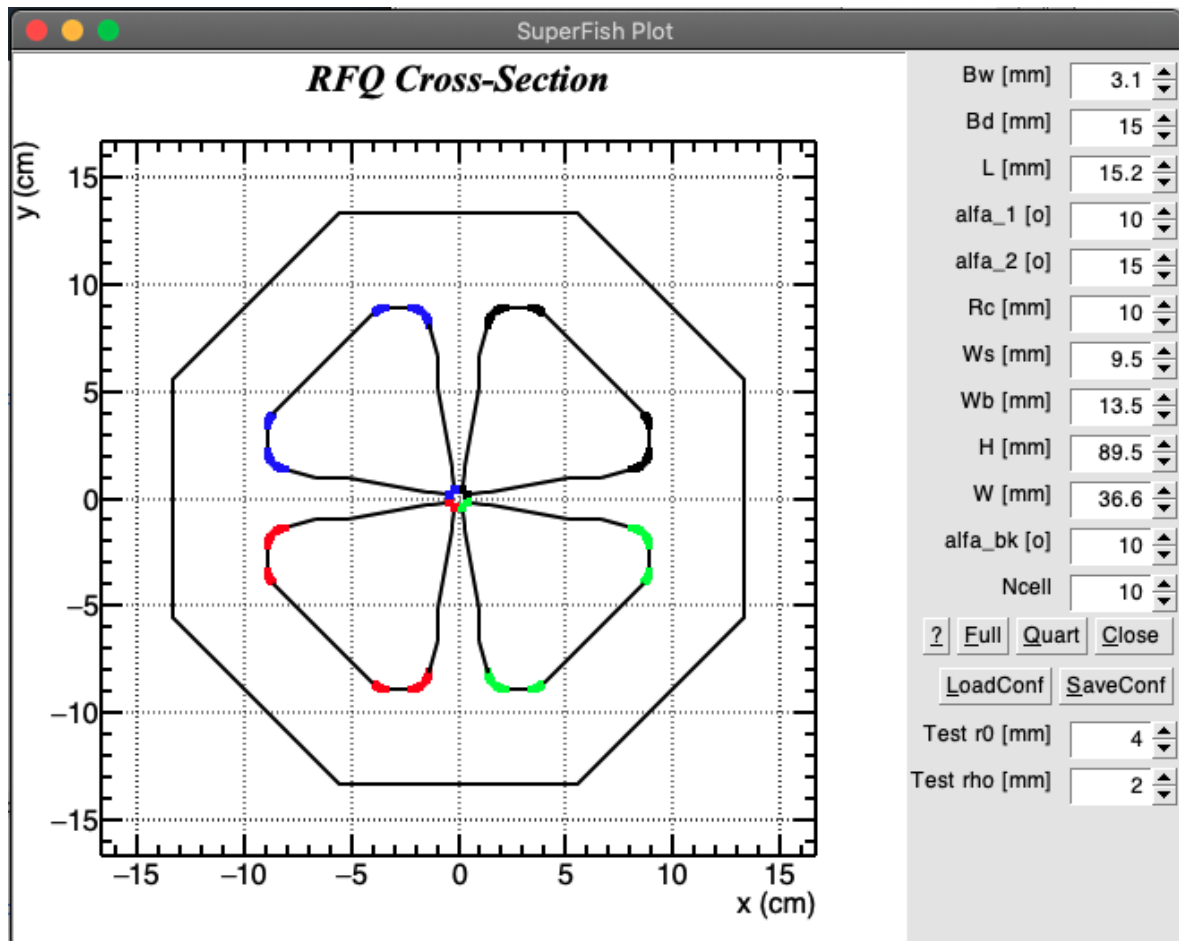


Figure 3.8. DemirciPro’s Superfish input interface.

Another notable interface is the vane window. This window allows sinus or two-term potential (TTP) vanes to be drawn and saved. The user can use the ‘VS’ (vane shape) button to open this window. This window is presented in Figure 3.9. The vane plot can be zoomed in by clicking and dragging. Furthermore, it is possible to draw the vane shapes in 3D as shown in Figure 3.10.

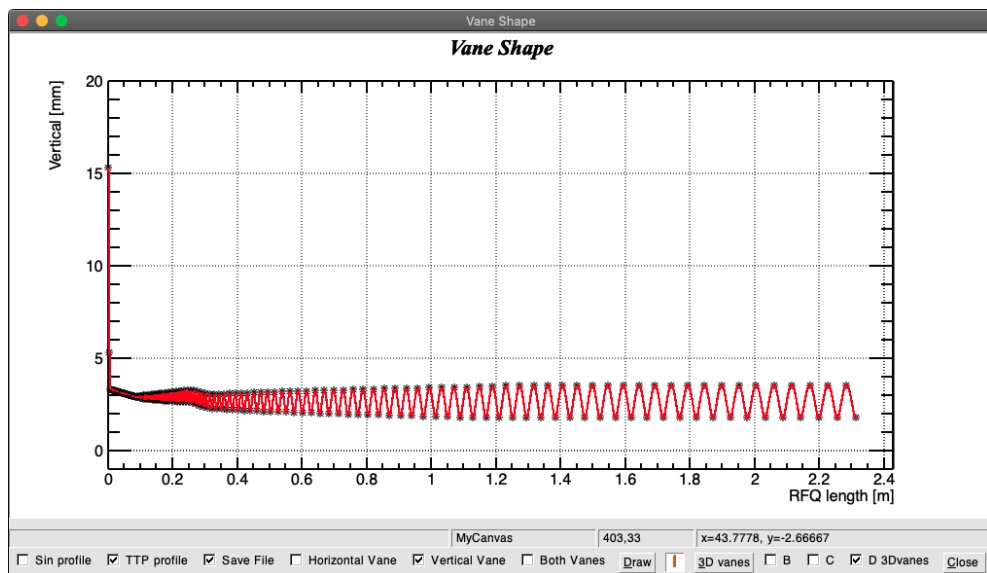


Figure 3.9. Interface for drawing RFQ vanes.

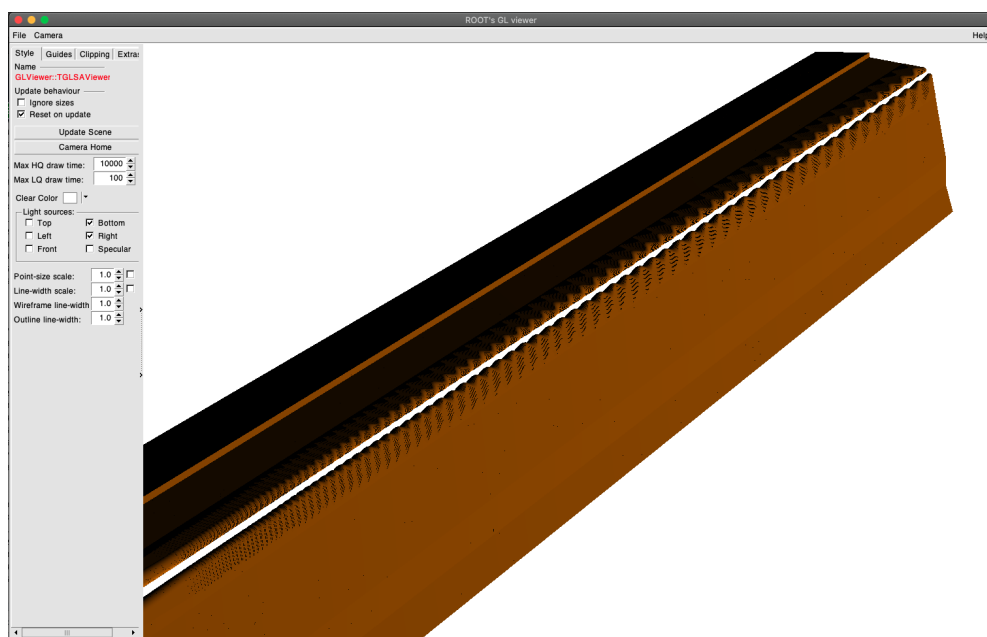


Figure 3.10. 3D view of the RFQ vanes

Once a promising design is achieved, the user can click the “Calc 8 Terms” button to calculate and save the 8T values for each cell. Then the user can simulate the design to the beam dynamics interface.

There are three tabs dedicated to beam dynamics simulation. The user can set which four plots should be presented for each tab. The data presented in different tabs are identical. A picture of the beam dynamics tab can be found in Figure 3.11. Next, the user selects the graphs or histograms desired from the drop-down menus. At the initialize step, macro particles are generated using internal values previously defined. The user can advance the particles inside the RFQ either one step at a time or as an animation by clicking the “play” button. We also included a 3D representation of the macro particle positions in space. An example of this can be found in Figure 3.12.

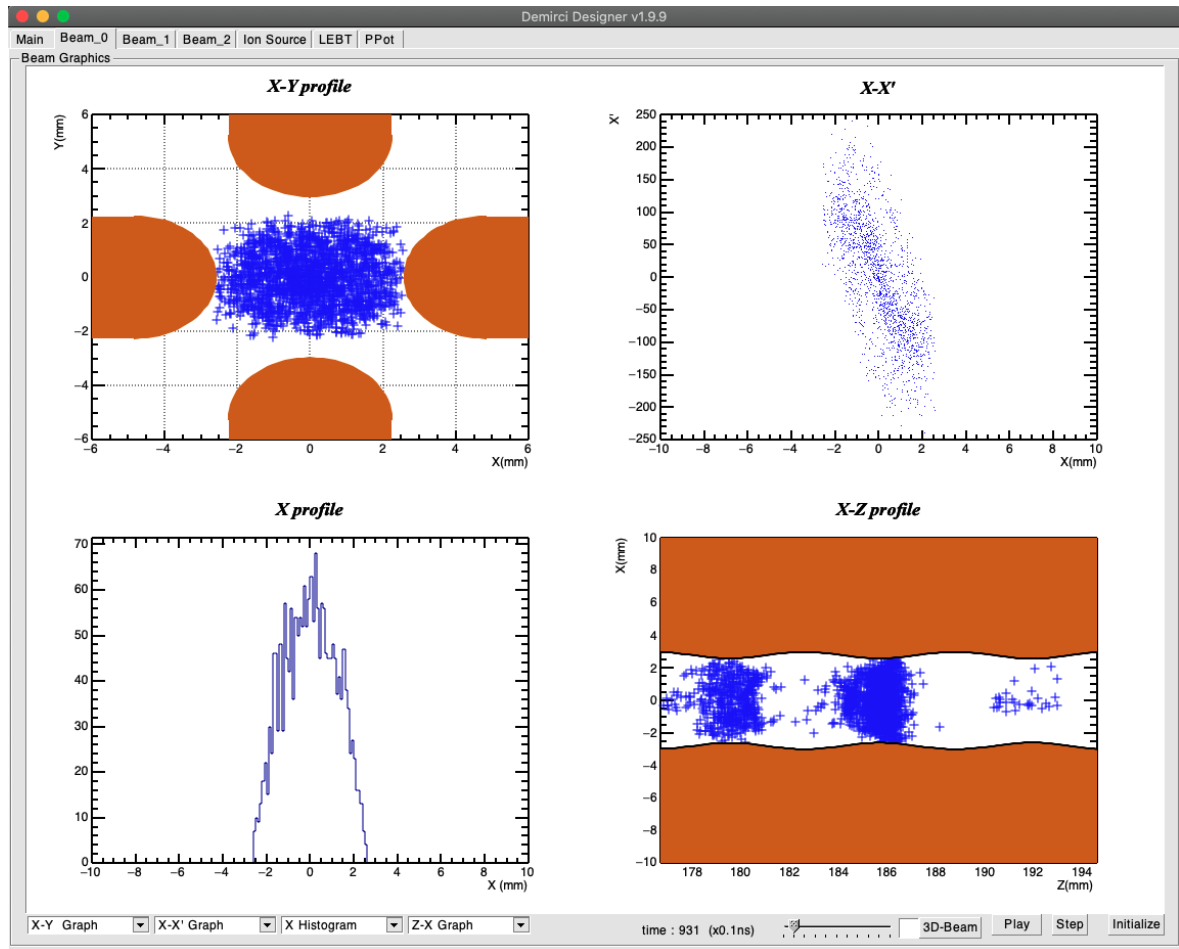


Figure 3.11. DemirciPro beam-dynamics tab.

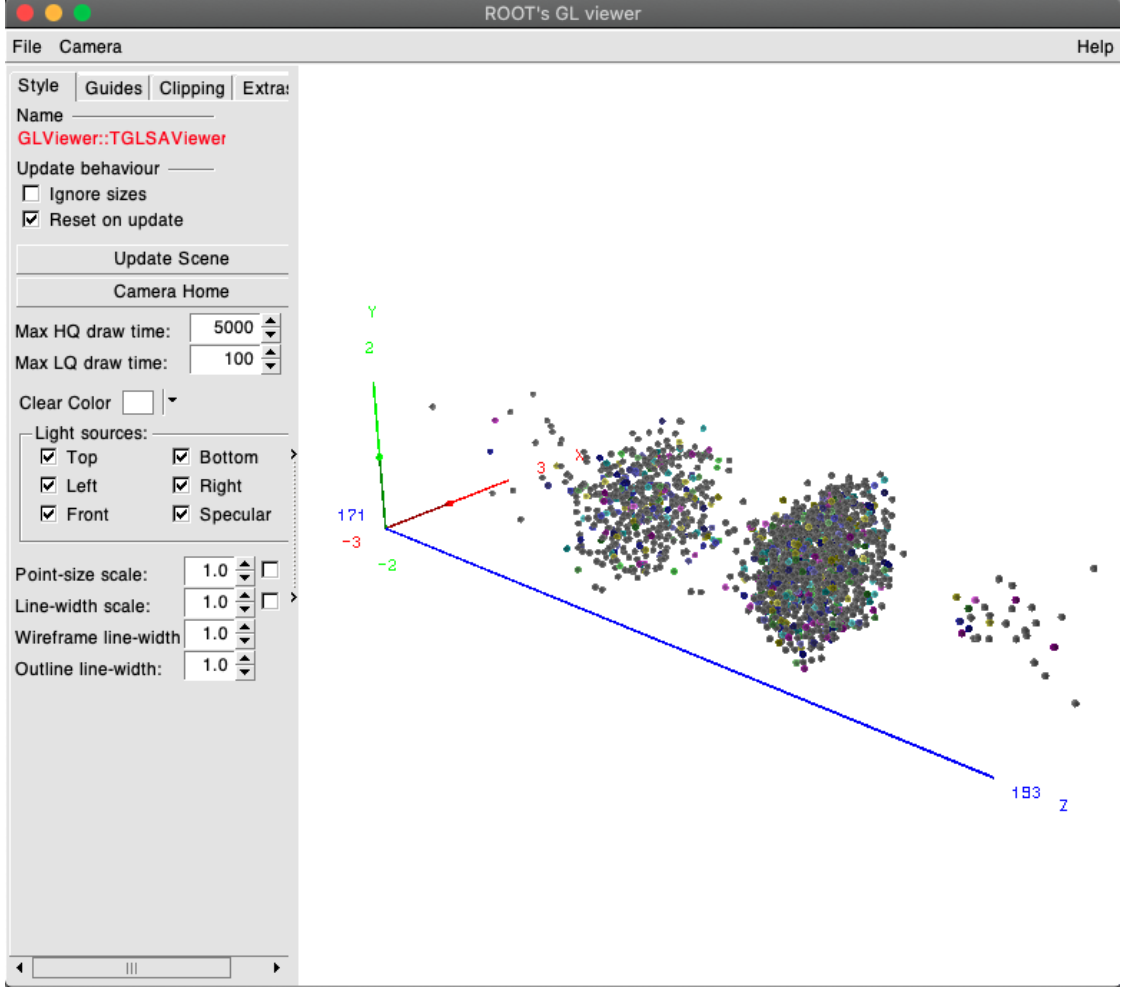


Figure 3.12. 3D representation of the particles with DemirciPro.

DemirciPro uses a relativistic leapfrog method [18] to advance particles, which updates the position, velocity, and kinetic energy at each time step ( $t + \delta t$ ). Equations that are used in update steps can be expressed as

$$\vec{x}^{t+\delta t} = \vec{x}^t + \vec{\beta}^t c \delta t + \frac{1}{2} \frac{Q}{\gamma^t M} \vec{E}^t \delta t^2, \quad (3.1)$$

$$\gamma^{t+\delta t} \vec{\beta}^{t+\delta t} = \gamma^t \vec{\beta}^t + \frac{1}{2} \frac{Q}{cM} \delta t (\vec{E}^t + \vec{E}^{t+\delta t}), \quad (3.2)$$

$$E_k^{t+\delta t} = (\gamma^{t+\delta t} - 1) M c^2, \quad (3.3)$$

where  $\vec{x}^t$ ,  $\vec{\beta}^t$ , and  $\gamma^t$  represent the position, velocity, and relativistic gamma factor of the macro-particle at time  $t$ .  $Q$  and  $M$  are the charge and mass of the macro-particle, respectively, and  $c$  is the speed of light. The electric field at time  $t$  is denoted by  $\vec{E}^t$ , and  $\delta t$  is the time step. The default value of  $\delta t$  in DemirciPro is set to be 0.1 ns.

3.1.3.1. Calculation of Inter-vane Electric Fields Using Finite Element Method. One can use a simplified electric field (TTP) instead of real electric fields in design. However, accurate results require precise field calculations, and since the geometry of RFQ cells is complex, there is no general analytical solution. Therefore, we decided to create a Finite Element Method (FEM) module for DemirciPro to calculate the fields accurately. To test the feasibility of the FEM, a Laplace problem with a known analytical solution was chosen. The problem was to solve the 2D electrostatic problem with rectangular boundaries, which have similar symmetry to an ideal RFQ cell. We created a toy version of the FEM code and solved the problem without utilizing the symmetries. The problem is a rectangular boundary problem with top and bottom boundaries at +200 V and left and right at +100 V. Our solution is given in Figure 3.13. Upon inspection, we found that our solution exactly matches the analytical solution. Next, we employed the symmetries in the x and y-axis by meshing only a quarter of the problem and solving it, which allowed us to obtain the same solution in a shorter time as we expected.

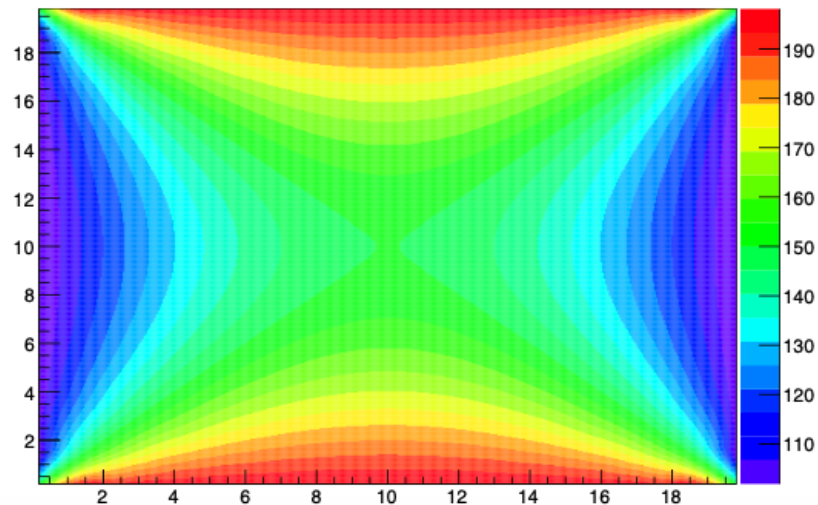


Figure 3.13. The solution of the toy problem.

Next, we built a meshing algorithm for the vane gap using 20 node iso-parametric elements. The algorithm starts by dividing the cell in the  $Z$  to  $D_k$  sections. Then for each  $Z$  value, it calculates the vane positions. If the vane profiles are TTP ones, then

the calculation is done by a bisection method. The vane tip arch and the following taper are created using vane tip radius  $\rho$  and taper angle  $\alpha$ .

To mesh the taper, we divide it into two sections, and the arch has a variable number of divisions based on  $D_j$ . The endpoints of these arches define a new line that is shown in green in Figure 3.14. We then define a new line (shown in yellow) from the origin to the midpoint of the green line and divide it into the same number of equal lengths as the arches. Next, we use the points on the arches and the yellow line to form new lines, which are divided according to the value of  $D_i$ . We apply a similar strategy to the tapered region, resulting in the calculation of all the elements and their node positions. We were inspired by a similar meshing method used in RFQCOEF ([19]), although we do not know the exact meshing algorithm used in that case.

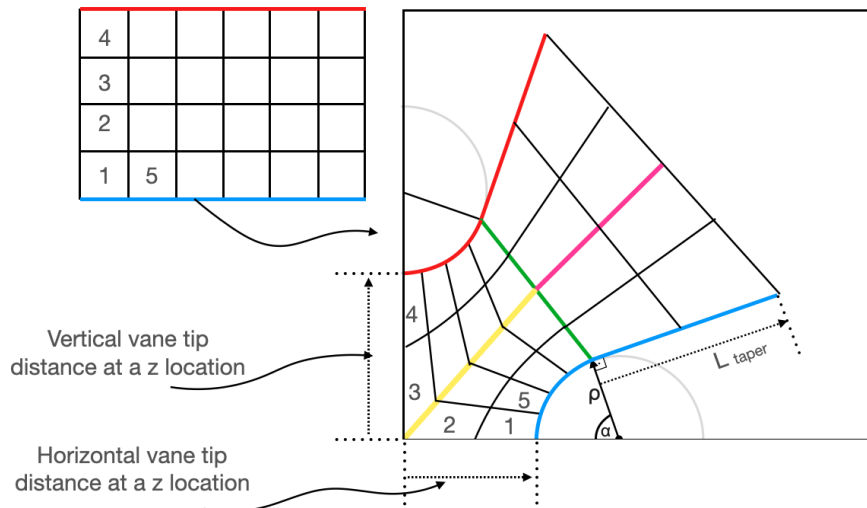


Figure 3.14. Quarter of RFQ cell has meshed with 20 node brick elements in a regular fashion. The nodes are not shown in this figure.

The regularity of our mesh is similar to that of a regular grid, as shown in the figure. If we call the number of nodes in  $z$  direction  $n_z$ , the number of nodes along the electrode surface  $n_e$ , and the number of nodes on the green line in the figure  $n_c$ , the  $D_i, D_j, D_k$  values expressed as

$$D_i = 2n_c + 1, \quad (3.4)$$

$$D_j = 2n_e + 1, \quad (3.5)$$

$$D_k = 2n_z + 1. \quad (3.6)$$

The nodes on the center of an element or the center of a surface are simply ignored. Once the problem geometry is divided into elements and node positions determined, we construct the global stiffness matrix ( $A$ ) that represents the couplings of all the mesh nodes.

As the number of nodes in a matrix  $A$  increases, the amount of memory required to store all its values increases proportionally with the square of the node number. For example, a cell mesh with approximately 1000 nodes would require storing approximately  $10^6$  double precision numbers in memory, equivalent to about 2 GB.

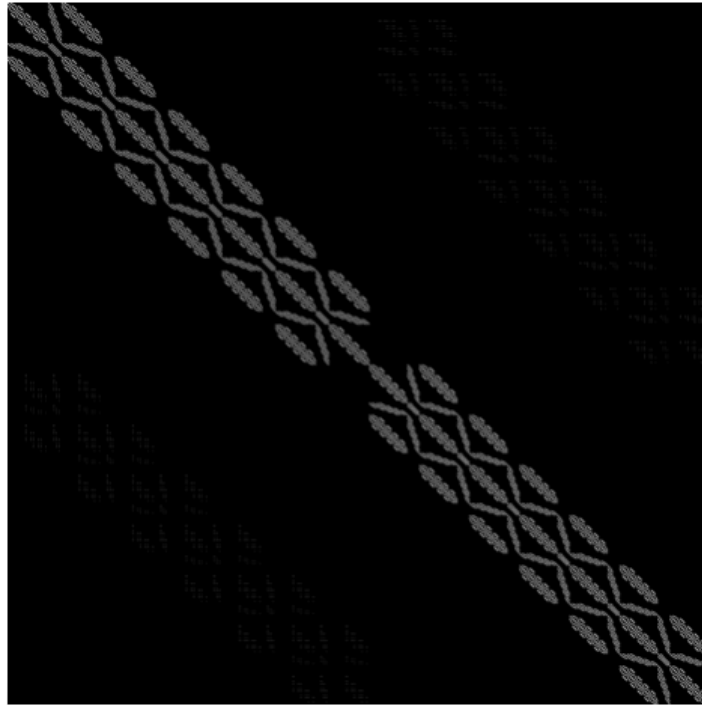


Figure 3.15. A cell mesh connection matrix with zero-valued matrix elements is shown with black pixels, and others are represented with white pixels.

However, each node is coupled to surrounding elements nodes only, meaning that matrix  $A$  has a small amount of non-zero elements compared to zero-valued elements (Figure 3.15). These types of matrices are called sparse matrices. We wrote a Demir-

ciPro library that only keeps non-zero elements in memory with their indices. Then we expanded this library by adding the needed sparse matrix operations. With sparse representation, the required memory changes linearly with the number of nodes.

After meshing and entering boundary conditions, the problem reduces to solve  $A\vec{x} = \vec{b}$  equation as explained in the chapter 2. Here  $A$  is the global stiffness matrix,  $\vec{b}$  constructed by using known node values in boundaries, and  $\vec{x}$  is the unknown node values we want to find. However, since  $A$  is a sparse matrix, we cannot use the inverse matrix method since it would create non-zero matrix elements. Additionally, as the matrix size increases, exact matrix inverse algorithms become computationally unfeasible due to the time they require.

---

**Require:** Initial guess  $x_0$ , right-hand side  $b$ , matrix  $A$ , and tolerance  $\epsilon$

- 1: Compute the residual:  $r_0 = b - Ax_0$
- 2: Set the initial search direction:  $p_0 = r_0$
- 3: **for**  $k = 0, 1, 2, \dots$  **do**
- 4:   Compute the matrix-vector product:  $Ap_k$
- 5:   Compute the step size:  $\alpha_k = \frac{r_k^T r_k}{p_k^T Ap_k}$
- 6:   Update the solution:  $x_{k+1} = x_k + \alpha_k p_k$
- 7:   Update the residual:  $r_{k+1} = r_k - \alpha_k Ap_k$
- 8:   Compute the new search direction:  $\beta_k = \frac{r_{k+1}^T r_{k+1}}{r_k^T r_k}$ ,  $p_{k+1} = r_{k+1} + \beta_k p_k$
- 9:   Compute the tolerance:  $\text{tolerance} = \frac{\|r_{k+1}\|_2}{\|b\|_2}$
- 10:   **if**  $\text{tolerance} < \epsilon$  **then**
- 11:     **return**  $x_{k+1}$
- 12:   **end if**
- 13: **end for**

---

Figure 3.16. Algorithm for conjugate gradient (CG) method.

The conjugate gradient method [27] is widely employed to solve such problems (Figure 3.16). This method does not alter the matrix  $A$  and solves the equation iteratively by guessing the solution. First, it computes a residual vector using the current solution guess, then creates a new solution. This iteration continues until the magnitude of the residual vector decreases below a specific value. Based on our experience, we have found that this method converges to the solution vector  $\vec{x}$  quickly

and efficiently.

Once our FEM code was developed, we tested it by simulating the same cell geometry in DemirciPro and the well-established multi-physics simulation software CST [28]. By comparing the results of our FEM code with CST's results, we could confirm that our code was performing the simulation correctly. Our tests showed that for this specific geometry (Cell 180 from Table 3.1), the results of our FEM code agreed with CST's results with a tolerance of  $\sim 0.1\%$ . We have presented the differences between the two simulations in the form of a histogram with black lines in Figure 3.17.

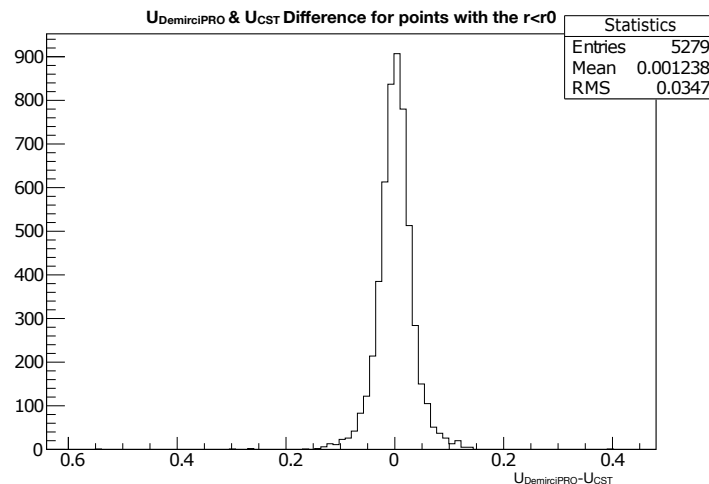


Figure 3.17. The difference between DemirciPro and CST potential calculation results for a test cell (Cell 180 from Table 3.1) is plotted as a histogram. The voltage difference between vanes is 200 Volts, yet CST and DemirciPro results differ by less than 0.2 volts apart from a few data points.

Once the FEM analysis is available, we use the 8 Term Potential (8TP) equation (equation 1.26) to approximate the electric field values at the nodes located inside the minimum bore radius of the cell. First, we perform a least-squares fit to obtain the coefficients for the 8TP equation. This equation provides a quick way to calculate the electric field values inside the cell and is used in the DemirciPro beam dynamics analysis.

Once the 8TP values are available for all cells, DemirciPro can perform beam dynamics studies for an RFQ design. The results are displayed in the beam dynamics tabs at each time step. With these results, the user can identify any issues with the current design and iterate for a better solution by going back to the main tab of DemirciPro.

We also attempted to replicate the results presented in the RFQCoef publication [19] by calculating the 8TP values for five cells (as shown in Table 3.1) and comparing them with the CHRG3D results listed in the same publication. However, our results did not exactly match to result presented. Then we calculated the 8TP coefficients of the same cells with PARMTEQM assuming the table it uses is accurate. Again, our results were not the same as the PARMTEQM but were significantly close compared to other results (Table 3.2). The reported total relative errors defined as  $\epsilon_{tot} = \sqrt{\sum_i (\frac{A_i - A_i^R}{A_i^R})^2}$  where the summation runs over the first 8 coefficients and  $A^R$  represent the reference values. In the case where the reference value is zero, the test value ( $A_i$ ) is used in denominator.

Table 3.1. Definitions of the RFQ cells used for comparison. Minimum bore radius and cell length are in cm.

cell#	$a$	$m$	$\ell_{cell}$
20	0.409	1.020	0.58
60	0.399	1.072	0.60
100	0.392	1.111	0.68
140	0.381	1.171	0.92
180	0.309	1.631	1.94

3.1.3.2. Simulation with External Files. The CST electromagnetic simulation software can simulate particle beam dynamics by using the particle-in-cell method and accounting for space-charge and image-charge effects. The electromagnetic field simulation of the entire vane geometry of an RFQ design is relatively fast compared to full beam dynamics (in our case, it takes days), and even when space-charge and image-

charge effects are ignored, we do not observe a considerable speed-up.

We wanted to compare the beam dynamics results of DemirciPro with CST. By doing so, we can check the compatibility of these codes. If they are compatible, we can use DemirciPro beam dynamics in future studies since it is faster.

Table 3.2. Comparison of the multipole coefficients calculated by available software.

The errors ( $\epsilon_{tot}$ ) are always calculated relative to CHRG3D except for DEMIRCI, which also reports relative to PARMTEQM in parentheses.

#		$C_{10}$	$C_{00}/a^2$	$C_{11}$	$C_{01}/a^6$	$C_{30}$	$C_{20}$	$C_{31}$	$C_{21}$	$\epsilon_{tot}$
		$A_{10}$	$A_{01}$	$A_{12}$	$A_{03}$	$A_{30}$	$A_{21}$	$A_{32}$	$A_{23}$	
20	CHRG3D	0.00606	5.73007	0.05304	4.94852	0.0	-0.00003	0.0	0.00072	-
	RFQCoef	0.00601	5.74846	0.05031	4.41814	0.0	-0.00002	-0.00001	-0.00077	2.32
	ParmteqM	0.00539	5.72978	0.06728	4.9641	0.0	0.00001	0.0000	0.00069	1.36
	DemirciPro	0.00549	5.73015	0.06511	4.92675	0.00000	0.00	-0.00000	-0.00000	1.43 (1.41)
60	CHRG3D	0.02273	5.73981	0.20874	4.89934	0.00000	0.00003	0.00000	-0.00031	-
	RFQCoef	0.02280	5.75573	0.21751	4.51230	0.00000	-0.00006	-0.00001	0.00402	14.32
	ParmteqM	0.02051	5.73962	0.27159	4.98538	0.00000	0.00007	0.00000	0.00134	5.50
	DemirciPro	0.0206495	5.74013	0.26736	4.98026	0.00000	0.00005	0.00001	0.00091	4.13 (1.08)
100	CHRG3D	0.04307	5.74320	0.45675	4.88818	0.0	0.00018	0.0	0.00087	-
	RFQCoef	0.04296	5.85630	0.48357	4.03974	-0.00001	0.00022	-0.00002	0.00628	6.38
	ParmteqM	0.03866	5.74426	0.63987	4.99520	0.00000	0.00028	0.00000	0.00443	4.15
	DemirciPro	0.03896	5.74496	0.63007	5.01070	0.00000	0.00027	-0.00001	0.00262	2.33 (1.08)
140	CHRG3D	0.09684	5.74616	1.40462	4.74544	0.0000	0.00076	0.0000	-0.04081	-
	RFQCoef	0.09662	5.75831	1.35976	3.84250	0.00000	0.00096	-0.00015	-0.09994	1.79
	ParmteqM	0.08634	5.75451	2.64614	4.95261	0.00001	0.00165	0.00004	0.01875	2.51
	DemirciPro	0.08687	5.75461	2.60377	4.95999	0.00001	0.00163	0.00004	0.01968	2.50 (0.51)
180	CHRG3D	0.44918	5.65552	-36.14094	2.36514	-0.00002	-0.04355	-0.10643	-100.715	-
	RFQCoef	0.44807	5.66045	-34.26460	1.44060	-0.00007	-0.04664	-0.10646	-99.0374	2.53
	ParmteqM	0.39947	5.80745	81.02745	3.70216	0.00078	0.05586	-0.03312	-49.50706	40.21
	DemirciPro	0.40167	5.79689	75.01900	3.73725	0.00071	0.05036	-0.03615	-38.81840	36.64 (0.281)

A healthy comparison can be made using the same electric field in both cases. We aimed to accomplish this by importing the electric field data produced with CST to DemirciPro to simulate beam dynamics with both codes' electric field results. CST can export electric fields in a format that contains regularly spaced mesh points and their electric field components. DemirciPro checks the exported data file for irregularities and creates a position-to-index map that provides fast access to the required data points

for interpolation. If there are any missing points in the file, tri-linear interpolation is used to estimate the values for those points.

In our initial studies with tri-linear interpolation with CST exported field, we only allowed z position update of the particles in the beam dynamics. As a result, we observed that the designed acceleration is achieved at the end of the accelerator. We saw that we had lost the beam when we lifted this restriction.

To debug this problem, we started with a test RFQ design and produced a DemirciPro field export data using 8TP values of the cells. The test design is a 352 MHz RFQ with  $r_0 = 2.8 \text{ mm}$ . This LANL-type design is chosen since the PTAK (Proton Testbeam At Kandilli) RFQ has aggressive changes between neighboring cells. We also added a tri-cubic interpolation capability to DemirciPro. Tri-cubic interpolation, which uses 64 data points, is expected to be more accurate than tri-linear interpolation, which uses only 8 data points.

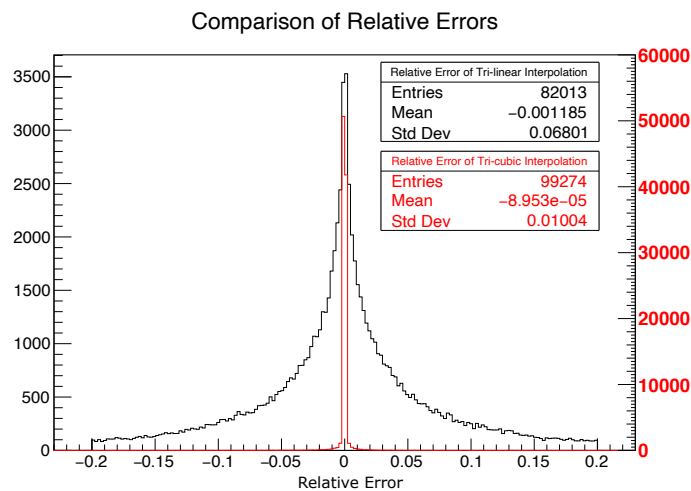


Figure 3.18. Difference between interpolation and 8TP divided with the 8TP. The relative errors of tri-linear(black line) and tri-cubic interpolation (red line) are presented together. The relative errors with absolute values larger than 0.2 were discarded, as most of these stem from sample points with 8TP values close to zero.

(The imported file has 1 mm separation between data points.)

We imported this DemirciPro exported data back into DemirciPro and also we added a field comparison capability to our software. DemirciPro compares the exported field to 8TP values at randomly generated coordinate points in the beam-line volume of the RFQ. Then the evaluated the field values on those points using the two interpolation methods, and the actual values came from cell 8TP values written into a file for inspection.

In Figure 3.18, the interpolation errors (compared to 8TP field values) for these two interpolation methods can be observed. It is worth noting that the tri-cubic method exhibited much better agreement with the actual field values than the tri-linear method.

We observed that the most significant errors come from the end section of the RFQ. To inspect further, we projected coordinates with significant errors of both methods on the x-z plane (Figure 3.19). These errors are situated mainly at RFQ cell boundaries in the case of tri-cubic interpolation where as somewhat uniform in tri-linear interpolation. That hints that there are discontinuities between electric fields calculated for long cells at the test design.

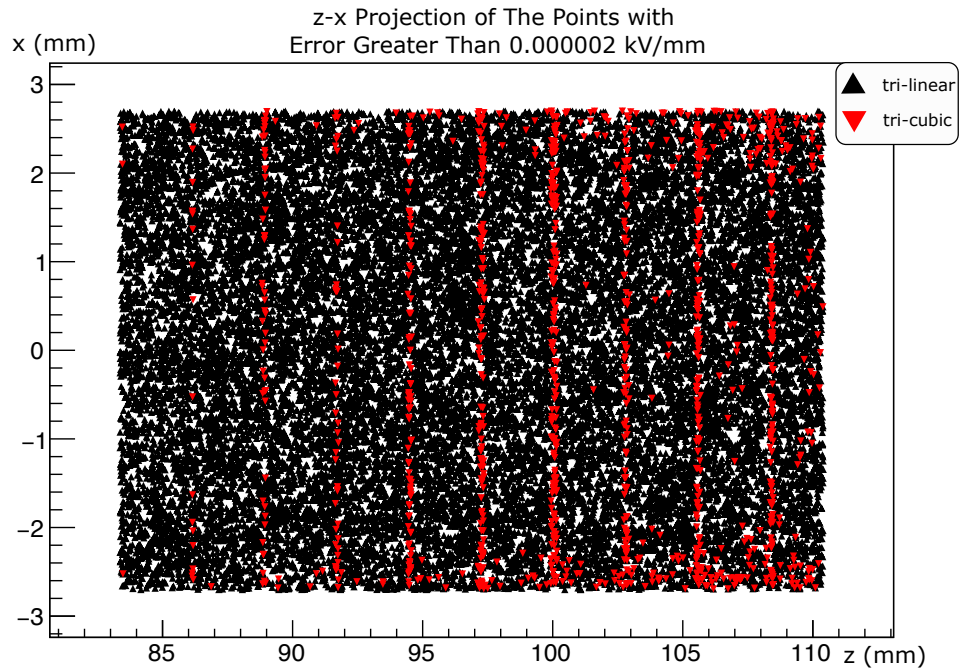


Figure 3.19.  $z, x$  projection of the coordinates with  $E_z$  error greater than 0.000002 kV/mm for tri-linear method (black upper triangles) and tri-cubic method (red lower triangles).

In the center, the errors are rare, as shown in Figure 3.20 for the tri-cubic method (red lower triangles). For reference, the mid-cells of the test RFQ  $x-y$  cross-section are depicted in Figure 3.21 together with the sampling area. Looking at tri-linear method results denoted with black upper triangles in Figures 3.19 and 3.20 (for  $x-y$  and  $x-z$  projections), we can conclude that these errors are more uniform in these cells and infer that these errors are not related to cell transitions at all. Acknowledging the origin of the more significant errors being cell boundaries, we concluded that the tri-cubic method best suits our needs.

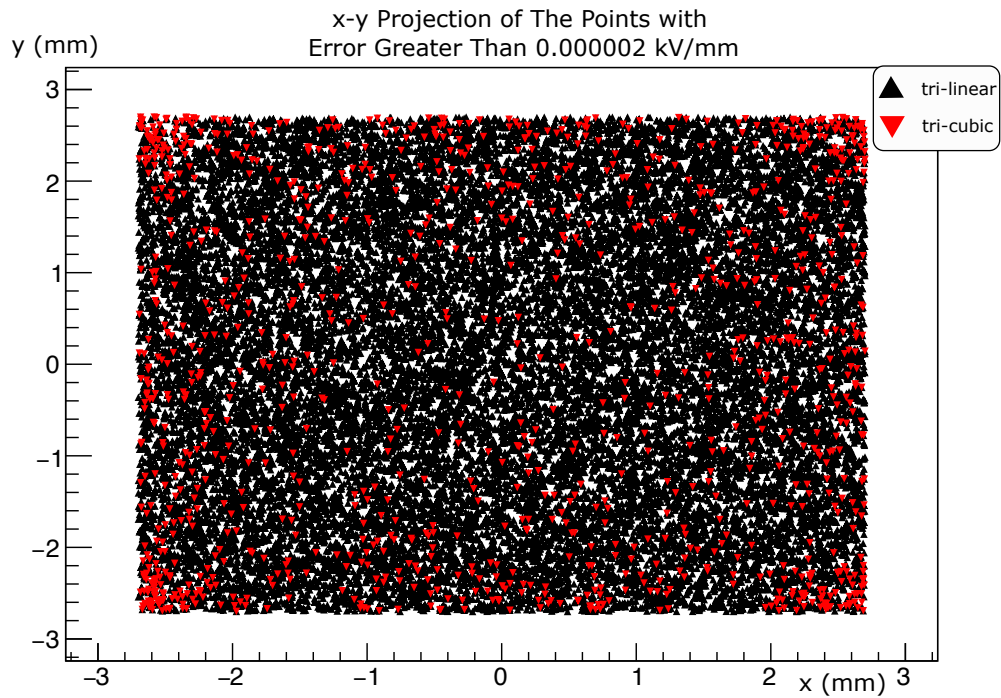


Figure 3.20.  $x, y$  projection of the coordinates with  $E_z$  error greater than  $0.000002$  kV/mm for tri-linear method (black upper triangles) and tri-cubic method (red lower triangles).

We ran beam dynamics with CST-imported data of PTAK RFQ using tri-cubic interpolation, yet we lost the beam again. So this time, we decided to look at imported data. We inspected the cross-section at around  $z = 2\text{mm}$  and plotted the  $E_x, E_y, E_z$  (Figure 3.22). We observed no obvious problems other than a slight mismatch between the  $E_y = 0$  line and the origin.

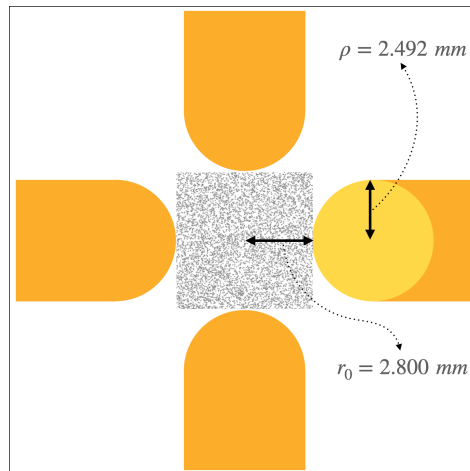


Figure 3.21. The sampled area in  $x - y$  plane depicted in middle of a cell with dotted square. Test geometry is a 352 MHz RFQ, designed with LANL method.

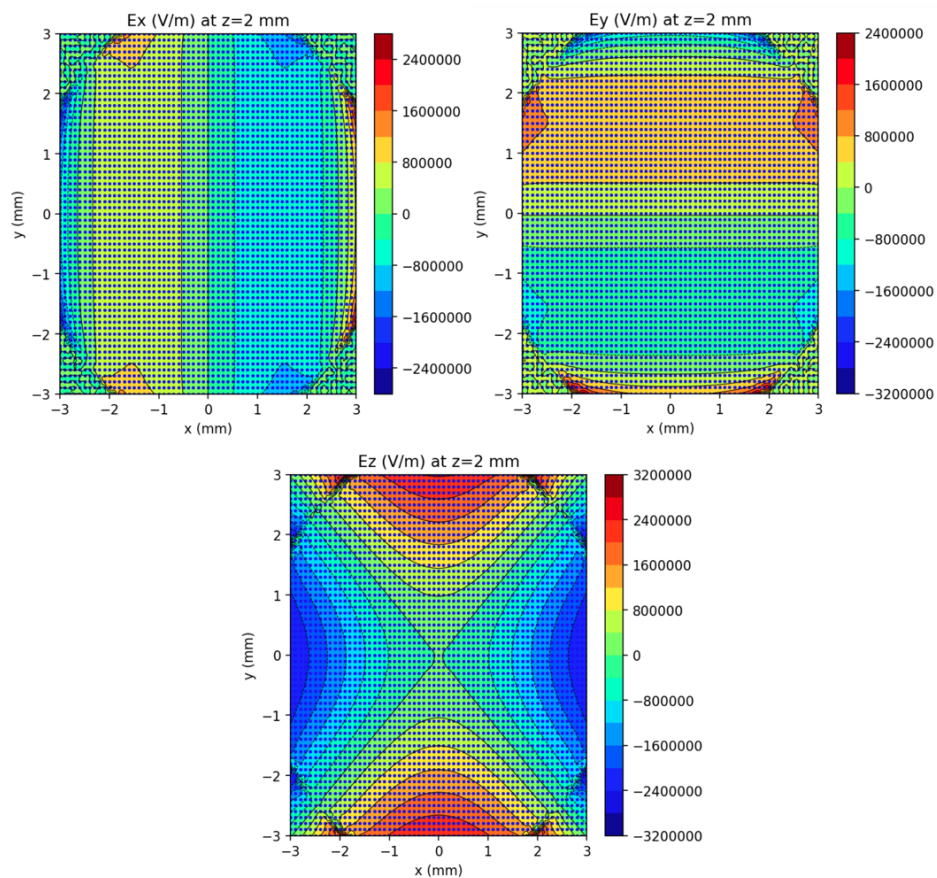


Figure 3.22. The CST simulation of the PTAK RFQ provided the electric field values  $E_x$ ,  $E_y$ , and  $E_z$ . These values are presented in the  $x$ - $y$  cross-sections at a distance of 2 mm from the beginning of the RFQ where  $m=1$ . Inter-vane voltage difference is 33 kV.

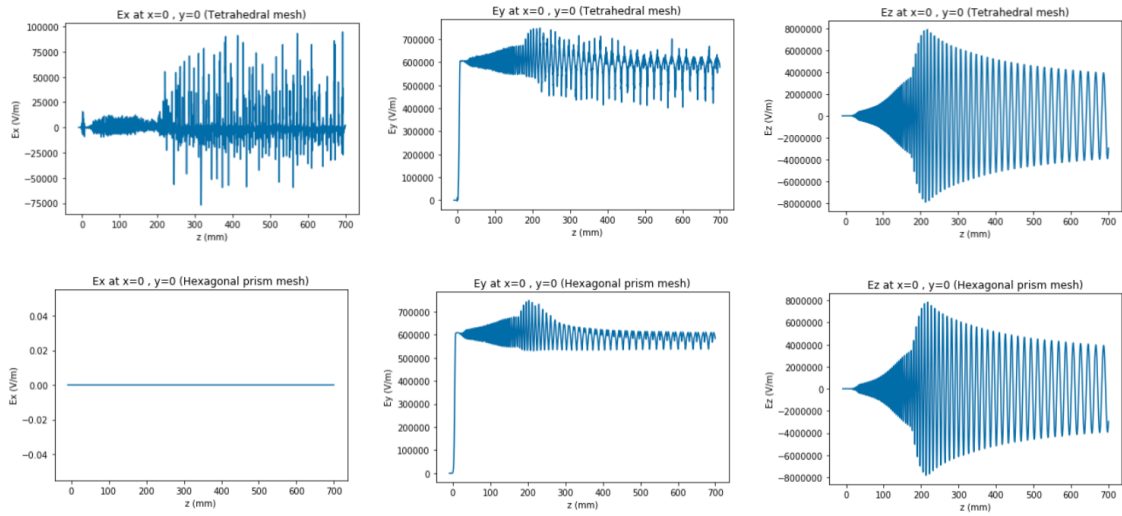


Figure 3.23. CST simulation results with different meshing strategies compared.

Then we draw three electric field components at  $x = 0$ ,  $y = 0$  points. We saw that the same mismatch continues throughout the RFQ. This field calculation is done with hexahedral elements. We have created the same plot with a hexagon prism elements solution (Figure 3.23). Hexagon prism elements eliminated the interpolation error essentially. However, still,  $E_y$  values suggest a shift at the origin.

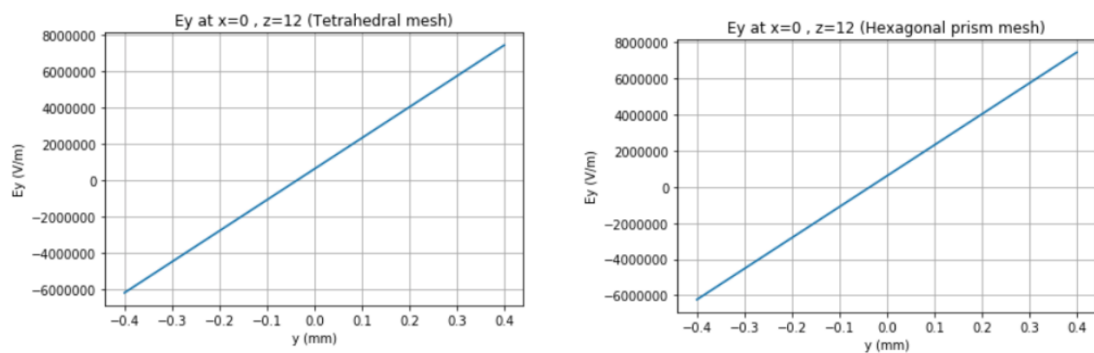


Figure 3.24.  $E_y$  values for  $x = 0$  mm plotted. For both types of meshing, the center seems to be placed to  $x = 0$  mm,  $y = -0.0355$  mm.

We choose the  $z = 12$  mm location where  $E_y$  and  $E_x$  are relatively flat and draw  $E_y$  and  $y$  values for the points with  $x = 0$  mm (Figure 3.24). The position that gives

$E_y = 0$  is calculated as  $y = -0.0355 \text{ mm}$ . We checked both vane positions in the RFQ geometry and export options of the CST but could not identify the cause of this shift.

We conducted Toutatis simulations to determine if the error significantly impacted the beam by adjusting the vane positions in the Toutatis vane file accordingly. However, we found that the slight reduction in acceleration percentage we observed in simulation results could not account for the observed beam loss in DemirciPro. As a result, we plan to conduct further investigations to debug this problem.

### 3.2. The Future of DemirciPro

We are confident that our software, although currently only able to design low current in an integrated environment, has the potential to become a strong competitor for other RFQ design codes. We demonstrated the bunching and acceleration in the test design using the  $\delta TP$  calculated in the DemirciPRO; furthermore, the calculated  $\delta TP$  values were close to those of PARMTEQM. However, we need to fine-tune the existing capabilities, and also, there are several areas that we plan to expand.

We need to incorporate image-charge and space-charge effects into our software to simulate high-current RFQ designs. We plan to use a finite element method (FEM) with simplified beams (pencil beam or point bunch) to calculate image-charge effects. For space charge, we will explore the thick rings method akin to the one used in the SCHEFF routine (PARMTEQM). By combining these methods with  $\delta TP$  calculations, we aim to reduce the time needed for each design iteration and deliver accurate results.

We also plan to develop a code that calculates the field values inside an element. Our meshing strategy reduces this problem to a 2D one, but we will still need to find the natural coordinates of the point in question. We will explore the bisection method to find these coordinates and avoid aliasing problems. Additionally, we plan to adapt our division strategy for RFQ vane profiles, even those not designed in DemirciPro, to avoid aliasing issues.

Also, the field calculation for the entire RFQ geometry is on our agenda. We plan to add the capability of calculating the field values inside an element. We can calculate electric field values in problem coordinates if we know the natural coordinate values of the point in question. Finding those natural coordinates requires finding the root of the complicated 3D map polynomials. However, our meshing strategy reduces this problem to 2D since we can calculate one coordinate readily. We will explore the Newton-Raphson method to find the remaining natural coordinates of a point. Also, we need to avoid aliasing problems while exporting the DemirciPro field data. These problems may arise if we divide the geometry in  $z$  regularly and we plan to use adapting divisions for given RFQ vanes profiles.

Another venue we have already ventured into in PTAK RFQ design is optimization. We plan to implement a similar design procedure. Furthermore, an optimization based on the LANL method of RFQ designing together is also envisioned.

We plan to update the main tab of the GUI to aid the design further. Currently, cell parameters are in separate plots. We want to present them in a single plot with different  $y$ -axis numbering for each variable. Users will be able to activate one parameter change while locking the rest. Current interpolation is linear; this is not desirable. We plan to use centripetal Catmull–Rom spline [29].

We have already analyzed the PTAK RFQ's error using PARMTEQM and Tou-tatis. We plan to upgrade DemirciPro using the gained experience. We can examine the effects of changing input beam parameters, vane voltage, or operating frequency in DemirciPro. However, we assumed horizontal and vertical symmetries while calculating the potential created by the electrode geometry. We tested a mesh with radial displacements of the vanes, but simulating the effects of vane misalignments and irregularities will require new studies on both the mesh of the cell and the fitted function.

## 4. PROTON TESTBEAM AT KANDILLI (PTAK) AND 800 MHZ RFQ DESIGN

The PTAK beam line starts with a microwave discharge ion source with a two-electrode extraction scheme. The proton beam generated by the ion source is then transferred and measured using the low-energy beam transport (LEBT) section, which consists of two solenoids, two steerer magnets, a beam pipe, and a measurement box. Particles exiting LEBT will be accelerated from 20 keV to 2 MeV with PTAK RFQ. A picture of the PTAK beam-line can be found in Figure 4.1.

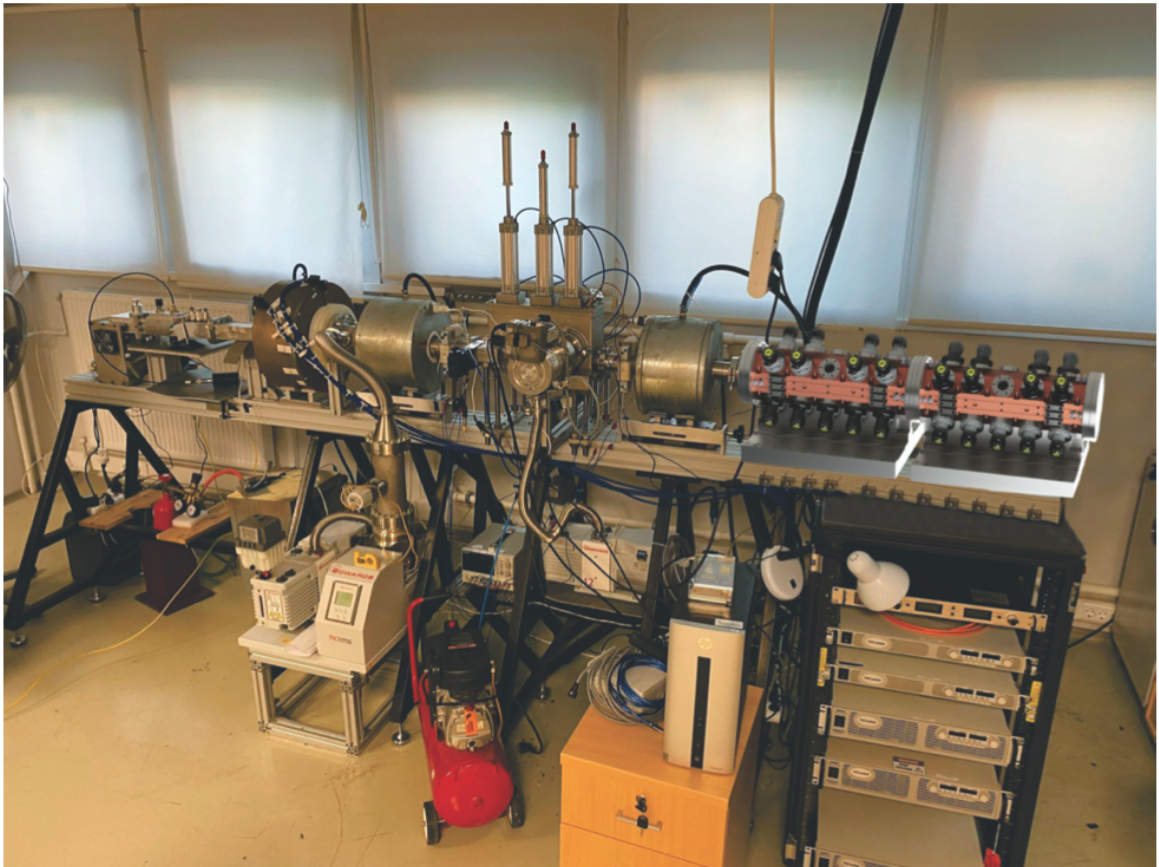


Figure 4.1. PTAK beam line with virtually added RFQ.

The RF power for the IS is generated by a commercial 2.45 GHz magnetron and delivered by RF wave guides (Figure 4.2). These wave-guide components are designed

in KAHVELab and produced locally as the IS itself and LEBT components. The latest measurements show that the system yielded 0.03 mA peak current at a 0.4 duty factor. A detailed explanation and measurements of the IS and LEBT can be found in the article referenced as [12]. Apart from shape changes in the aluminum extraction electrodes, there were no problems requiring the redesign of any part.

Additionally, a permanent magnet microwave discharge ion source has been designed and produced. Its initial tests were successful, and after completion of all tests, it will replace the old IS, which uses a water-cooled solenoid magnet. This new design will reduce spark events and release the previous IS's chilled water budget and current supply unit to be used elsewhere. A recent publication on this work, referenced as [30], presents the design, production, magnetic measurements, and initial tests of the new permanent magnet microwave discharge ion source.

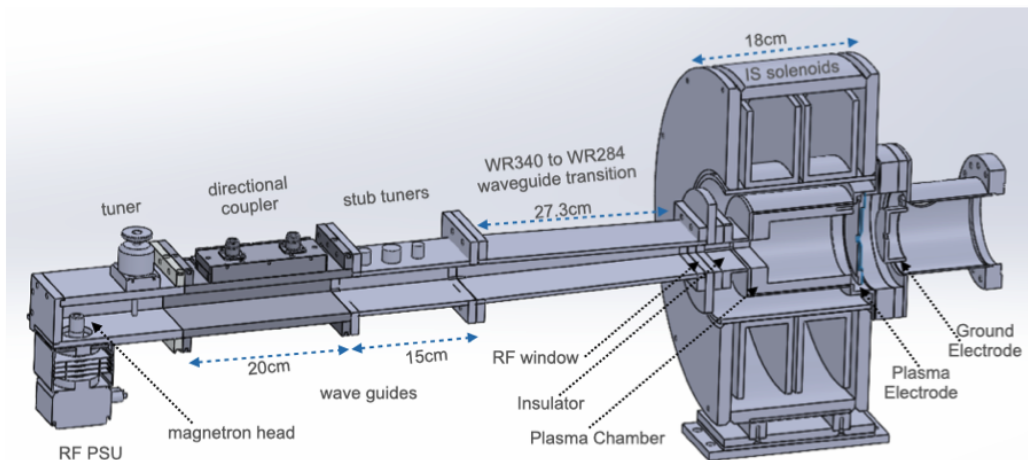


Figure 4.2. PTAK Microwave Discharge Ion Source design

#### 4.1. PTAK-RFQ Design Objectives and Limits

The RFQ we set sight to design will be operated at 800 MHz. This frequency is higher than any operational such accelerator that works with a normal conducting radio frequency cavity. As the resonant frequency of the structure increases, the size of the structure decreases, making it more challenging to manufacture accurately.

The chosen geometry for our RFQ is hexagonal. The cross-section of the resonant cavity can be seen in Figure (4.3). The vane tip radius is 1.392 mm, and the average distance of the vane tip to the beam axis ( $r_0$ ) for the cells is also 1.392 mm. The  $r_0$  value and inter vane-voltage are kept constant in all cells. Keeping the  $r_0$  and inter-vane voltage constant creates a constant focusing parameter ( $B$ ) for all cells; furthermore, this design choice also simplifies both tuning and the verification measurements of the RFQ.

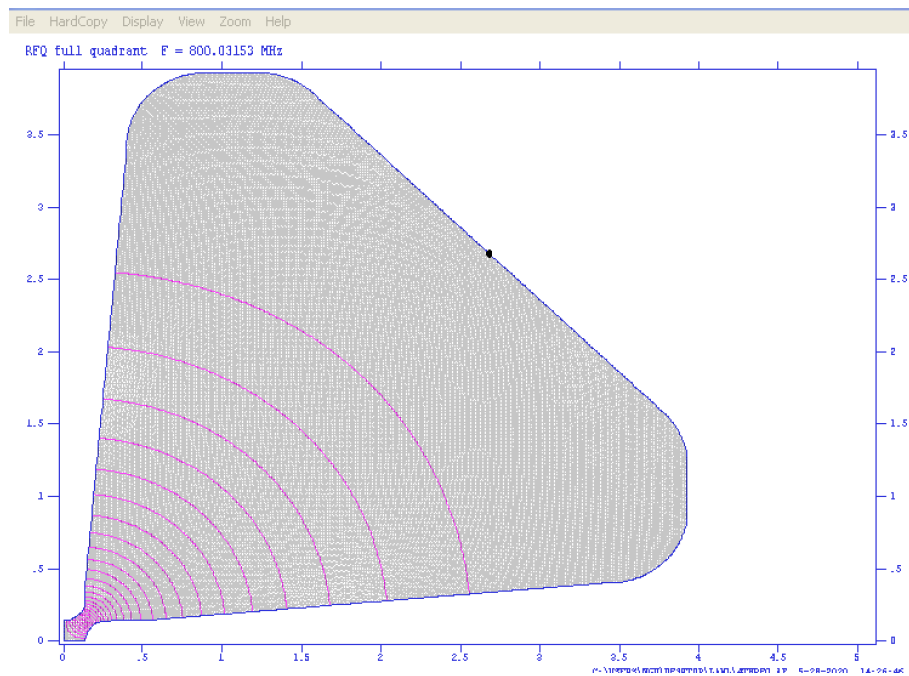


Figure 4.3. SF representation of Quarter RFQ cross-section.

However, there are practical considerations that we need to take into account. Our RF power source has limitations, and we can achieve a maximum of around 70 kW for pulsed operation. In the machinability case, the CNC machine that is available to our private sector partners is limited to max 1.00 m long structure. Moreover, the minimum radius of curvature on tips along the beam axis is 1.40 mm, which is close to the limit to which the CNC tool bit can produce vane tips reliably.

To achieve our design goal of a 2 MeV proton beam, we want a cavity that is approximately one meter long (shorter is better) and can achieve the designed inter-

vane voltage with a power consumption of around 60 kW (lower is better). The radius of curvature of the vanes in the beam direction should also be greater than 1.40 mm. However, the curvature limit has a complex interplay with the length of the RFQ and the available power, making it challenging to design an RFQ that meets all of these requirements.

## 4.2. Initial Design with LANL Method

The classical approach to designing an RFQ would divide the vane structure into four parts. Namely radial matching section, shaper, gentle buncher, and acceleration section. To see how well we could meet our design goals using this approach, we utilized a suite of RFQ design codes called PARMTEQM. We employed both manual and automated methods to run the codes. However, as the code could not function without a GUI (graphical user interface), we had to develop a program to click relevant buttons that controlled the code. The classical approach results were structures that were at least 1.20 meters long and had roughly 30% acceleration of the input beam. However, this design was beyond our power and length budget, and some designs were impossible to produce due to minimum curvature limitations. But this effort was not in vain; we gained a good grasp of the situation and produced some guiding plots as in Figure 4.4.

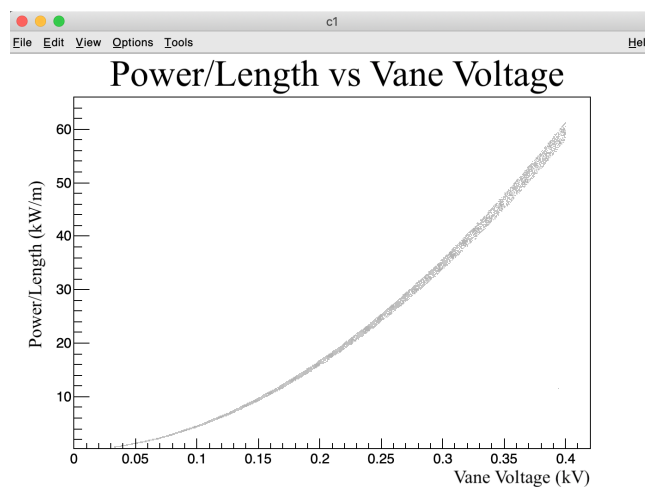


Figure 4.4. Power per meter & Vane voltage comparison.

### 4.3. PTAK RFQ Design

Firstly, we performed an analytical calculation to determine the minimum radius of curvature of a given cell's parameters. We then created a script that maximized acceleration using the estimated energy of particles at the starting point of the cell and returned the cell parameters. At each step, the code calculates the cell length according to the energy of particles, and then it searches (using the bisection root finding method) the cell that has the defined  $r_0$  and the minimum curvature of radius equal to our limit value. These cells replace the shaper and the gentle buncher cells leaving the accelerating structure and radial matching section unchanged. We were able to feed our design into a subroutine called PARI that takes this maximum acceleration design and produces more realistic cell potentials (8TP) using tabulations inside PARMTEQM folders. As a result, a design that is roughly 0.92 m long and has an transmission of 15% (Figure 4.5). This design was used as the starting point for further improvements to get the desired acceleration percentage.

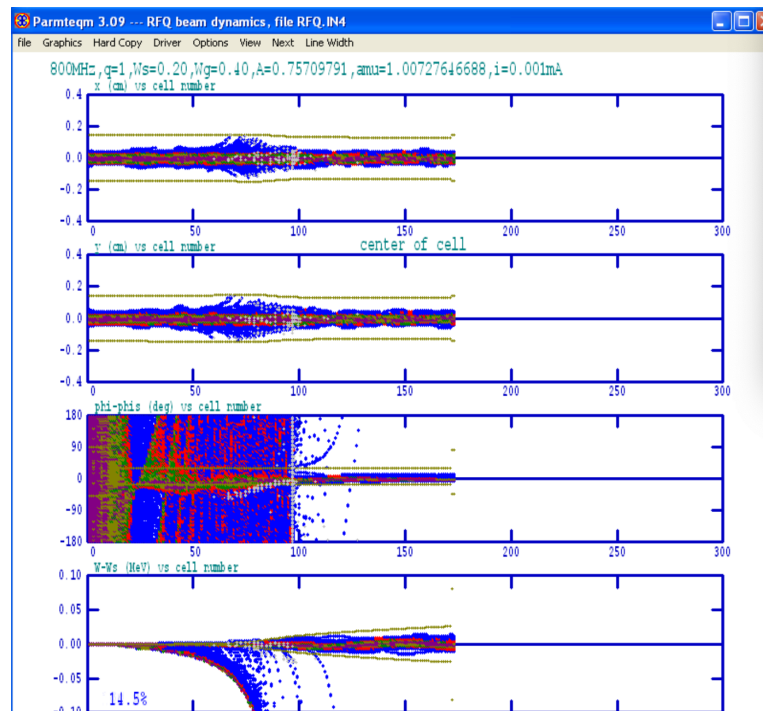


Figure 4.5. PARMTEQM simulation result for the minimum design. The total length of this design was roughly 92 cm.

### 4.3.1. Our Design Approach

We had a design for the shortest RFQ possible, which suggested that we could trade off length and transmission percentage to gain more allowance from both length and power budget. Our goal was to find a design that satisfied all the constraints. We needed to find a curve for the modulation parameter and synchronous particle phase before the acceleration section. In Figure 4.6, our heuristic approach to this problem is depicted. In the right figure, red dots depict the upper limit of the permitted variations of modulation ( $m$ ) on those points derived from the minimum length design. For each position, one value was randomly generated. The lower limits of the random generation were set to the current values of the previous points to ensure that the generated numbers were strictly ascending. For the synchronous particle phase, the only requirement was that it be strictly ascending. We randomly generated phase values and sorted them later rather than using a complicated schema.

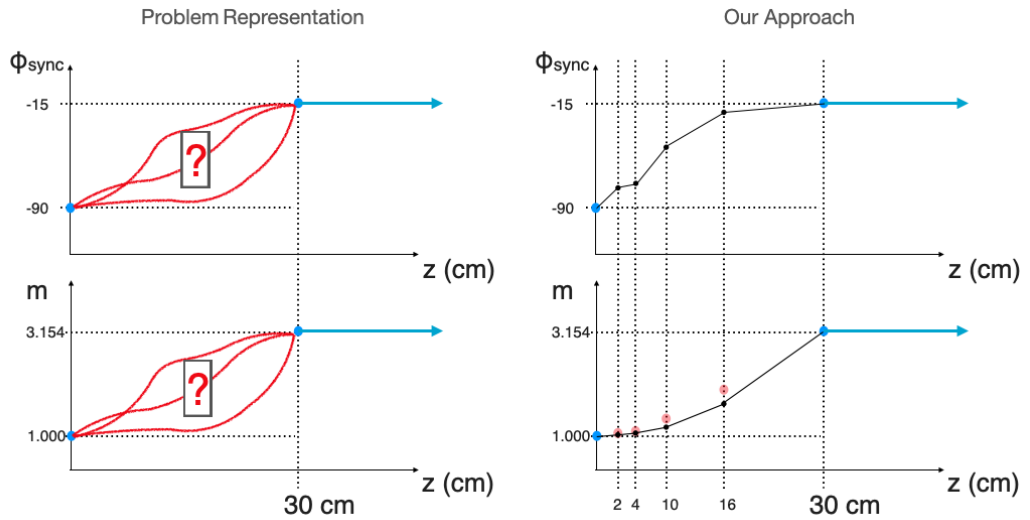


Figure 4.6. On the left, the problem at hand is depicted. On the right, the method of tackling the problem is presented. Red dots represent the upper limit for modulation ( $m$ ) values that are taken from the minimum design.

We made further modifications to our automation code to carry out thousands of simulations with PARMTEQM, while tuning the limits and point positions. After

several iterations of this process, we began to see promising results, as demonstrated in Figure 4.7, for example.

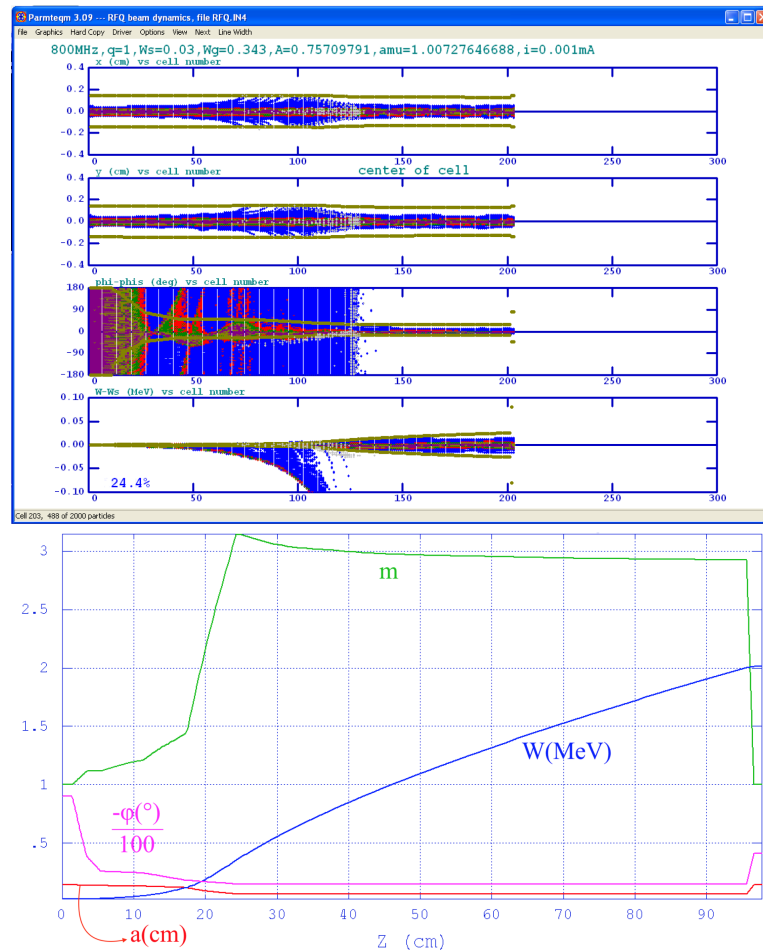


Figure 4.7. One of the first promising results where the 24% of the particles were accelerated. The total length was roughly 1 meter and the intervane voltage was 35 kV.

After a few iterations, we decided to reduce the inter-vane voltage (from 35 kV to 33 kV) of our RFQ by slightly modifying the cross-section of the cavity. Although this modification increased the length of the RFQ, we had enough budget for it, and it reduced the power requirement by a small amount, which might be crucial in practice.

We ran our optimization algorithm again with the new cavity parameters and obtained highly promising designs. After further fine-tuning of the parameters, we

arrived at our final design, which is shown in Figure 4.8. The final RFQ parameters also presented with DemirciPRO in Figure 4.9.

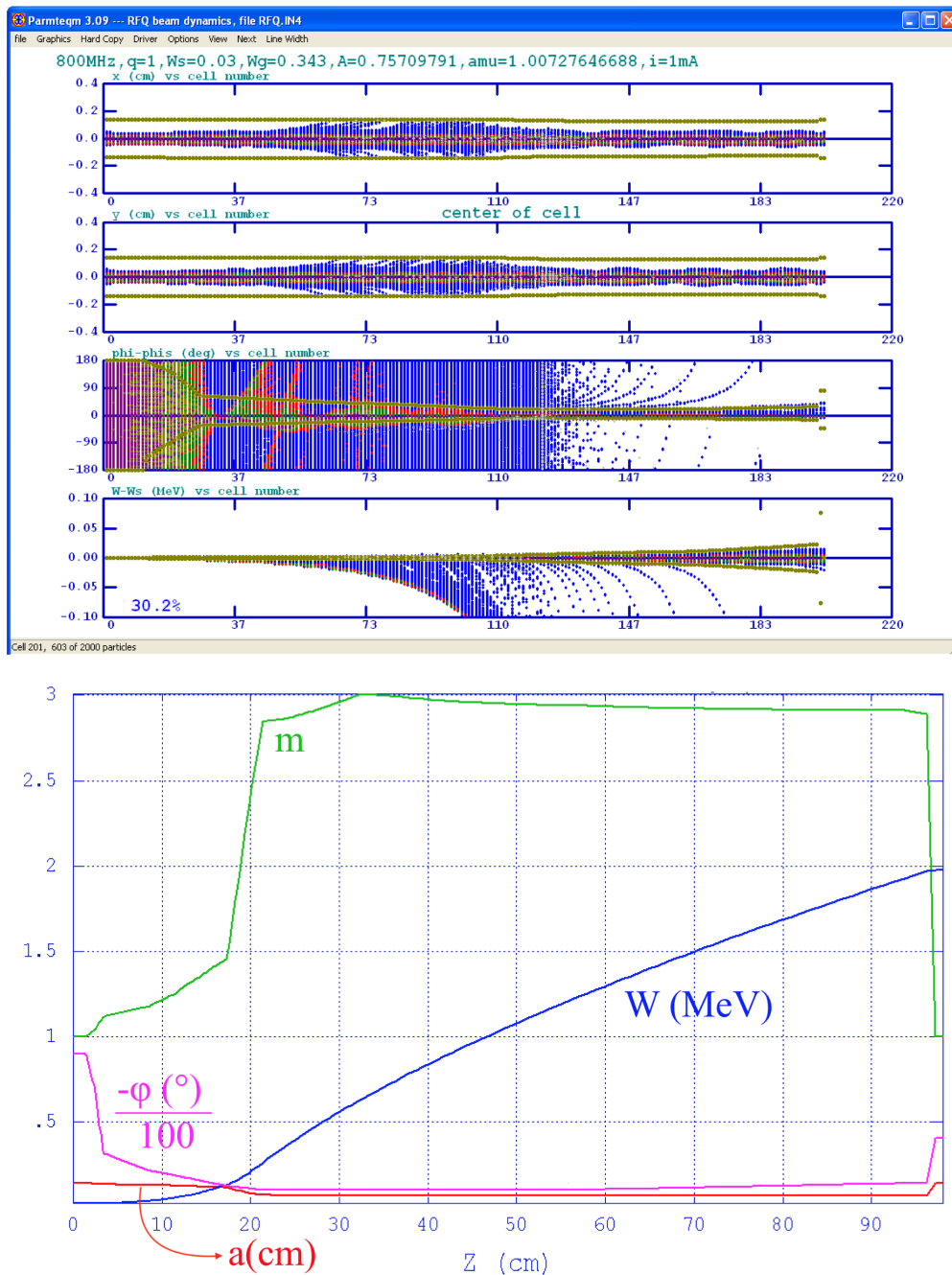


Figure 4.8. The particle simulation results are plotted on the top, and the design parameters are presented in the bottom graph. In the final design, the total length is roughly 98cm. In addition, 30% of particles are accelerated, and the estimated power usage is 58 kW.

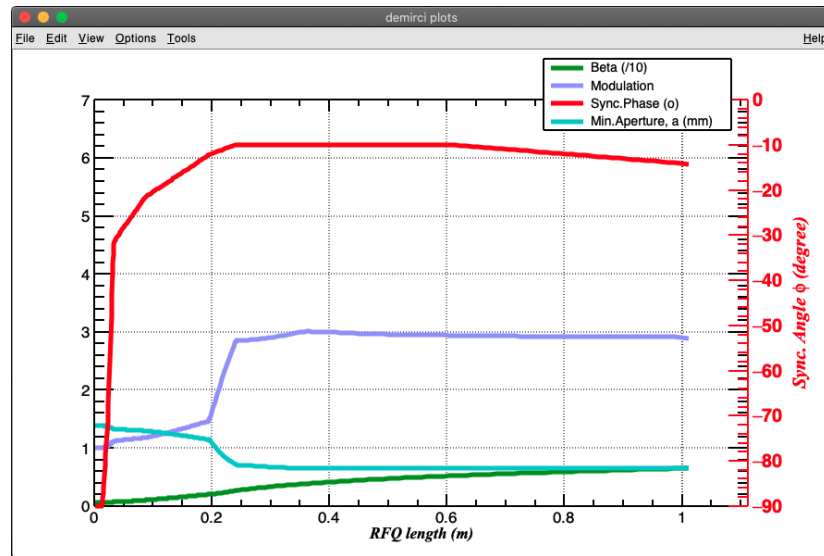


Figure 4.9. A parameter view from DemirciPRO

## 5. PTAK TEST MODULE (MODULE-0) MEASUREMENTS

The PTAK RFQ is designed to operate at a frequency of 800 MHz. This frequency is higher than that of other normal conducting RFQs that were designed earlier. Although a few 750 MHz designs have been produced, our approach to designing and assembling our RFQ is different from those designs.

One significant difference is that we used only commercially available machining bits to machine the copper. In contrast, the machining of the tips is finalized with a specialized cutter for 750 MHz designs. Secondly, in the other designs, all parts are brazed together in a large vacuum furnace. The brazing method seals the vacuum inside the RFQ cavity and the RF power that will be resonating inside the RFQ. We researched the feasibility of this method and tried to find a local organization or firm with such a vacuum furnace. We decided to move on and solve those two challenges separately by using RF Seals and high vacuum-capable 3D o-rings. This decision allows us to build the RFQ locally; furthermore, the RFQ will be easy to inspect since our design can be taken apart and reassembled. Since we want to use these methods in a tolerance-sensitive structure, we want to ensure we can achieve micron-level adjustments of the RFQ vanes and verify them. Test design includes only the first half of the 1m RFQ cavity commissioned. We also designed two end special end-caps with four holes to close the cavity for bead pull measurements. A bead pull measurement was done with the help of a bead on a thin rope. This thin rope helps us to position the bead in the RF cavity. Bead material (in our case, aluminum) perturbs the field created inside, and this effect can be measured via Vector Network Analyzer(VNA).

There are two ways to measure this perturbation, one is to look at the change in the resonant frequency, and the second and more precise one is to look at the change in the phase in S21. The relationship between phase change and field at the

position bead can be found by Slater’s perturbation method [31]. We also took vane tip position measurements from DORA MAKINE [32], the company we partnered with for RFQ production, and used these micron-level measurements to understand if we could predict and reduce machining errors and simulate the beam with these vane tip errors.

### 5.1. Vacuum Test

We conducted a vacuum test using a 3D o-ring, as depicted in the left picture of Figure 5.1, produced by gluing sealant parts together using a special compound. The achieved vacuum was around  $10^{-6}$  mbar, which was a promising result(right picture of Figure 5.1). Furthermore, we plan to repeat the same measurement with an o-ring constructed with a different fusing method. Lastly, a helium vacuum leak test was performed, and there was no leak detected in the mating surfaces of the parts.

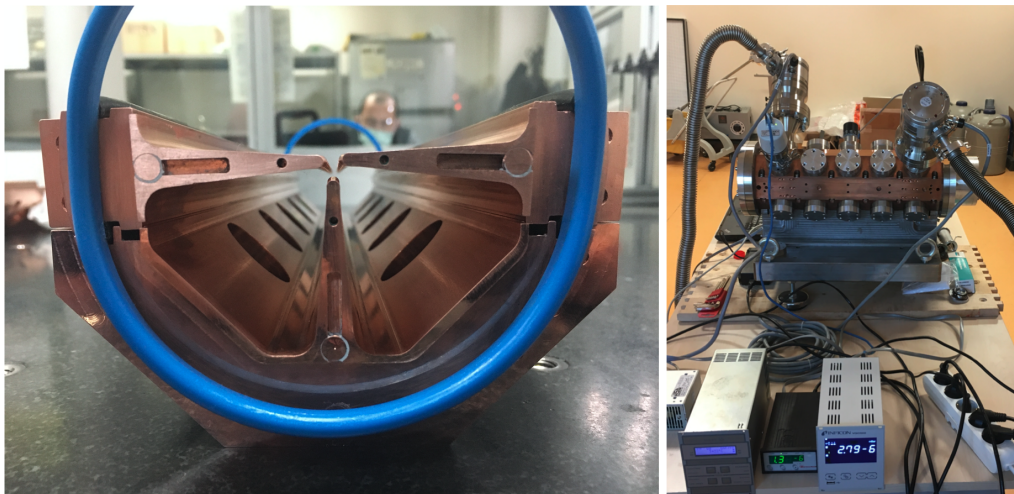


Figure 5.1. The 3D o-ring and its placement in the RFQ are presented on the left, and a picture from the vacuum test is presented on the right.

### 5.2. Beadpull Measurements

When we attempted to assemble the test RFQ parts, we discovered that the channels for the RF seal and the 3D o-ring required more clearance. As a result,

we were unable to adjust the vane alignment to the optimal positions in this setup. Additionally, we realized that when the parts were bolted together, small movements could occur that might compromise the optimal positioning. Furthermore, moving these delicate parts was risky due to their weight and difficulty to handle. To address these issues, we plan to use positioning pins and parts with mating holes (marked with a red circle in Figure 5.2) to aid in the relative positioning of the vanes and serve as handles during actual production.

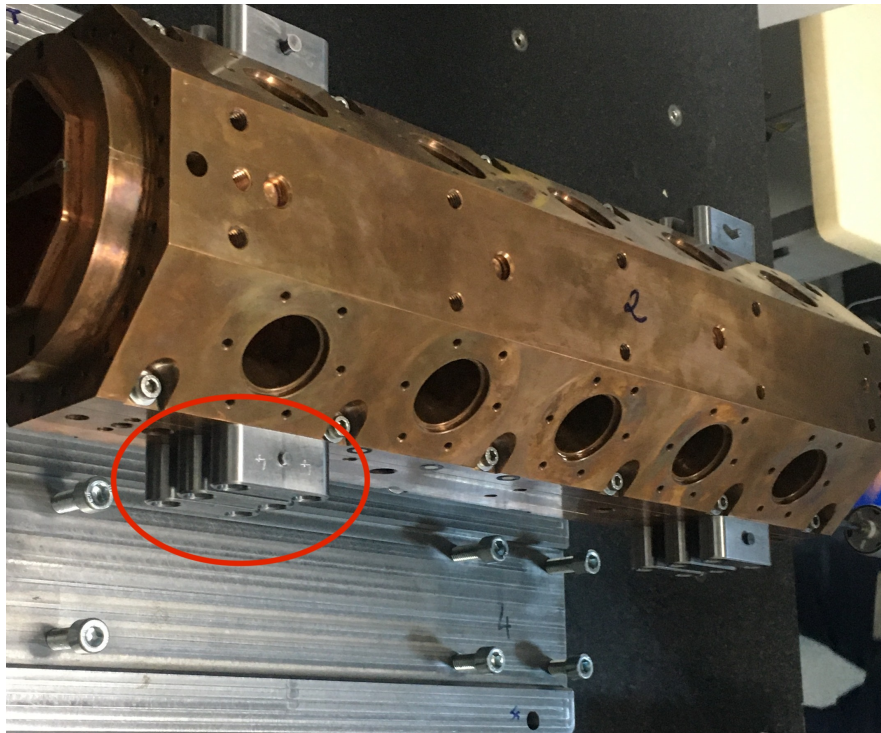


Figure 5.2. The pins and parts were added to the RFQ body to achieve repeatable relative positioning presented. These pins and holes were produced with tight tolerances, and hole positions were determined after vane alignment.

At the time of the tests, the RF seals weren't delivered. As a result, we conducted measurements without them and found that the quality factor was very low due to small gaps between the joints passed RF waves. To solve this issue, we purchased solder wires and inserted them into the channels instead of the RF seals. Although this method may seem unorthodox, it worked effectively, and we were able to achieve a better quality factor, as shown in Figure 5.3.

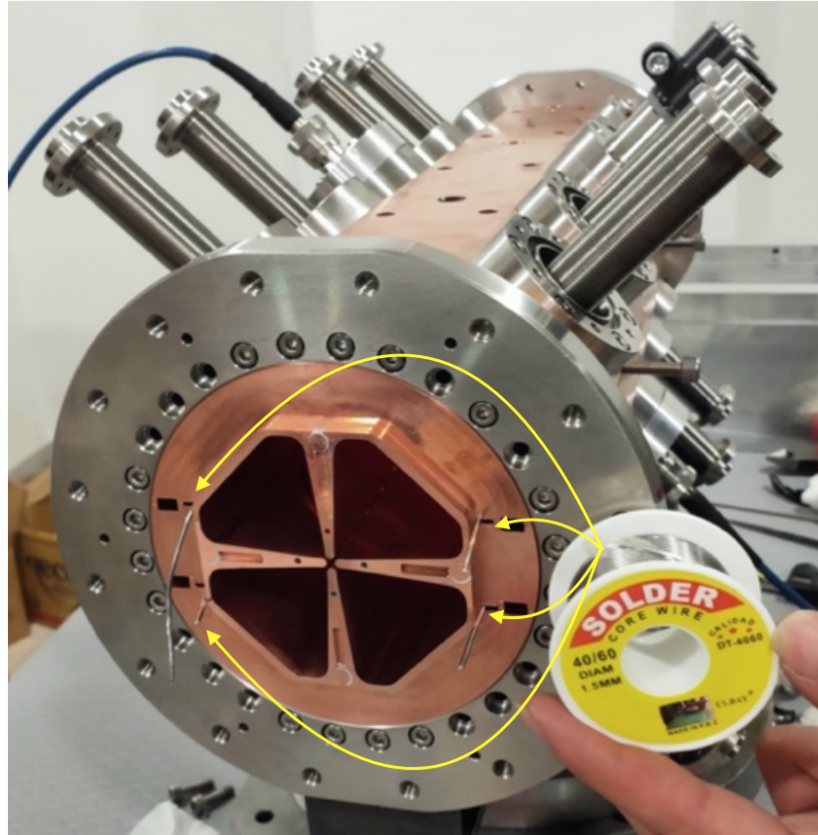


Figure 5.3. Solder wire was used instead of RF seal.

The bead pull setup was initially designed for a pillbox cavity. We modified it so that we could use it in a horizontal orientation and made it longer. Also, we upgraded the LabView [33] code that was written to use the setup. The Bead pull setup (Figure 5.4) moves the tensioned rope that has a small aluminum bead on it with predefined increments. A LabView code was written to send a signal for initiating the measurement to VNA and finally receive the measurement results.

Also, the tests with the old 800 MHz pill box setup showed that the cavity resonant frequency and phase are greatly affected by thermal changes. To monitor these thermal changes, we used a thermal probe and evacuated the test area before the experiments started.

Figure 5.5 shows the results of our first-ever bead-pull measurement. At the time, parts of the tuners were not fully completed, and there wasn't enough clearance

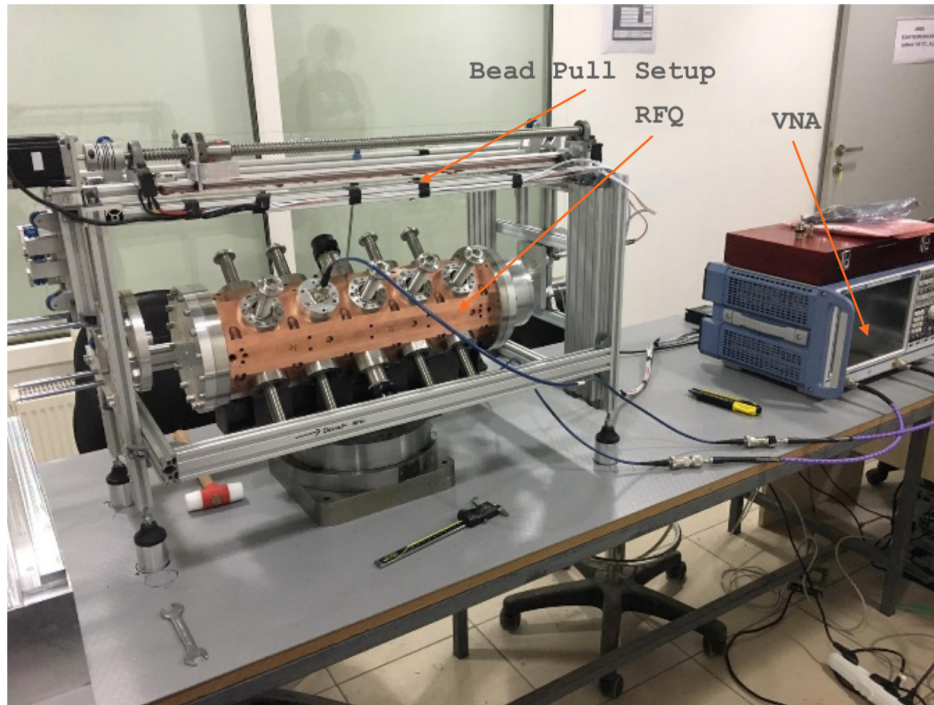


Figure 5.4. Experimental setup for bead pull measurement

to adjust the horizontal vanes slightly. As a result, we could not change the relative positioning of the vanes to each other or adjust the tuners accurately. This caused unequal field values in each part, leading to the poor results seen in the figure. A detailed account of this initial measurement are presented elsewhere [34]. However, a tuning study with better-aligned vanes and installed RF fingers was conducted using the same bead-pull setup [35].

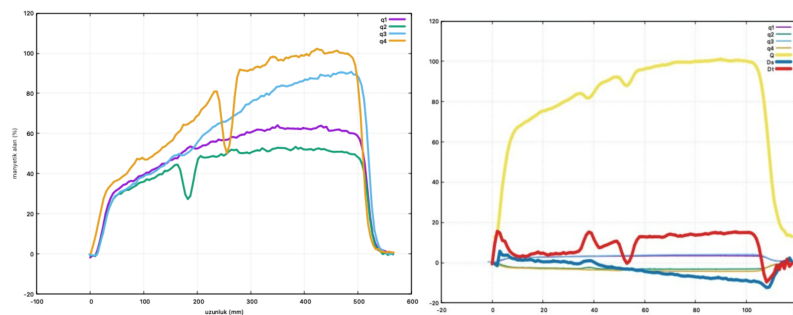


Figure 5.5. On the left bead pull measurements, on the right Calculated Quadrupole (bold yellow) and Dipole (bold red and bold blue) moments along the  $z$ -axis.

### 5.3. CMM Measurements

The production company provided us with the vane tip position measurement data for us to verify. We wanted to compare the measurements to the designed vane geometry. However, we could not directly compare the radial distance measurements since the  $z$ -direction positioning of the data points on the design files and measurements might be different. To overcome this, we used one-dimensional cubic interpolation in Python to create a smooth function of the CMM results. This function, which we called  $F(z)$ , allowed us to retrieve any radial measurement results at any  $z$  position.

Next, we needed to shift these measurement functions in the radial and  $z$  directions to match the design. We accomplished this by defining a new function,  $F_{shifted}(z, a, b)$ , where ‘a’ is the shift in the  $z$  direction and ‘b’ is the shift in the radial direction. We used the SciPy [36] Python [37] package to find the best values for ‘a’ and ‘b’ for the best fit. The results are presented in Figure 5.6.

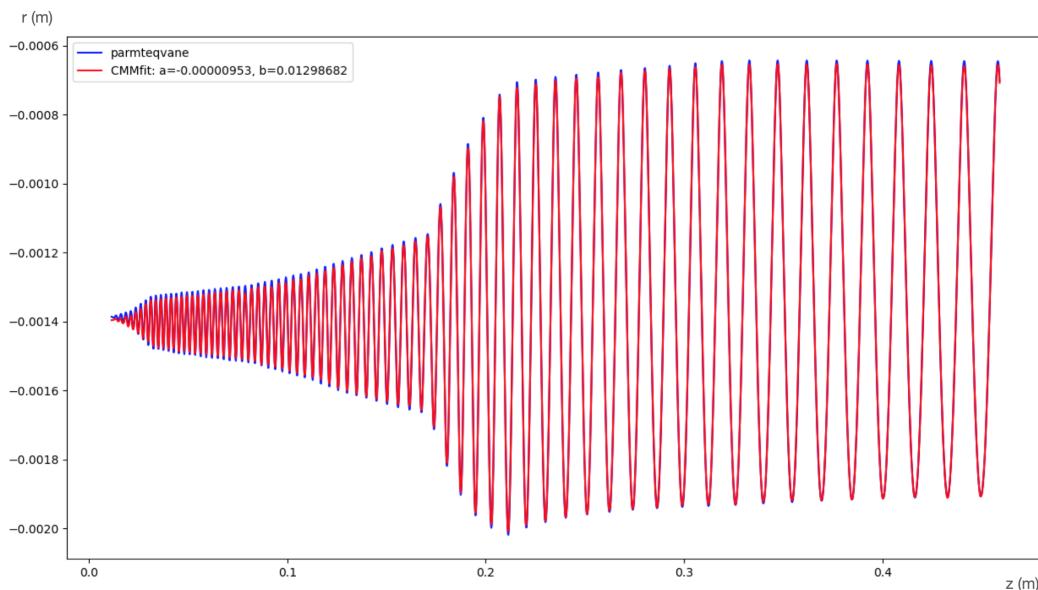


Figure 5.6. Blue lines are the design vane tip coordinates, whereas the red lines are the CMM measurements for the top vane after a fit performed with  $F_{shifted}(z, a, b)$  function. We brought the measurement and design values into the same coordinate system by performing this fit.

The difference of the design vane tip coordinates and measured values calculated for each vane after the fit was performed. These machining errors are presented in Figure 5.7 for the top vane and in Figure 5.8 for the rest of the vanes.

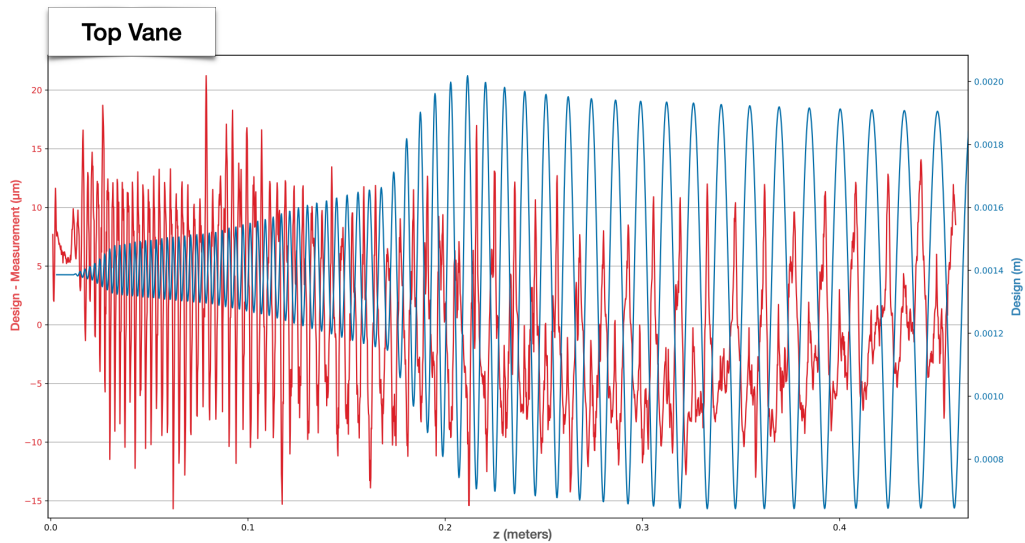


Figure 5.7. Blue lines are the design values for vane tip coordinates. In red we are displaying the difference of measurement from this design values which corresponds to machining errors of the top vane tip.

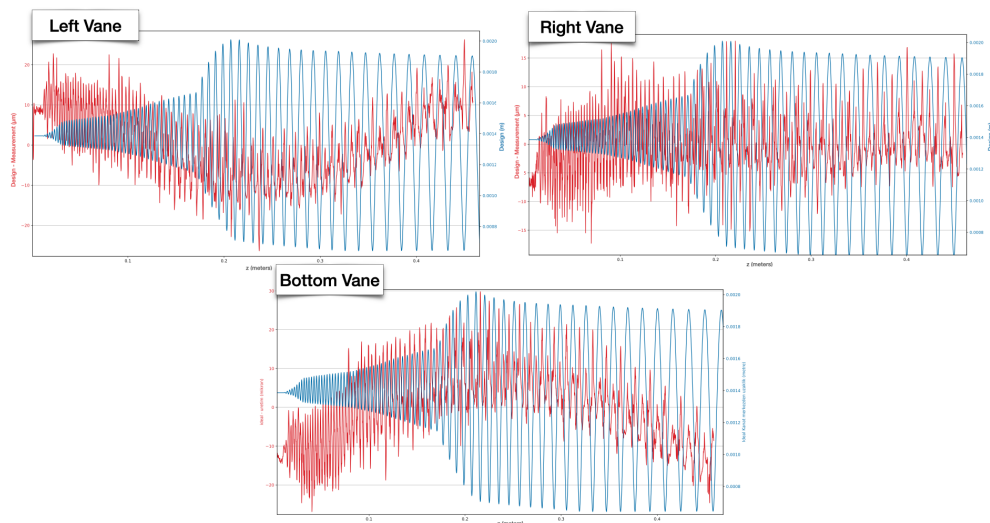


Figure 5.8. Blue lines are the design values for vane tip coordinates. In red we are displaying the difference of measurement from this design values which corresponds to machining errors of the corresponding vane.

After observing the periodic error, we wanted to inspect the dynamic nature of the errors. In this analysis, we interpolated design data, and since the interpolation was cubic, we were able to evaluate the first and second derivatives of  $r$  with respect to  $z$  for the design. We chose the first vane as a reference since it was the one with the smallest errors. We looked for a possible correlation between these derivatives and the errors.

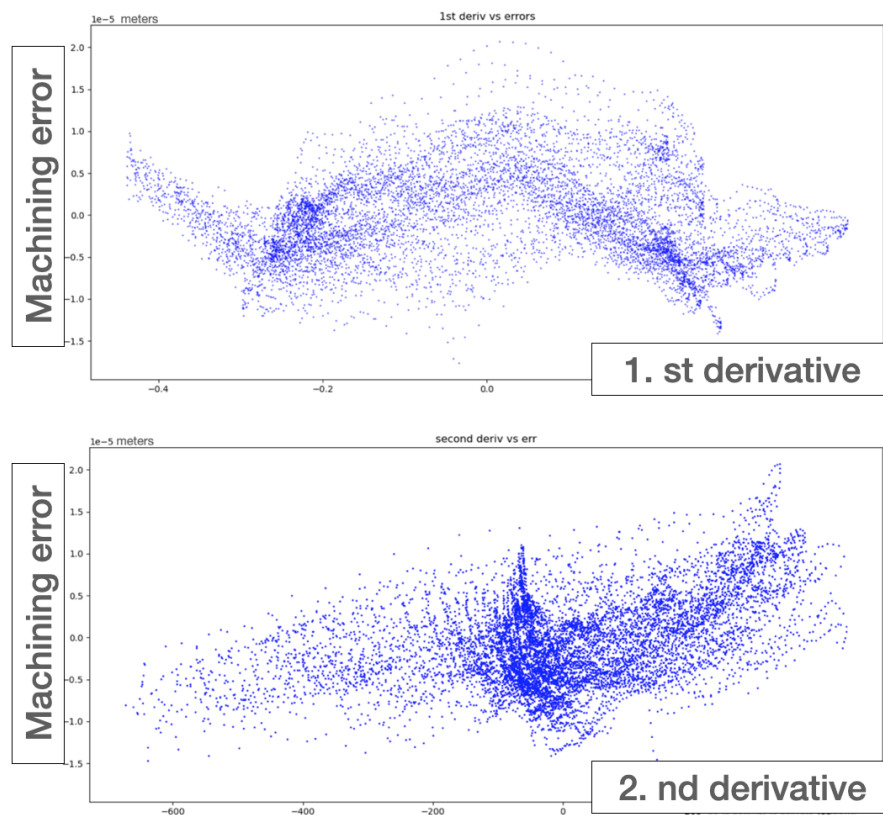


Figure 5.9. The figure shows how errors in machining vary when we consider the first and second derivatives of the vane with respect to its position along the  $z$ -axis. The vane tip coordinates are approximated using a cubic spline then the derivatives are calculated. The relationship between the machining errors changes with both orders of derivatives in a complex manner, as shown in these figures.

We created two graphs showing the relationship between errors and their first and second derivatives. While we didn't find a strong linear correlation, there were some indications of patterns (Figure 5.9). To investigate further, we produced a 3D

plot of machining errors vs. the first derivative and the second derivative. It revealed a complicated interplay between derivatives and error. Points on the plot were not on a single surface; therefore, to understand better, we divided the derivative plane into a grid and calculated the mean, standard deviation, and count of the points that lie on each grid segment. The purpose of the count plot (presented in Figure 5.12) was to make sure that we had enough statistics to infer mean and standard deviations. The idea is that we can use these mean values and make an interpolation in two dimensions (first and second derivative) to define a function most likely machining error values for a given first and second derivative pair (Figure 5.10). But as we can see from the standard deviation plots, there are some first and second derivative pairs with higher standard deviations (Figure 5.11).

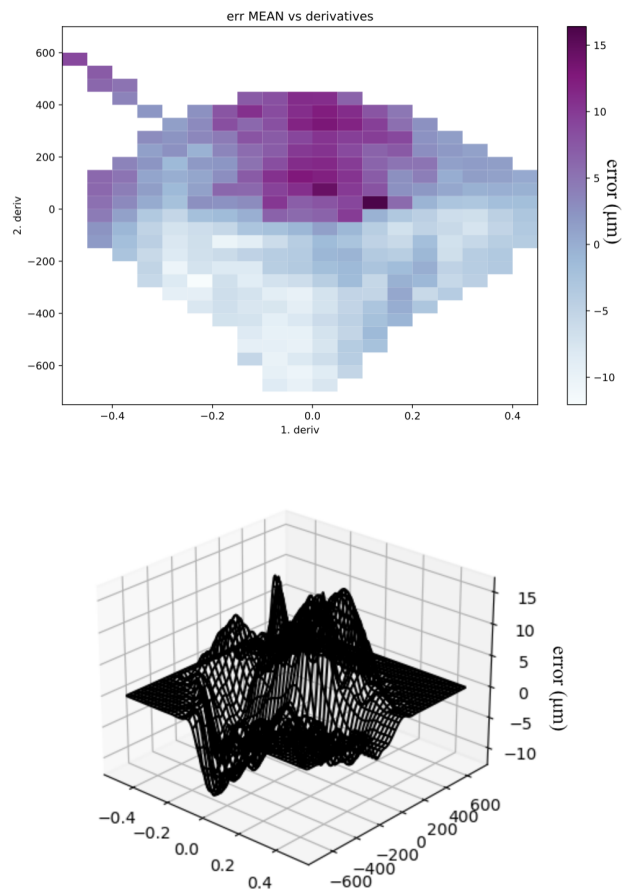


Figure 5.10. Top: Mean values of Machining Errors on the Grid vs. Derivatives. Bottom: 3D representation of the prediction surface constructed from the top plot.

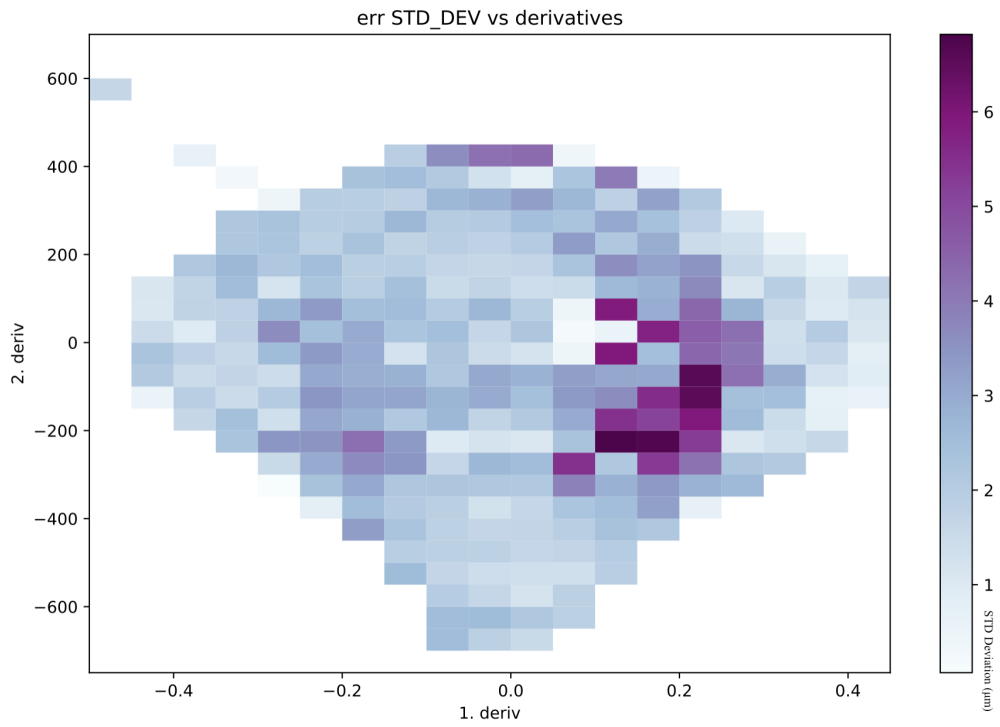


Figure 5.11. Standard deviation values of Machining Errors on the Grid vs. Derivatives.

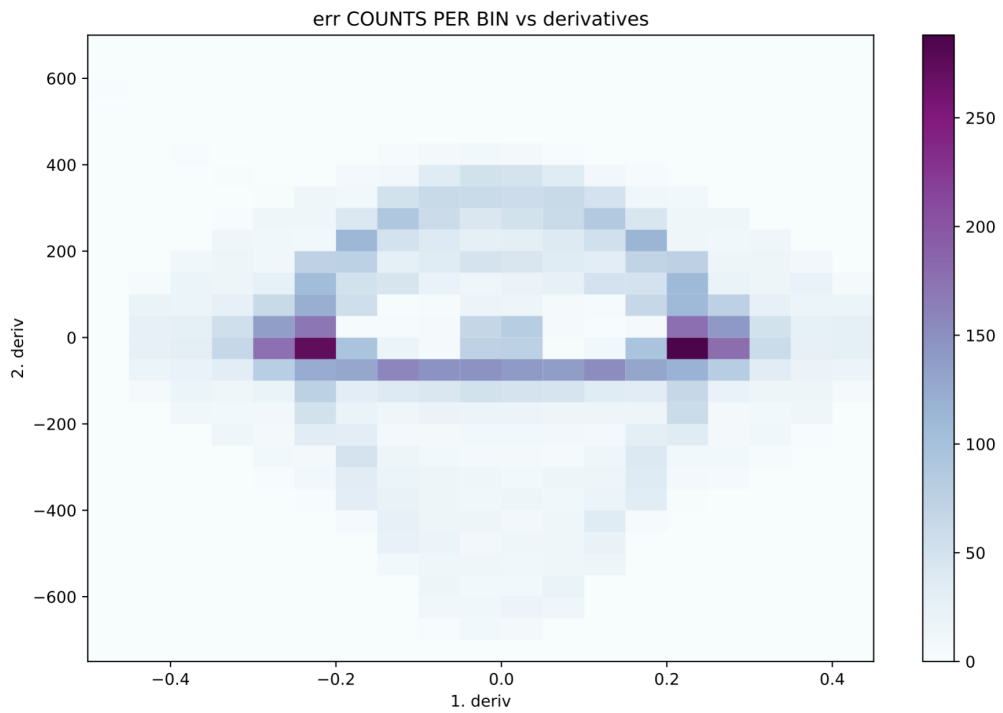


Figure 5.12. Count values of Machining Errors on the Grid vs. Derivatives.

Then we proceed to build a prediction function using mean values, and these predictions are subtracted from the errors of the same vane to see the statistical behavior of the errors. (Figure 5.13).

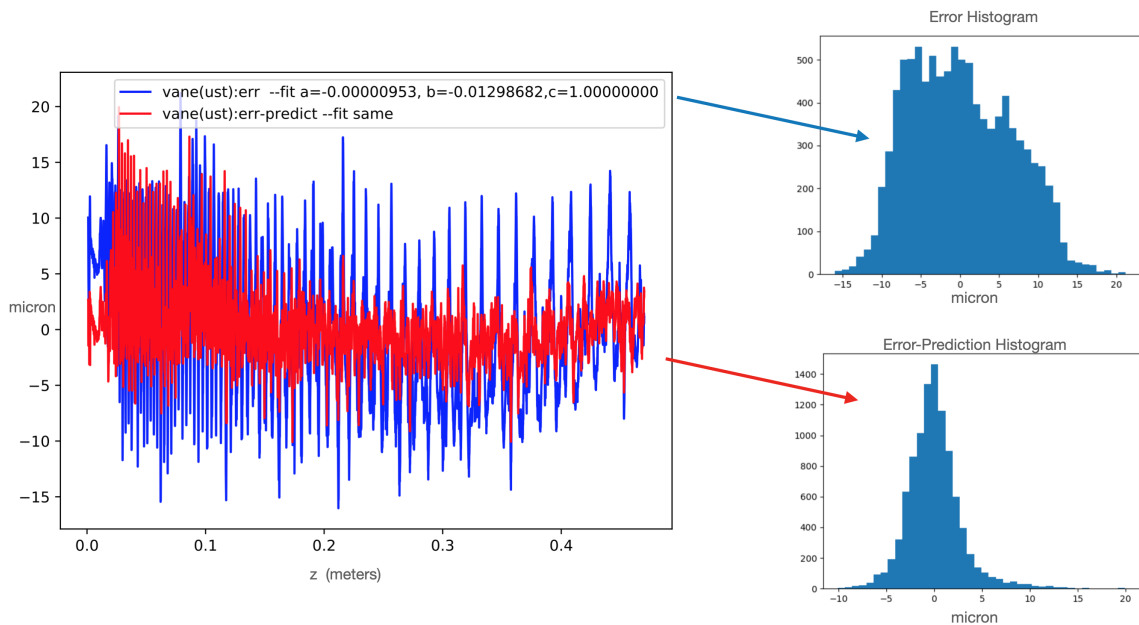


Figure 5.13. Left: Top vane errors and errors after prediction subtracted from measurement overlaid together. Right: Error Histograms from before and after prediction subtraction are shown separately.

We used this function to predict errors and subtract these from actual errors for the rest of the vanes. We can see in Figure 5.14 that after subtraction error profile improves a little bit but not drastically as the top vane.

It begged the question if we can assume all the vanes were produced in the exact same conditions. Since the top vane and bottom vane are symmetrical; also the right vane and the left vane are symmetrical, we compare them to each other. If the process is exactly the same, then the difference between them should be only statistical. To do this time  $F_{shifted}$  functions are modified to express tilt also. We can call these  $F_{shift,tilt}(z, a, b, c)$  with  $c$  being the slope of the tilt. The bottom vane fitted on the top vane using respective functions. That gave us matched CMM measurements. We subtracted them and plotted the difference with respect to  $z$  (Figure 5.15). We repeated

the same procedure with the right and the left (Figure 5.16). This made it clear there is definitely something else in effect.

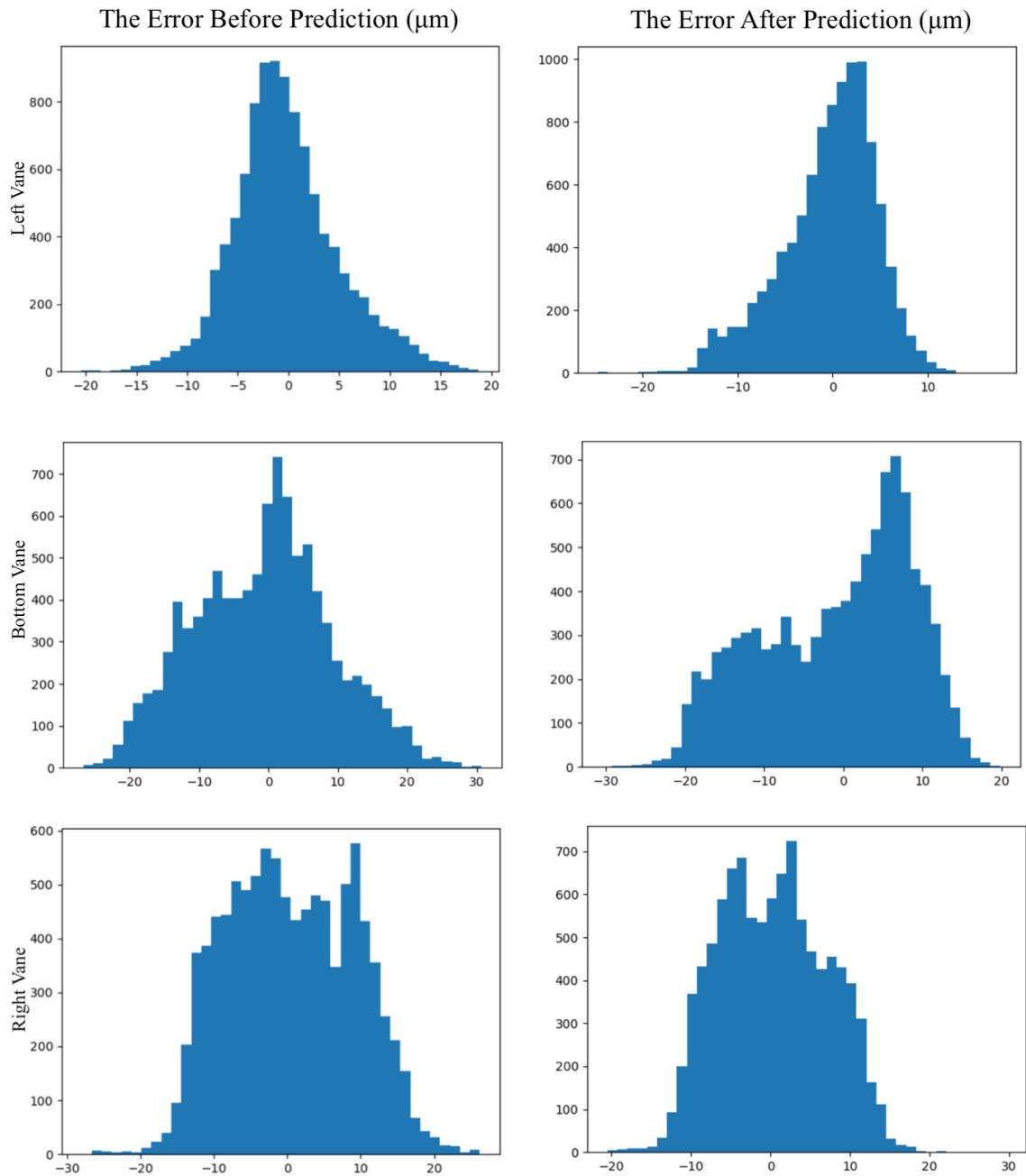


Figure 5.14. From top to bottom: Left, bottom, right vane machining errors displayed before and after prediction constructed with top vane data. The improvement is marginal, if it exists at all. These results suggest that the behavior of errors is different between vanes; therefore, the production process is not identical.

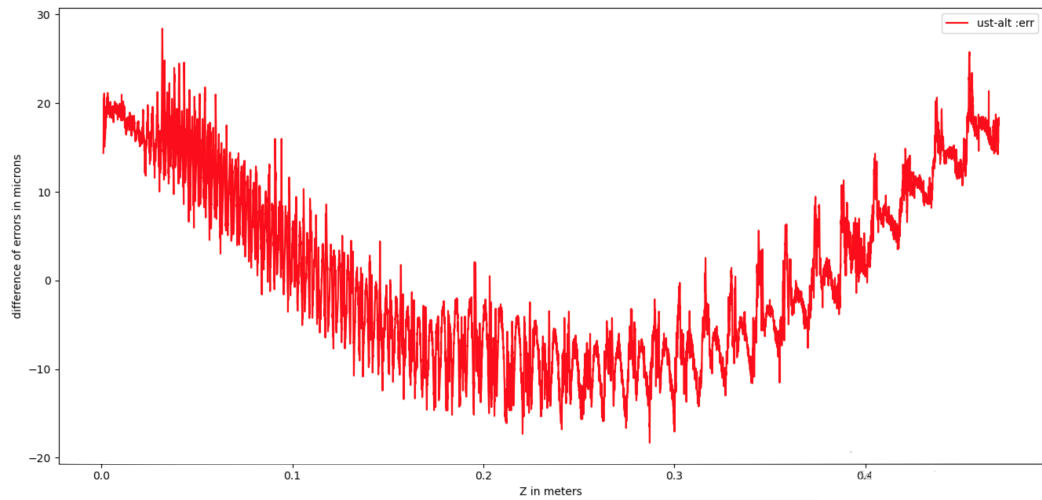


Figure 5.15. Difference of top and bottom CMM measurements after both fitted on the design values of the vane displayed. There are periodic and bowing-like behavior present.

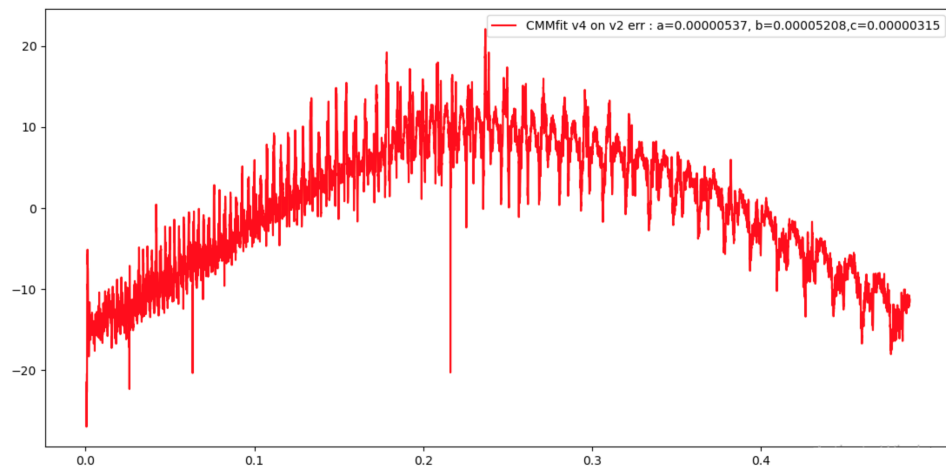


Figure 5.16. Difference of right and left CMM measurements after both fitted on the design values of the vane displayed. There are periodic and bowing-like behavior present.

These results do show an unexpected nature. We would expect flat, random-walk-like results if the production steps are exactly the same. There are a few possibilities, and the most prominent one is the possibility of vanes warping at the center. Measurement misalignment also can produce results like these to some degree.

The module-0 was found to be hard to align in the horizontal direction, which depends on the tolerances of the channels for o-ring and RF seals. Re-machining of the joint surfaces was necessary.

Then the machining operations that are mentioned are carried out. We saw better alignment and consistency on this alignment after subsequently taking apart and reassembling the structure.

All the disassembling, reassembling, machining, and vacuum tests would apply some forces to the parts of the structure. We do not expect any force that surpasses the elastic limit of the copper, yet our structure is precisely machined, and we want to ensure that the geometry stays the same. Therefore we retook the CMM measurements after these operations and compared the results to those before.

### 5.3.1. Comparison of Old and New CMM Measurements

After a couple of months, the RFQ was disassembled for a minor alteration. During this time, we requested another CMM measurement to see if any changes occurred with the operations performed. Comparison of the old and new CMM measurements performed with the same python script and errors computed.

After we compared the four vanes to old and new data, we arrived at the Figure 5.17. In these difference plots, one may see some sudden jumps (10s microns at a time); we believe these jumps are associated with small dust particles or small scratches. In the top and bottom parts, these differences move around 0 microns which signals a nice stability; however, in the bottom vane, we see some periodic difference emerges around  $z = 0.2$  meters (Figure 5.18). We discussed this with the firm, and we will request more data in the next disassembly to understand if there is a small bending in that location. On the right and left vanes, we see small bending-like behavior. These parts are smaller than the top and bottom parts, therefore, less rigid. The current situation is not worrisome, but we requested more caution with these parts.

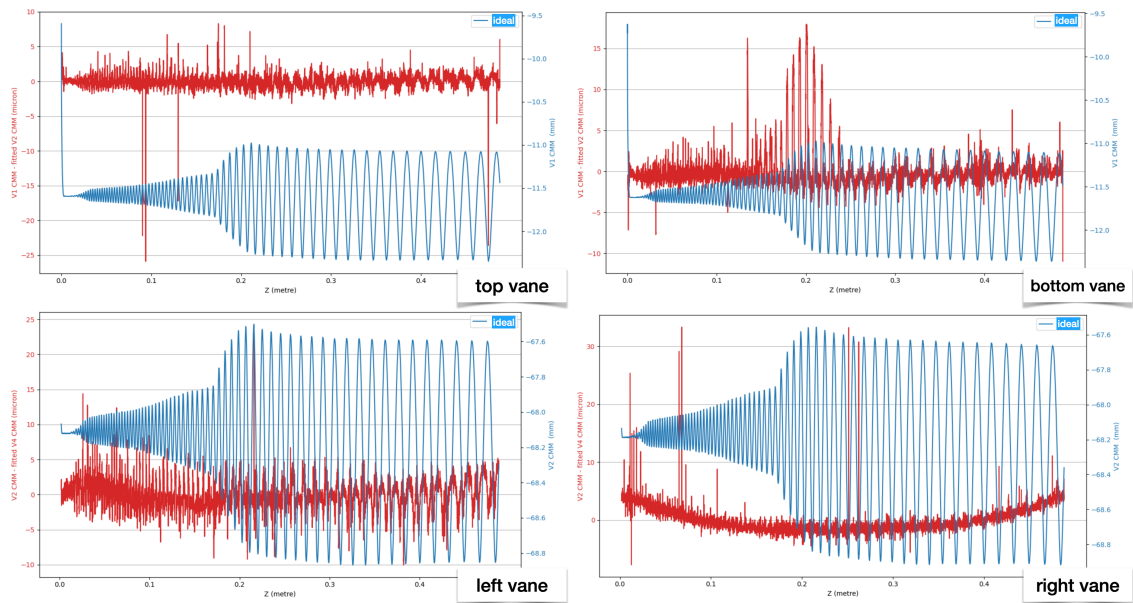


Figure 5.17. In blue, ideal vane geometry is represented, and in red, the difference between old and new CMM measurements is displayed. Notice the plot labeled bottom vane has some large periodic differences around 0.2 meters

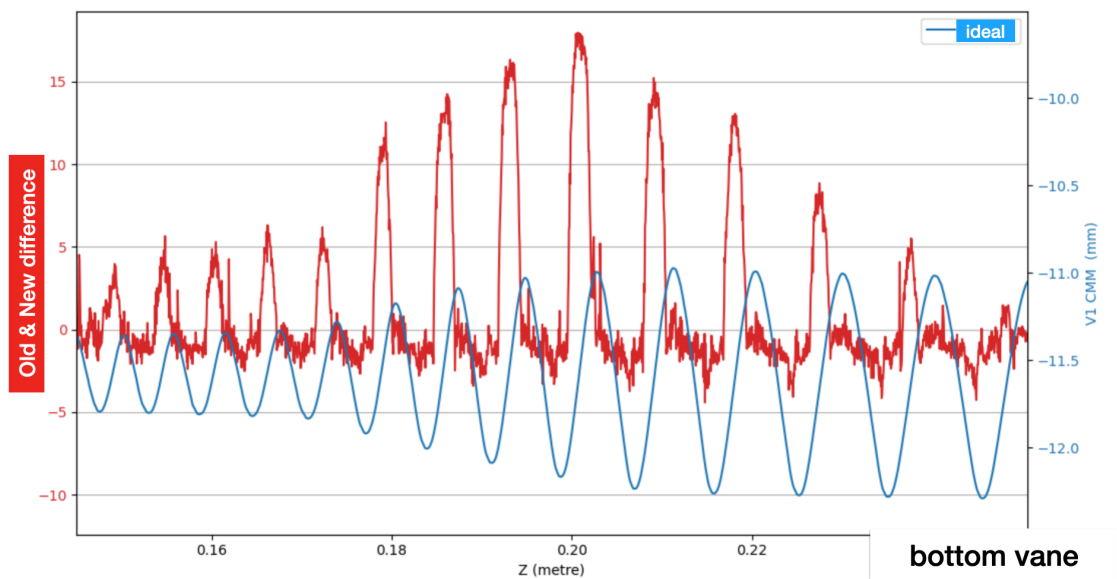


Figure 5.18. Bottom vane plot zoomed around 0.2 meters.

The overall situation shows that we can assemble, disassemble, make mechanical corrections, and produce a vacuum vane without seriously distorting the critical vane geometry.

We wanted to quantify the bowing effects in each vane. To achieve this, we separated high-frequency content and low-frequency content for all vanes. The separation value is decided after careful inspection of the Fourier transform of the errors. We present the results of this separation in Figure 5.19. In the error histograms, we can observe the contribution of these bowing effects to the overall errors. To quantify this, we calculated the ratio of the number of errors that fall within the  $\pm 10$  micrometer range to all errors, which is shown in Table 5.1. Speculating that these bowing effects will be eliminated with proper machining and handling procedures, we are hoping for better results in the future.

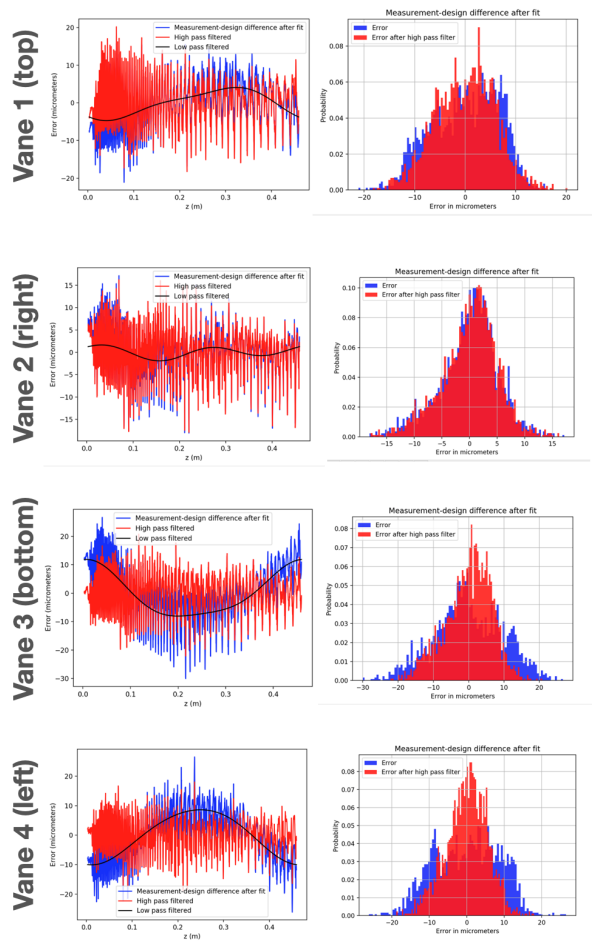


Figure 5.19. On the left column, errors are presented with blue, high-pass filtered errors with red, and low-pass filtered values represented with black for each vane. On the right column, error and high-pass filtered error values are histogrammed for each vane.

Table 5.1. The ratio of errors with an absolute value less than 10 micrometers to all is tabulated for unfiltered errors, and the errors after the high pass filter is applied.

	$P( Error  < 10\mu m)$	$P( Error  < 10\mu m)$ after High Pass filter
Vane 1	0.884	0.912
Vane 2	0.934	0.941
Vane 3	0.686	0.872
Vane 4	0.722	0.930

### 5.3.2. Laser Scanner Measurements and Their Comparison to CMM Method

If we need to disassemble the finalized RFQ in the future, we won't have CMM at our disposal in our lab. For this reason, we are studying other methods of coordinate measurements.

We rented a laser 3D scanning service (Figure 5.20), and the operator took 3D point cloud measurements on module-0 parts. This method promised 7 micrometers of resolution in the calibration measurements.

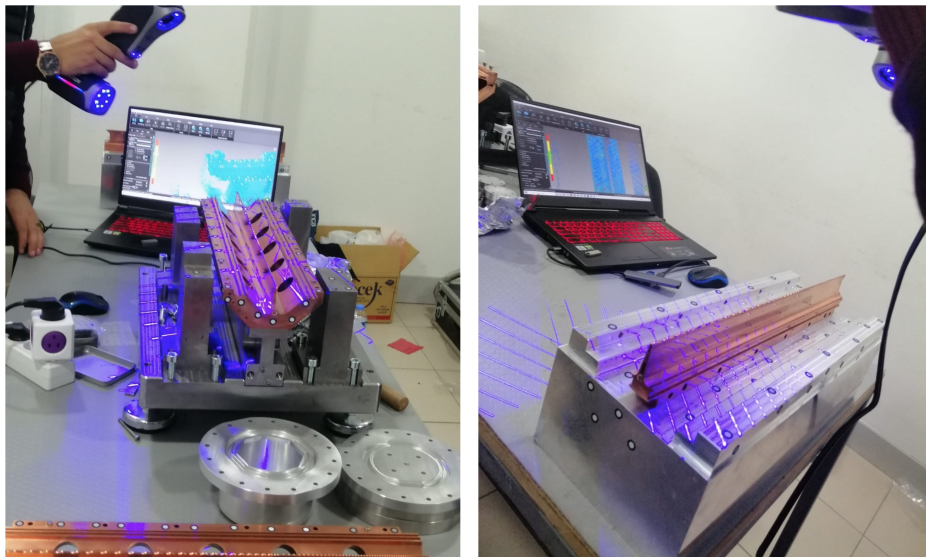


Figure 5.20. 3D laser scan process.

Since the success is critically dependent on vane tip geometry, we wanted to compare the results from CMM to laser scan values. CMM measurements are taken on a line on the vane tip, but the laser scan measures the whole geometry of the parts. To get a good measurement, first, we need to fit part measurement to part design. We used the open-source software Cloud Compare, and this software can fit two surfaces together and represent the difference in the geometry with a color scale. For the initial fit, we used the full design and full measurement data (Figure 5.21), then we isolated vane on both geometries and re-apply the fit. After shrinking the isolation region a few more times on the vane tip and refitting, we achieved a point cloud that corresponds to CMM measurement (Figure 5.22). Then we exported these into a text file and used a modified version of the python script we used in the previous section. We showed that the resolution of this method in the critical region is larger than 100 microns which makes the device unusable for our purpose (Figure 5.23).

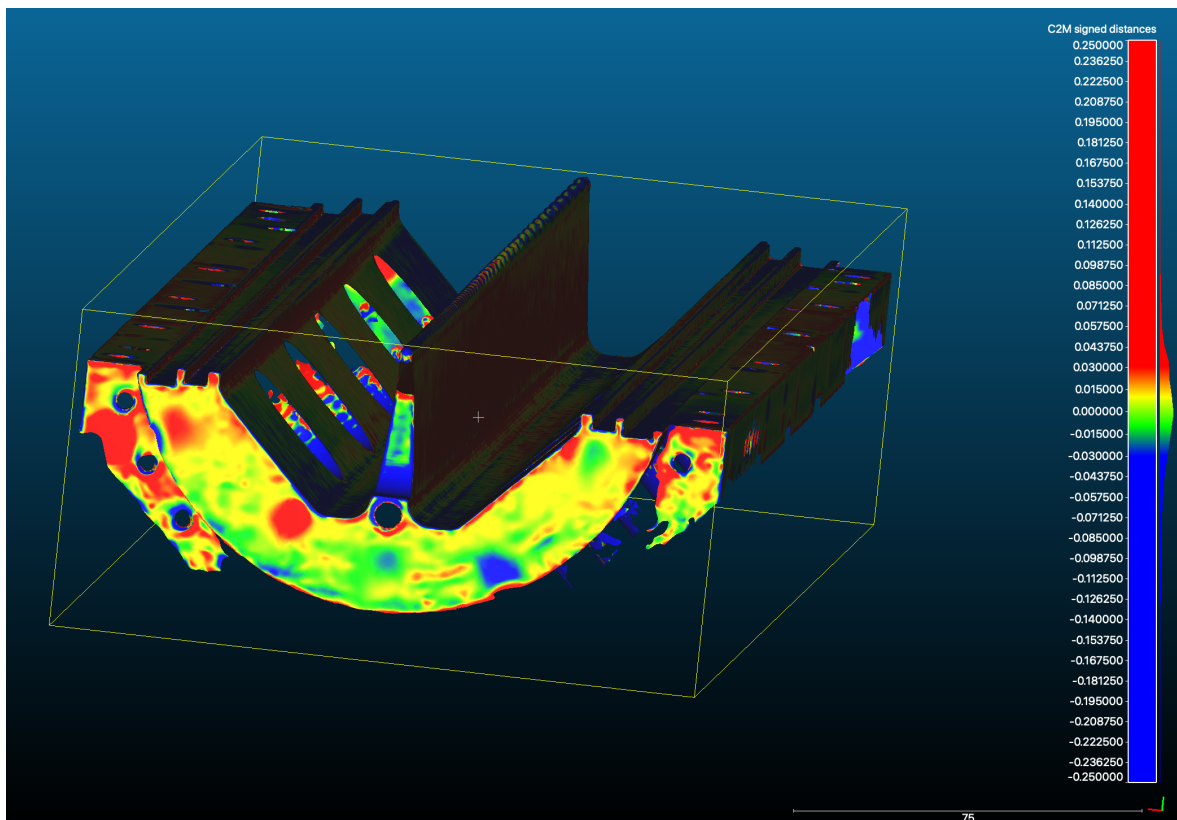


Figure 5.21. Cloud Compare software result on full part geometry. Colors represent the distance to the design surface.

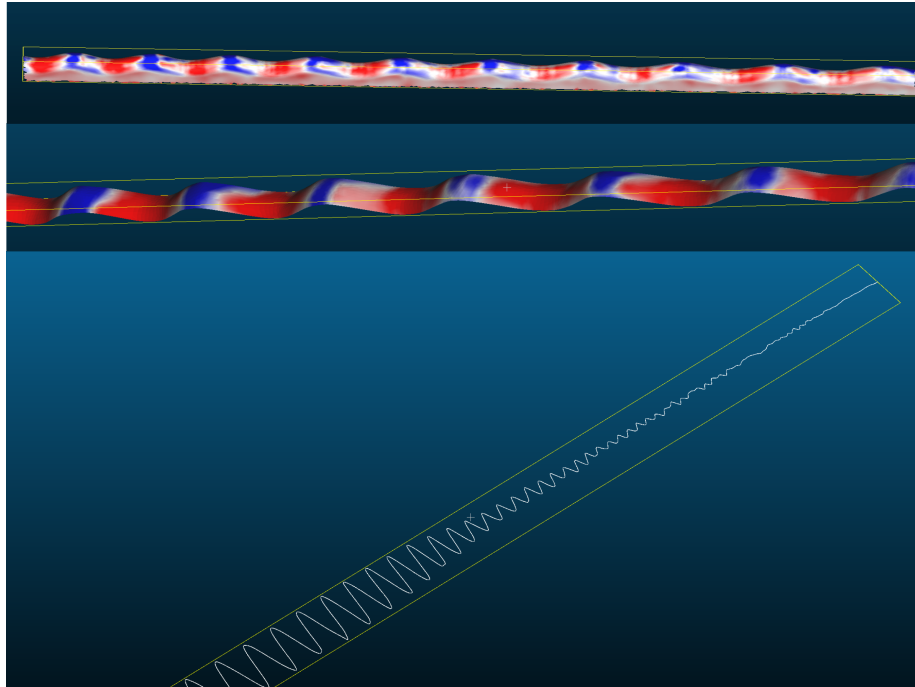


Figure 5.22. The successive selection of surfaces used in the fit procedure is presented. In the top two plots, blue areas indicate that the measurement result falls within the reference geometry, and red areas indicate that the result falls outside the reference geometry. In the final stage, the data points selected for further error analysis are shown in the bottom figure.

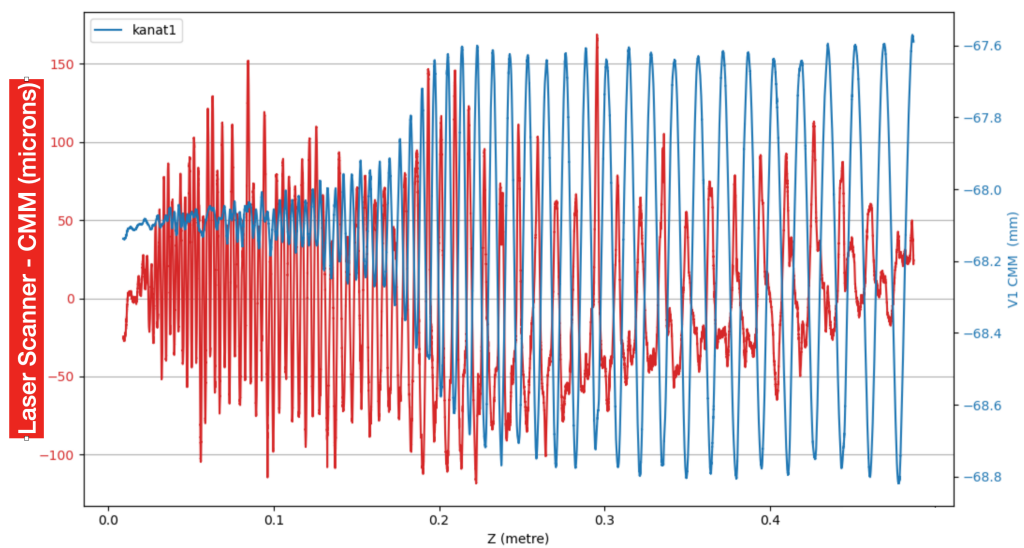


Figure 5.23. Difference of Laser scan with CMM measurements shows that the resolution of the Laser scan is worse than 100 microns.

## 5.4. Visual Inspection of The Machined Parts

We wanted to see the vane tip surfaces, and if possible, we would like to position measurements. Since the CMM measurement time at our disposal is limited and we can measure a limited number of points, we can't understand the small features engraved on the surface in the machining process. Also, we would like to make investigations at our lab that may prove very beneficial.

### 5.4.1. Initial Tests on an Advanced Microscope with Precise Motorized Stage

One method of inspection can be devised using a microscope objective with a shallow depth of focus. In this way, we can perform focus stacking, and using height information, we can even produce 3D images of the sample. We tested this method using a microscope with a large motorized stage (Figure 5.24).<sup>1</sup>

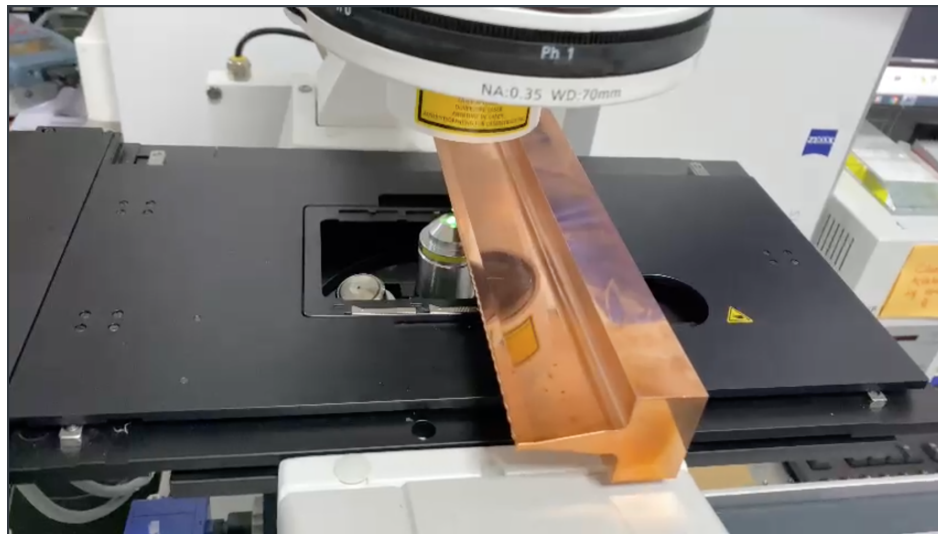


Figure 5.24. Sample part placed on a motorized microscope stage.

Initially, we explored two microscopy options, reflection microscopy, and transmission microscopy. We have presented the resulting images in Figure 5.25. However,

---

<sup>1</sup>We thank Professor Mehmet Burçin Ünlü for letting our sample be imaged in his lab.

the transmission image only shows the very end of the vane tip, and any other information is lost. Therefore, we moved forward with reflection microscopy and took multiple images of the same frame while changing the height of the stage. In Figure 5.26, we have shown an image focused on a specific part of the tip. As the stage moves, different parts of the sample come into focus, as illustrated in Figure 5.27. In both figures, a small section of pixels and their corresponding grey values are graphed. We observed that sharp changes only occur in the regions that are in focus.

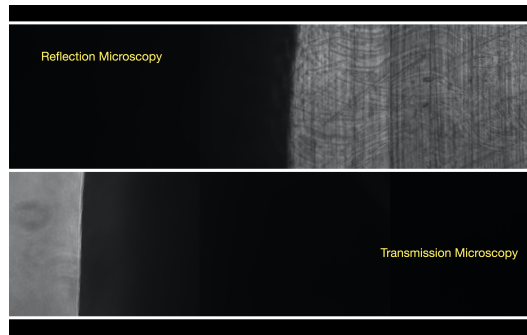


Figure 5.25. Reflection and transmission microscopy images. In the reflection mode, the best images are obtained when the surface in the focused plane is parallel to it. Transmission mode excels at the very tip, yet there is no other useful information can be received.

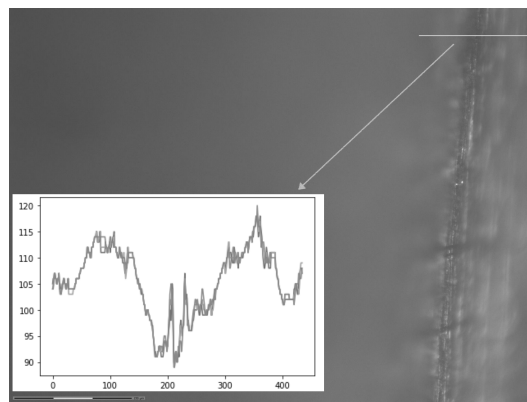


Figure 5.26. One example image is when the focus plane lowered to the tip region. As one might observe, only a small part of the surface is in focus, and the rest of the image is not sharp at all. In the bottom left, grey values from a row of pixels (marked with a white line) are graphed.

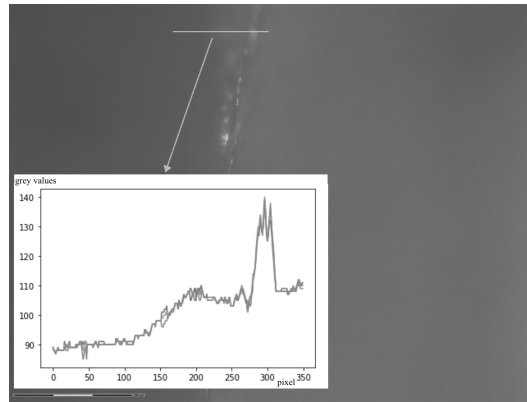


Figure 5.27. The difference in the stage height is 0.550 mm compared to the image presented in figure 5.26.

We developed a python script to process all the image files and identify in-focus pixels based on a certain difference between the 5th pixel on the left and right. The resulting in-focus pixels from all images were combined into a single image, as shown in Figure 5.28. By using the stage height information, we were able to create a 3D image from these in-focus pixels. To remove most of the noise, which was mostly in the form of isolated pixels, we applied an erosion algorithm. The resulting cleaned 3D image is shown in Figure 5.29.

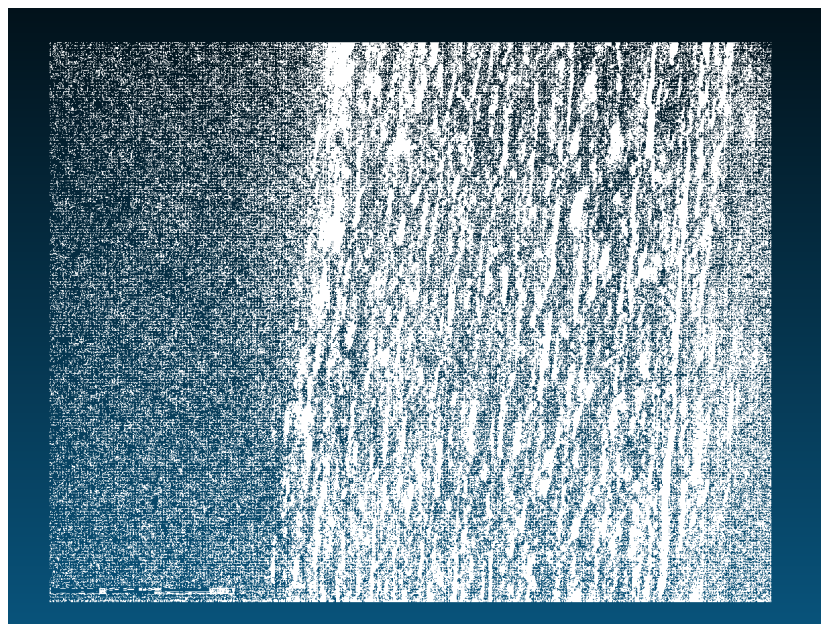


Figure 5.28. Points that are selected from each image stacked together.

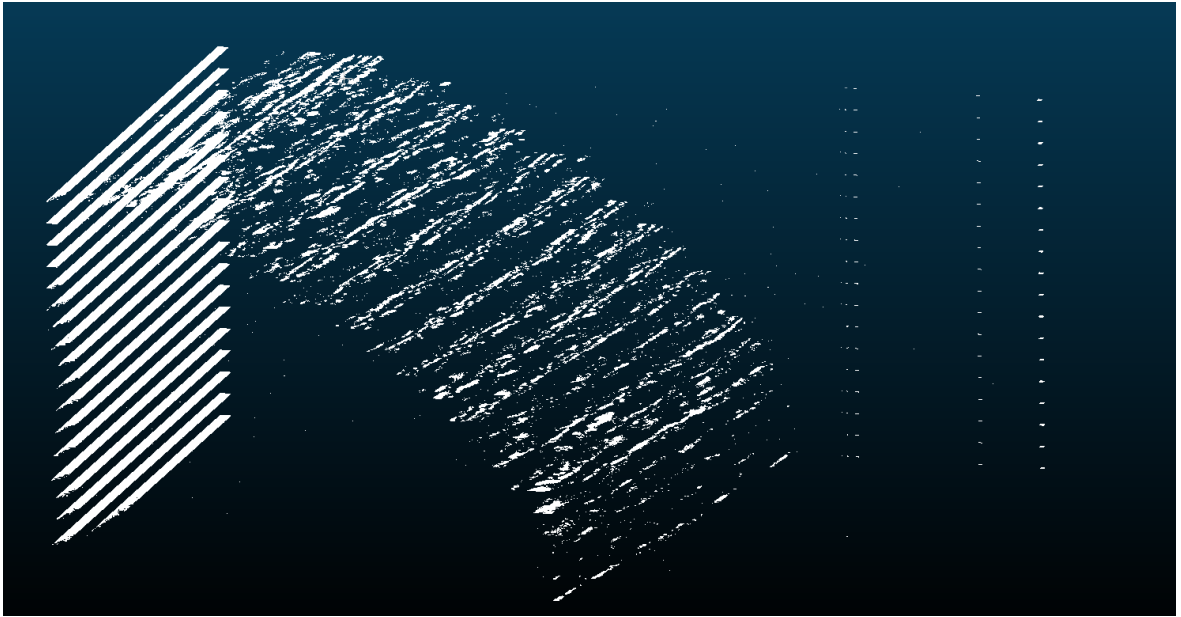


Figure 5.29. The 3D image in the Figure 5.28 when the underlying images cleaned with erosion method.

Our sample has odd dimensions, and because of that, the only configuration we could image the vane tips with this microscope could not illuminate the vane tip well. Even if this was the case, we were able to get some stacked images and 3D results with a very basic analysis. This encouraged us to make some feasibility studies with optical systems we can construct.

#### 5.4.2. Tests with Stereo Microscope

We used an Olympus SX30 stereo microscope with a long working distance of approximately 8cm and up to 4x zoom in the objective part. To explore the possibility of measuring focus using a laser and image analysis, we removed one ocular and replaced it with a bare sensor from an old webcam (Figure 5.30). We left the second ocular in place and directed a laser beam through it. We captured images of a vane tip with both the stereo microscopes ring light on and off (Figure 5.31 and 5.32). While this setup is suitable for inspection, it is not precise enough for coordinate measurement. The images of the vane tips showed small markings that resemble pits, likely caused by the spherical mill cutter attempting to cut the design curvatures. These structures

were not previously measured for surface roughness, but we plan to do so as they may increase the potential for electric discharge.

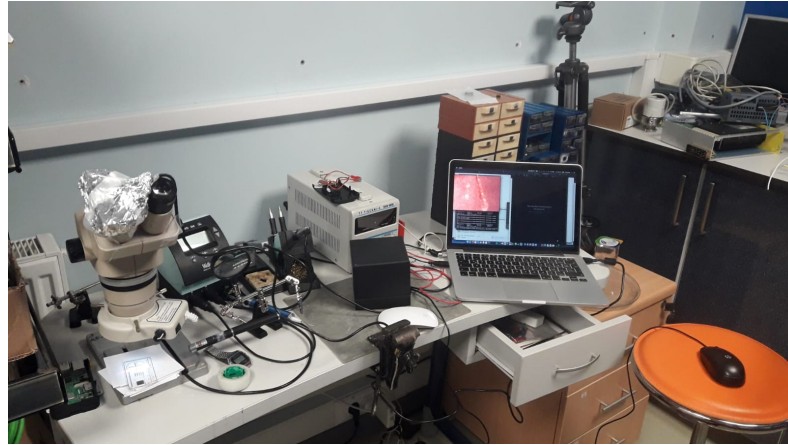


Figure 5.30. Stereo microscope setup: Left ocular of the Olympus SX30 microscope was removed, and the PS3 webcam sensor (optics are removed ) was placed in its place (wrapped in aluminum foil so that we can protect the sensor from stray light). Images acquired via a script. A laser pointer is aligned on the left ocular so that focused laser light can be seen in the image (not shown here).

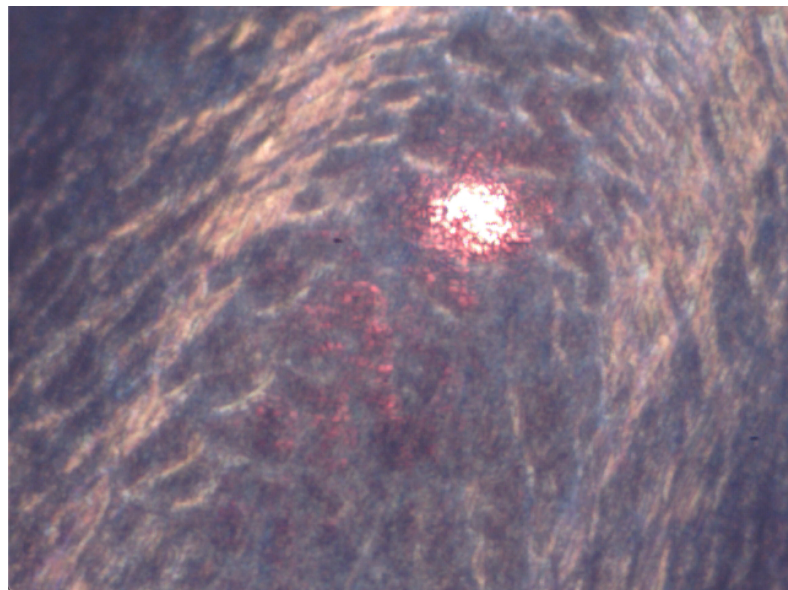


Figure 5.31. Image acquired in 4x mode of the microscope. Laser light and the machining marks on the vane tip can be observed. We tested if we could use a laser to assess whether the region of interest was in focus quickly.

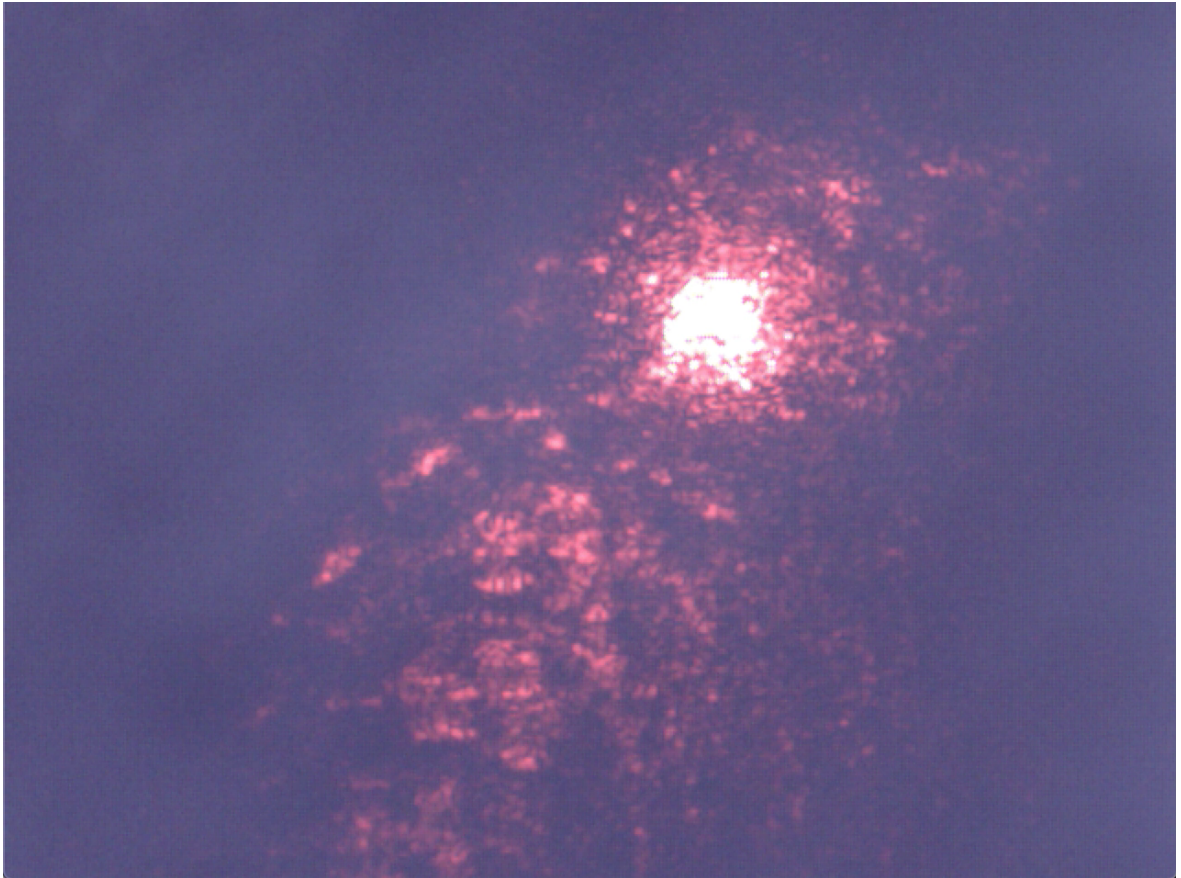


Figure 5.32. Same image as Figure 5.31 but the white light source is turned off.

#### 5.4.3. Tests with a DIY Microscope

We created a camera adapter for a microscope objective using empty lens extensions and a 3D-printed part. We then attached an old, used 40x lens to this adapter and used it to capture images with a very shallow depth of focus. Since the working distance of this lens is less than 1 mm, we positioned the sample almost horizontally to the sample surface during imaging. However, the advantage of this setup is that the depth of focus is very shallow, less than 10  $\mu\text{m}$ . Using this setup, we were able to capture detailed surface features of the vane tip, as shown in Figures 5.38, 5.36 and 5.37, as well as the flat region, as shown in Figure 5.35. These images confirmed that there is more surface roughness on the vane tips than on the flat regions, which were previously measured.



Figure 5.33. DIY camera adaptor for microscope objective.

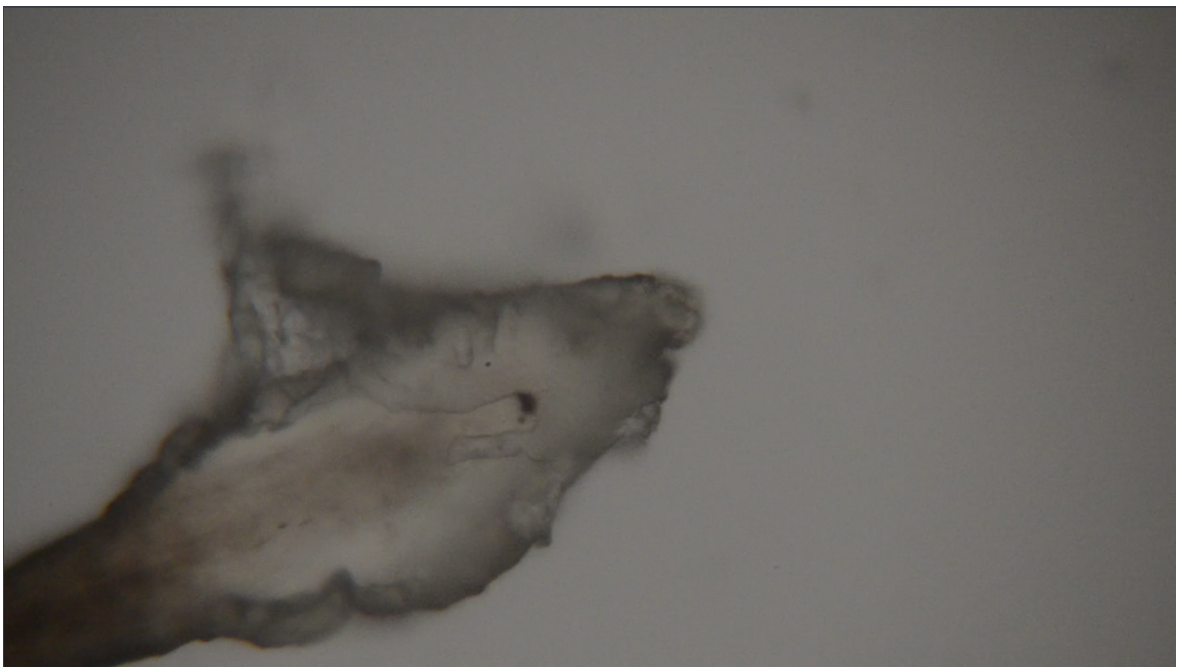


Figure 5.34. A human hair image taken with the DIY microscope.

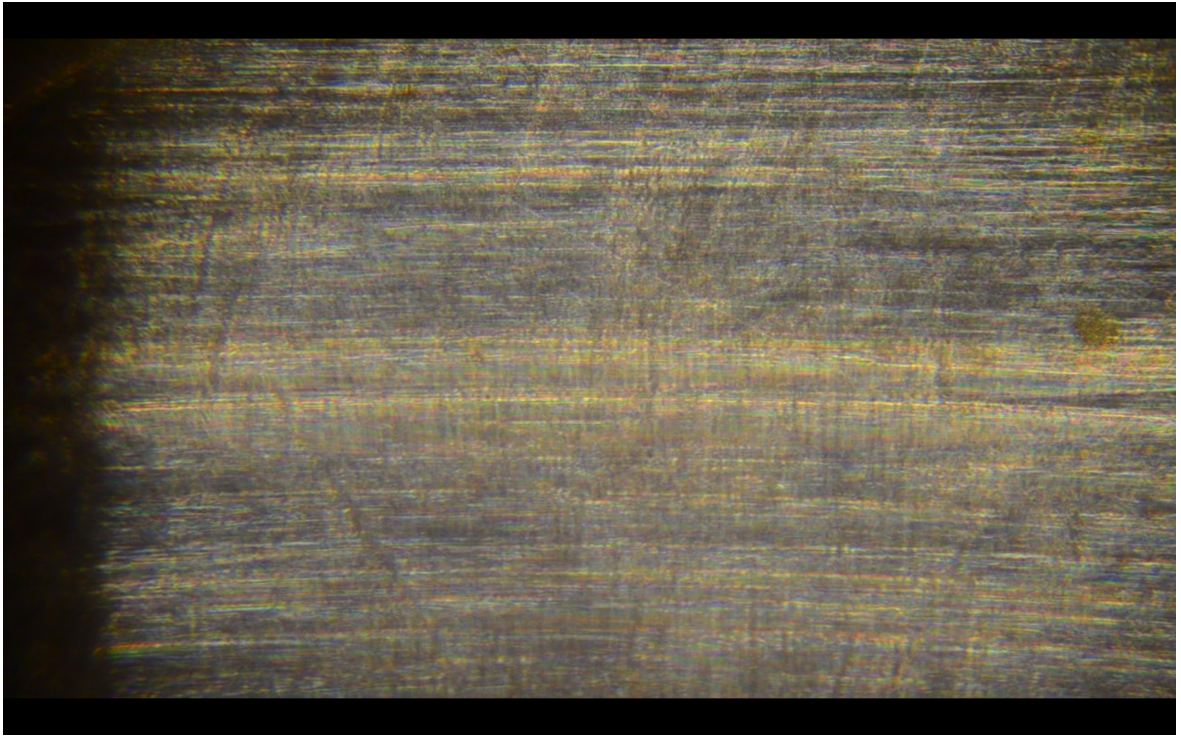


Figure 5.35. An image of a straight region on the part. The image shows that straight parts are manufactured with very little surface irregularities compared to vane tips

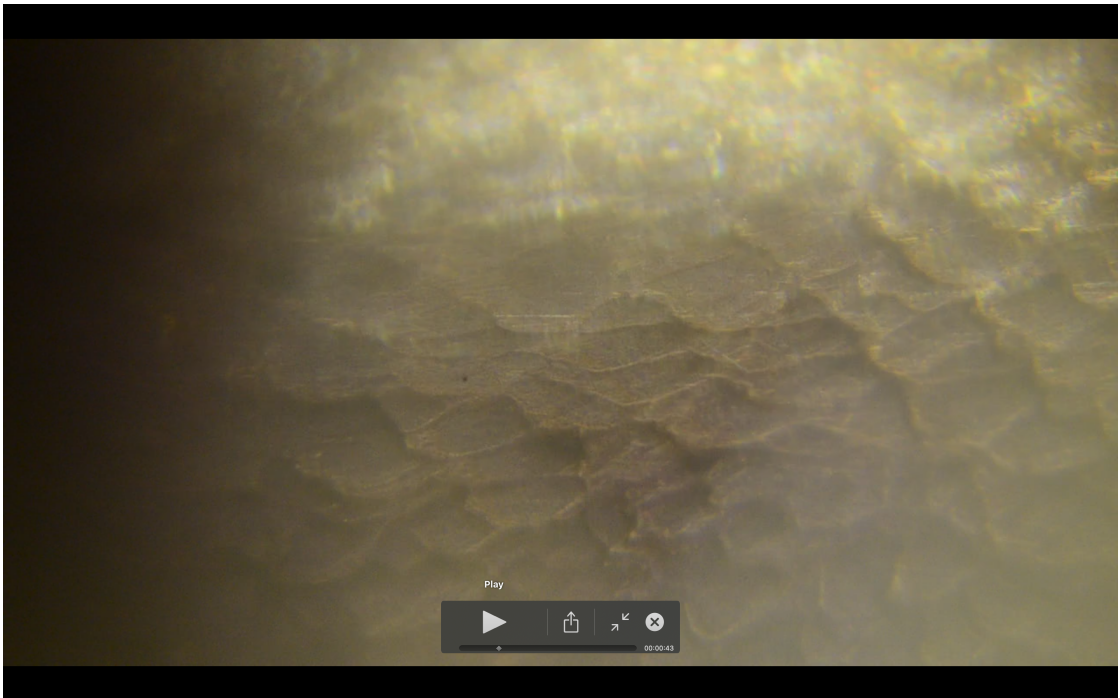


Figure 5.36. An image from the vane tip where the center of the image is sharply focused.

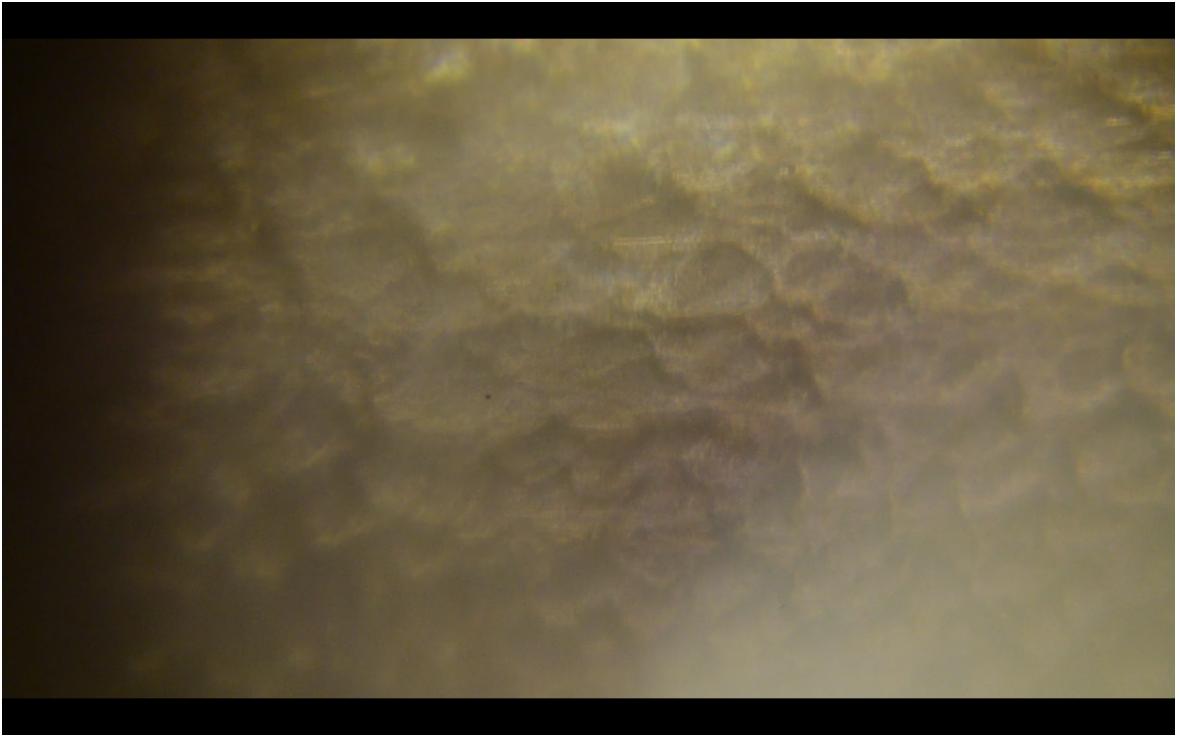


Figure 5.37. An image from the vane tip where the center of the image is not properly focused.



Figure 5.38. An image from the vane tip where the right top of the image is in focus.

A shallow depth of focus brings a short working distance as well. With this setup, our working distance is around 0.20 mm. This working distance and geometry of the objective might prohibit imaging some parts of the vane tips.

We propose constructing an image transfer tube, as described in [38], to enable us to image the entire surface of the vane tips. This setup can also be used as a touchless probe for the XYZ translation table of KahveLAB's milling machine. Based on our initial findings, we are confident that we can construct such a system to measure vane coordinates and inspect vane tip surfaces.

## 6. 800 MHZ RFQ DESIGN ERROR STUDIES AND EFFECT OF CAVITY SURFACE ROUGHNESS ON CAVITY MODES

### 6.1. Error Studies

To investigate the impact of frequency, vane voltage, and input beam energy changes, we utilized two computer codes: PARMTEQM and Toutatis. First, we used PARMTEQM, and then we employed our script to run Toutatis. However, we encountered an issue with Toutatis where it did not use the  $\phi_{sync}$  value listed in a file; instead, it calculated this value from other values (as shown in Figure 6.1). This inconsistency led to a difference in the accepted particles, and we hypothesized that particles outside of the  $\pm 100$  degree phase were lost. After a small study, we chose this phase range to limit the Toutatis input beam phase. With this change, we scaled the Toutatis results for comparison with PARMTEQM.

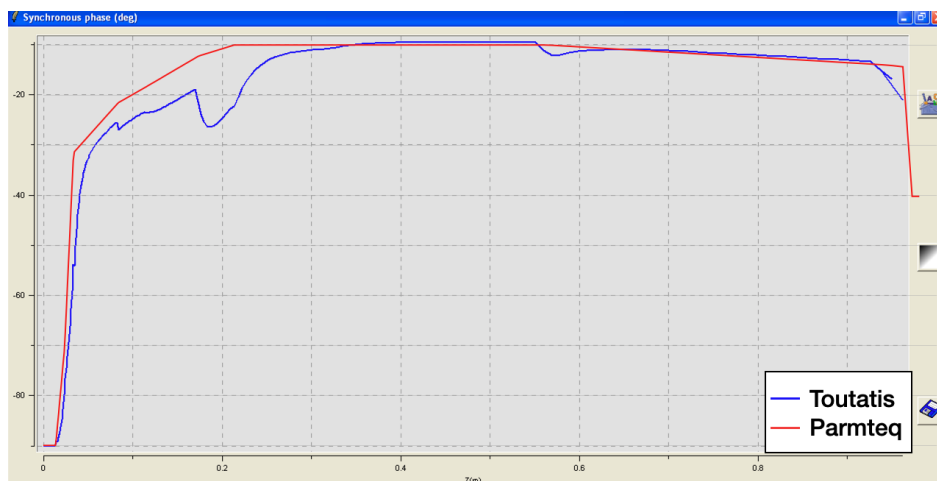


Figure 6.1. Toutatis calculation of the PTAK RFQ sync-phase value with respect to  $z$  presented with the blue line. The PARMTEQM results are presented with the red line. We suspect that the discrepancy between PARMTEQM and Toutatis sync-phase calculation makes Toutatis lose track of accelerated particles.

### 6.1.1. Vane Voltage, Frequency, and Input Beam Energy

PARMTEQM offers a few error study options, whereas another code called Toutatis can simulate errors in machining also. The reader can find the comparison of two codes in these error study results in Figure 6.2. Some data points are missing for Toutatis. When the accelerated particles are small in number, Toutatis prefers to track abundant unaccelerated particles. This effect might also be coupled with the discrepancy in  $\phi_{sync}$  values. All in all, we excluded data points if this was the case and refrained from further speculation since we don't have access to the source code for either computer code.

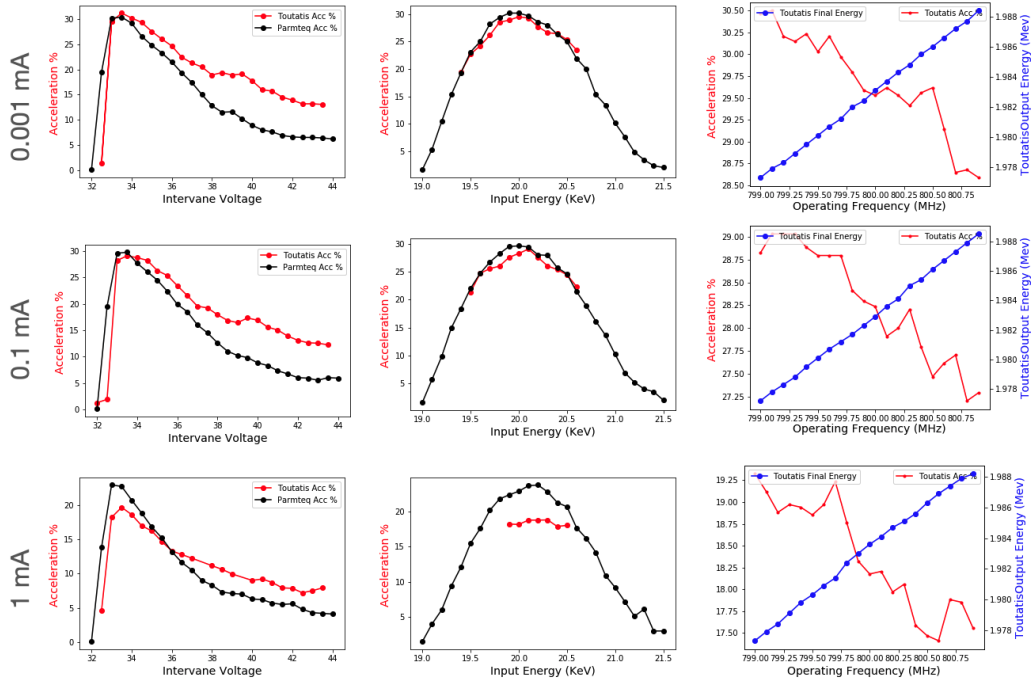


Figure 6.2. On the left column, acceleration percent versus inter-vane voltage is presented. In the middle column, acceleration percent versus input beam energy is presented. In the right column, acceleration percent versus operating frequency and output beam energy versus operating frequency are shown together.

These error studies showed the operation regime of the PTAK RFQ. For example, the design can't tolerate a decrease in inter-vane voltage; as a result, we must deliver

RF power at least equal to the design value. Also, we looked at the effect of the input current. Up to 0.1 mA, acceleration percent stays the same as shown in Figure 6.3. The maximum possible output current value is 0.4 mA for a 4 mA input current shown in Figure 6.3.

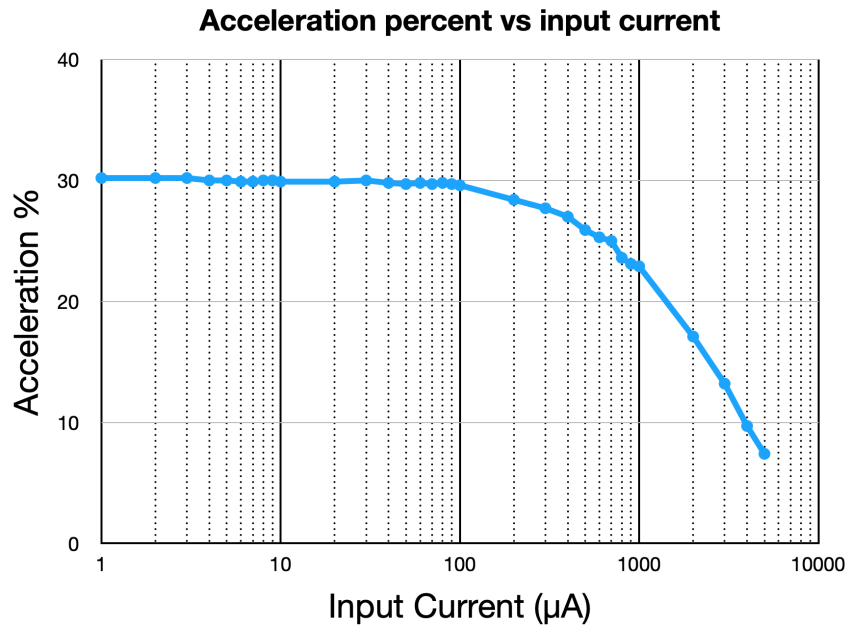


Figure 6.3. Acceleration percent vs. input current

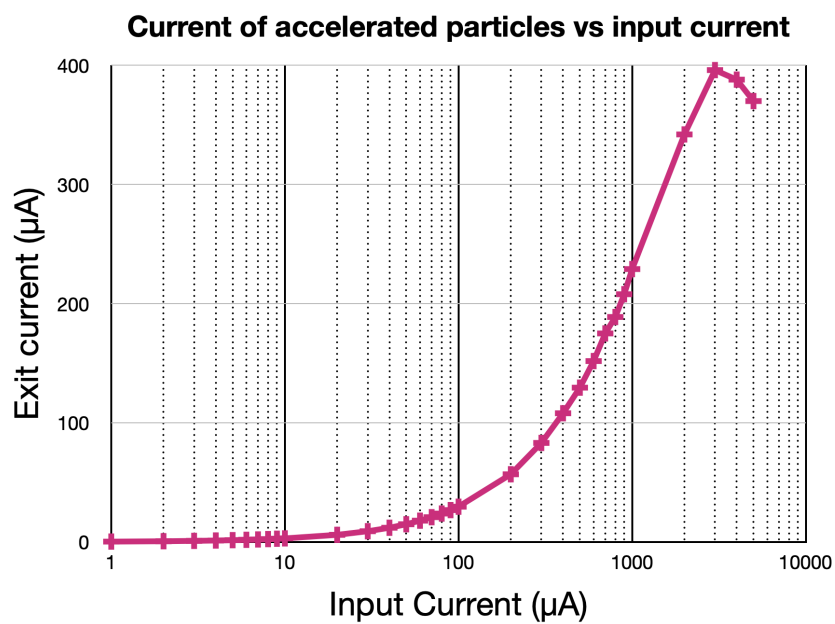


Figure 6.4. Current of accelerated particles vs. input current

Table 6.1. Comparison of Toutatis simulation results in Ideal geometry vs. machining errors present in the first half of ideal geometry. In this table, results presented without scaling

Geometry Description	Acceleration %	Acceleration Energy (MeV)
0 - 100 cm: Ideal (PARMTEQM)	50.70	1.9828
0 - 50 cm: CMM 50-100 cm: Ideal (PARMTEQM)	49.74	1.9856

### 6.1.2. Beam Dynamics Simulation with Machining Errors

In our initial attempt, we tried to import cell design values ( $a$ ,  $m$ ,  $l$ ,  $\rho$ ) from PARMTEQM to Toutatis, and we used the geometry produced by Toutatis. However, we were not successful, possibly because the  $z$  positions were not compatible between the two simulation and design codes. Later on, we used an interpolation and fit method to fit the PARMTEQM vanes onto the Toutatis vanes, and then we used only the  $z$  shift (disregarding the  $r$  shift) to evaluate the  $r$  values at the  $z$  positions on the Toutatis file. This approach was successful, and we obtained promising results. We then added machining errors to the simulation.

Since we only had the first half of the RFQ remaining for the full design test, we took the remaining 0.5 meters directly from the PARMTEQM results. The results of this simulation can be seen in Table 6.1. We also added machining errors to the simulation. Despite these errors, the impact on the beam was minimal, giving us confidence that the machining method used in the test production would yield acceptable results in the actual RFQ as well.

## 6.2. Surface Roughness

We also investigated the effects of the cavity's surface roughness on the resonant frequency and the quality factor of the cavity [39]. The study results are shown in Figures 6.5 and 6.6. The results indicated that we do not need to be concerned even

in the case of extreme surface roughness, up to 30 micrometers. However, it is worth noting that the actual measured surface roughness value was around 0.2 micrometers, which is significantly lower than in this extreme case.

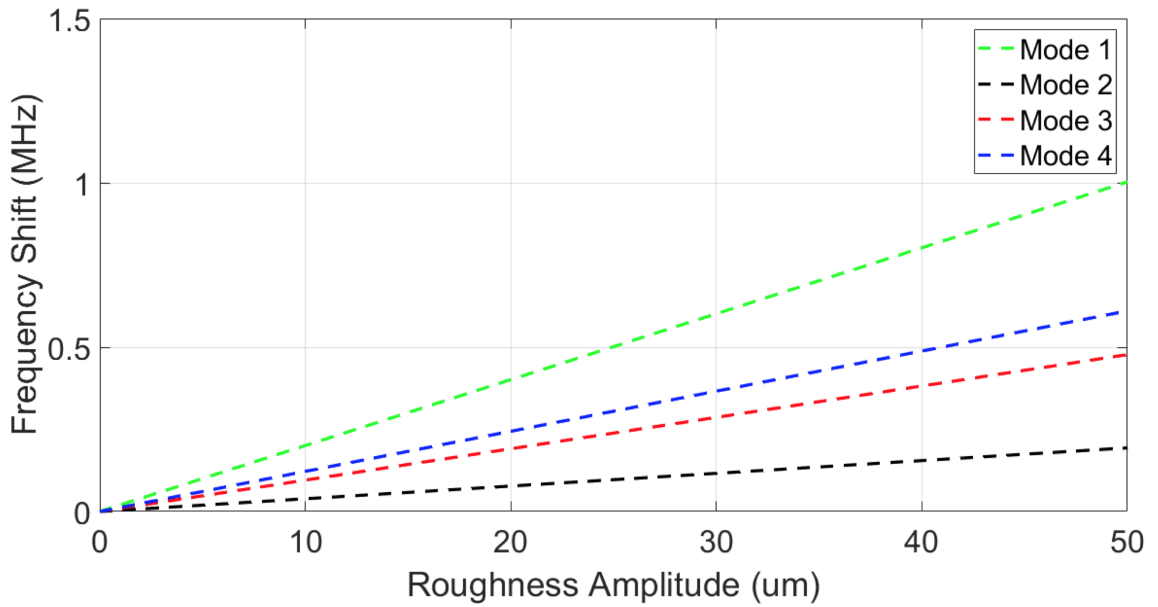


Figure 6.5. Frequency shift of fundamental modes induced by surface roughness.

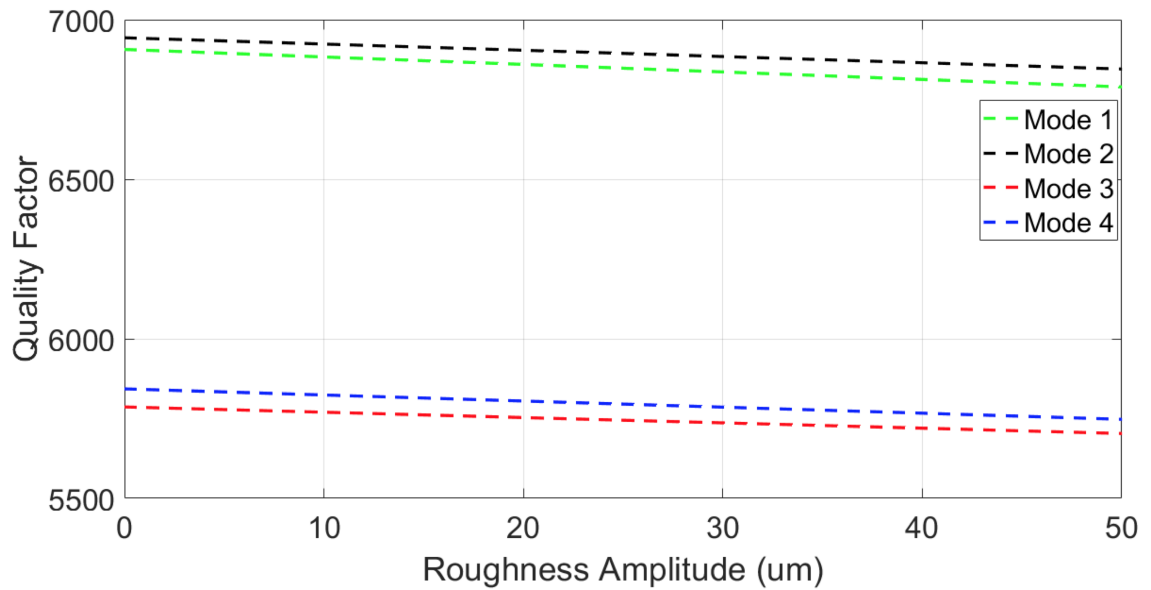


Figure 6.6. Quality factor change of fundamental modes induced by surface roughness.

### 6.3. Progress on Module-1 and Module-2

Currently, the actual RFQ modules (module-1 and module-2) are in production. In their production, oxygen-free copper (OFC) is used. Two changes were made to the machining procedure to mitigate the problems we saw in module zero. Firstly the wait time between machining passes increased by a couple of days. Secondly, the technicians machine an aluminum dummy with the proposed tool path before machining OFC parts and then measuring them. This is done to observe if the CNC milling induced deflection on the softer material. A recent picture displaying the current state of the parts is given in Figure 6.7.

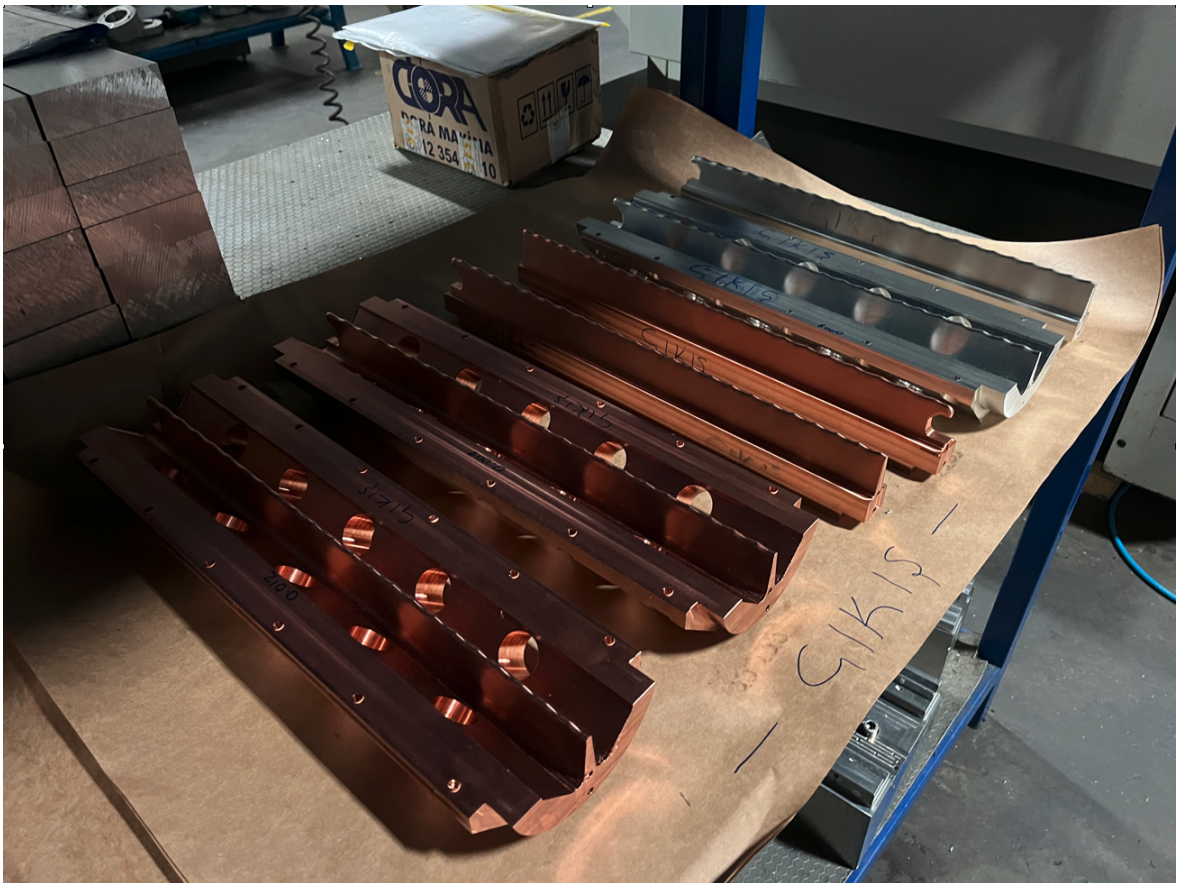


Figure 6.7. In this picture, both OFC parts and aluminum dummies are presented in their current state.

## 7. CONCLUSION

In this work, we have presented a comprehensive discussion on the RFQ design software DemirciPro and the RFQ section of PTAK (Proton Testbeam At Kandilli). We have demonstrated the development of 8TP calculation based on FEM in DemirciPro and compared the resulting data with those available in the literature. Additionally, we have implemented a beam dynamics simulation based on the leap-frog method and discussed the current status of the code with its capabilities. Furthermore, we have provided a roadmap for advancing DemirciPro's capabilities to exceed those of its competitors.

Regarding PTAK, we have presented a novel design approach and discussed our design choices and limitations. We have conducted beam dynamics simulations, completed a test production, and measured the vanes. The initial RF and vacuum tests have shown promising results. We have summarized the current state of the output of actual modules and proposed a cost-effective method for simple optical coordinate measurement using the available XYZ table of our milling machine. Further bead-pull measurements, vacuum tests, and CMM measurements will be repeated once the modules are completed. Our study has enabled us to improve the mechanical design for better alignment and take measures to reduce bowing-like errors. We expect to deliver PTAK's first 2 MeV proton beam by the end of 2023, depending on the progress of the RF power supply study.

Overall, we believe that our study will contribute to the advancement of the field of RFQ design and enable us to make significant progress toward the completion of PTAK's proton beam.

## REFERENCES

1. Stokes, R. H. and T. P. Wangler, "Radiofrequency Quadrupole Accelerators and Their Applications", *Annual Review of Nuclear and Particle Science*, Vol. 38, No. 1, pp. 97–118, 1988.
2. Paul, W. and H. Steinwedel, "A New Mass Spectrometer Without a Magnetic Field", *Zeitschrift fuer Naturforschung A*, Vol. 8, No. 7, pp. 448–450, 1953.
3. Kapchinskii, I. M. and V. A. Teplyakov, "A Linear Ion Accelerator with Spatially Uniform Hard Focusing", *Pribory i Tekhnika Eksperimenta*, Vol. 13, No. 2, pp. 19–22, 1970.
4. Kapchinskii, I. M. and V. A. Teplyakov, "Possibility of Reducing the Injection Energy and Increasing the Limit Current in an Ion Linear Accelerator", *Pribory i Tekhnika Eksperimenta*, Vol. 13, No. 4, pp. 17–18, 1970.
5. Golosai, N. I., G. N. Dernovoi, S. A. Il'evskii, V. V. Klokov, N. N. Kutorga, I. G. Mal'tsev, A. P. Mal'tsev, V. S. Sevost'yanov, V. B. Stepanov, V. A. Teplyakov and I. M. Shalashov, "Tests on the Initial Section of an Accelerator with Quadrupole HF Focusing", *Soviet Atomic Energy*, Vol. 39, No. 2, pp. 716–719, 1975.
6. Crandall, K., R. Stokes and T. Wangler, "RF Quadrupole Beam Dynamics Design Studies", *Linear Accelerator Conference, BNL*, Vol. 51134, New York, United States, p. 205, 1979.
7. Stokes, R. H., K. R. Crandall, R. W. Hamm, F. J. Humphry, R. A. Jameson, E. A. Knapp, J. M. Potter, G. W. Rodenz, J. E. Stovall, D. A. Swenson and T. P. Wangler, "The Radio-Frequency Quadrupole: General Properties and Specific Applications", *11th International Conference on High-Energy Accelerators*, Geneva, Switzerland, pp. 399–406, 1980.

8. Alessi, J., “RFQ Preinjectors”, *Nuclear Instruments and Methods in Physics Research Section B: Beam Interactions with Materials and Atoms*, Vol. 40, pp. 954–958, 1989.
9. Schempp, A., “Radio-Frequency Quadrupoles (RFQ)”, *CAS - CERN Accelerator School : RF Engineering for Particle Accelerators*, Vol. 1, Oxford, United Kingdom, pp. 522–537, 1992.
10. O’Shea, P. G., T. A. Butler, M. T. Lynch, K. F. McKenna, M. B. Pongratz and T. J. Zaugg, “A Linear Acceleration in Space—The Beam Experiment Aboard Rocket”, *Linear Accelerator Conference*, New Mexico, United States, pp. 739–742, 1990.
11. Türemen, G., B. Yasatekin, Ö. Apsimon, M. Celik, Z. Sali, Y. Akgun, A. Alacakir, S. Bolukdemir, E. Durukan, H. Karadeniz, E. Recepoglu, E. Cavlan, G. Unel and S. Erhan, “Project PROMETHEUS: Design and Construction of a Radio Frequency Quadrupole at TAEK”, *2nd International Beam Instrumentation Conference*, Oxford, United Kingdom, pp. 652–655, 2013.
12. Adıgüzel, A., S. Açiksöz, A. Çağlar, H. Çetinkaya, Ş. Esen, D. Halis, A. Hampar-sunoğlu, T. İlhan, A. Kılıçgedik, O. Koçer, , S. Oğur, S. Öz, A. Özbey, V. E. Özcan and N. G. Ünel, “Ion Source and LEBT of KAHVELab Proton Beamline”, *arXiv* 2208.00529, 2022.
13. “RFQ Design Codes”, Los Alamos National Laboratory, LA-UR-96-1836, 2005.
14. Staples, J. W., “RFQs—An Introduction”, *AIP Conference Proceedings*, Vol. 249, No. 2, pp. 1483–1532, 1992.
15. Wangler, T. P., *RF Linear Accelerators*, John Wiley & Sons, New York, 1998.
16. Crandall, K., “RFQ Radial Matching Sections and Fringe Fields”, *Linear Accelerator Conference*, Seeheim, Germany, pp. 119–121, 1984.

17. Hughes, T. J. R., *The Finite Element Method: Linear Static and Dynamic Finite Element Analysis*, Dover Publications Inc., New York, 2000.
18. Duperrier, R., R. Ferdinand, J.-M. Lagniel and N. Pichoff, “Toutatis, the CEA-Saclay RFQ Code”, *XX International Linac Conference*, Monterey, California, pp. 839–841, 2000.
19. Diserens, N. J., “RFQCOEF, A Package For Extracting The Harmonic Coefficients for the Potential Function in an RF Quadrupole Cell”, *Linear Accelerator Conference*, Seeheim, Germany, pp. 324–326, 1984.
20. Polycarpou, A. C., *Introduction to the Finite Element Method in Electromagnetics*, Morgan & Claypool Publishers, California, 2006.
21. Brun, R. and F. Rademakers, “ROOT — An Object-Oriented Data Analysis Framework”, *Nuclear Instruments and Methods in Physics Research Section A: Accelerators, Spectrometers, Detectors and Associated Equipment*, Vol. 389, No. 1, pp. 81–86, 1997.
22. Cakir, O., E. Celebi, H. Cetinkaya, H. Kolenoglu, G. Turemen, Z. Uysal and G. Unel, “DemirciPro’s Tools for Completing the Linac: Ion Source and LEBT Line”, *arXiv* 2103.11829, 2021.
23. Möhl, D., “Sources of Emittance Growth”, *CAS - CERN Accelerator School: Intermediate Course on Accelerator Physics*, Zeuthen, Germany, pp. 245–269, 2003.
24. Kalvas, T., O. Tarvainen, T. Ropponen, O. Steczkiewicz, J. Ärje and H. Clark, “IBSIMU: A Three-Dimensional Simulation Software for Charged Particle Optics”, *Review of Scientific Instruments*, Vol. 81, No. 2, p. 02B703, 2010.
25. “TRAVEL v4. 07: User Manual”, CERN, Geneva, Switzerland, 2007.
26. “User’s Guide for the POISSON/SUPERFISH Group of Codes”, Los Alamos Na-

- tional Laboratory, Los Alamos, New Mexico, 1987.
27. Hestenes, M. R. and E. Stiefel, “Methods of Conjugate Gradients for Solving Linear Systems”, *Journal of Research of the National Bureau of Standards*, Vol. 49, No. 6, pp. 409–436, 1952.
  28. Dassault Systèmes, “CST Studio Suite 3D EM Simulation and Analysis Software”, 2023, <https://www.3ds.com/>, accessed on November 21, 2022.
  29. Catmull, E. and R. Rom, “A Class of Local Interpolating Splines”, *Computer Aided Geometric Design*, pp. 317–326, 1974.
  30. Açüksöz, S., A. Adıgüzel, H. Çetinkaya, Ş. Esen, D. Halis, A. Hamparsunoğlu, T. B. İlhan, A. Kılıçgedik, O. Koçer, S. Oğur, S. Öz, A. Özbey, V. E. Özcan and G. Ünel, “Beam Diagnostics at KAHVE Lab Proton Source and LEBT Line”, *Proceedings of Science*, Vol. EPS-HEP2021, p. 856, 2022.
  31. Maier Jr, L. C. and J. C. Slater, “Field Strength Measurements in Resonant Cavities”, *Journal of Applied Physics*, Vol. 23, No. 1, pp. 68–77, 1952.
  32. “Dora Makina”, <https://www.doramakina.com.tr/en/>.
  33. Bitter, R., T. Mohiuddin and M. Nawrocki, *LabVIEW: Advanced Programming Techniques*, CRC Press, New York, United States, 2006.
  34. Şeyma Esen, *Düşük Betalı Proton Hızlandırıcısı için Uzay Yüğü Hesabı ve Elektromanyetik Alan Ölçümleri*, Master’s Thesis, Istanbul University, 2021.
  35. Kılıçgedik, A., A. Adıgüzel, A. Çağlar, E. Çelebi, Ş. Esen, M. Kaya, Ü. Kaya, V. E. Özcan, G. Türemen, G. Ünel and F. Yaman, “Electromagnetic and Vacuum Tests of the PTAK-RFQ Module 0”, *In preparation*.
  36. Virtanen, P., R. Gommers, T. E. Oliphant, M. Haberland, T. Reddy, D. Cour-

- napeau, E. Burovski, P. Peterson, W. Weckesser, J. Bright, S. J. van der Walt, M. Brett, J. Wilson, K. J. Millman, N. Mayorov, A. R. J. Nelson, E. Jones, R. Kern, E. Larson, C. J. Carey, Í. Polat, Y. Feng, E. W. Moore, J. VanderPlas, D. Laxalde, J. Perktold, R. Cimrman, I. Henriksen, E. A. Quintero, C. R. Harris, A. M. Archibald, A. H. Ribeiro, F. Pedregosa, P. van Mulbregt and SciPy 1.0 Contributors, “SciPy 1.0: Fundamental Algorithms for Scientific Computing in Python”, *Nature Methods*, Vol. 17, pp. 261–272, 2020.
37. Rossum, G. V., *Python Tutorial*, Tech. Rep. CS-R9526, Centrum voor Wiskunde en Informatica (CWI), Amsterdam, May 1995.
38. Kim, J. K., W. M. Lee, P. Kim, M. Choi, K. Jung, S. Kim and S. H. Yun, “Fabrication and Operation of GRIN Probes for In Vivo Fluorescence Cellular Imaging of Internal Organs in Small Animals”, *Nature Protocols*, Vol. 7, No. 8, pp. 1456–1469, 2012.
39. Çelebi, E., A. Adıgüzel, B. Baran, A. Çağlar, O. Çakır, H. Çetinkaya, Ş. Esen, A. Karatay, Ü. Kaya, O. Koçer, S. Oğur, V. E. Özcan, G. Türemen, H. Ö. Yılmaz, F. Yaman and G. Ünel, “Design and Construction of a Proton Testbeam at KAHVELab”, *In preparation*.

## APPENDIX A: 20-NODE ISOPARAMETRIC BRICK INTERPOLATION FUNCTIONS

Here we present interpolation functions in the elements natural coordinates. The node numbers and their corresponding natural coordinates were listed in Table 2.1.

The equations defining interpolation functions can be expressed as:

$$\begin{aligned}
N_1 &= -\frac{1}{4} + \frac{1}{8}\eta + \frac{1}{8}\eta^2 + \frac{1}{8}\zeta - \frac{1}{8}\zeta\eta^2 + \frac{1}{8}\zeta^2 - \frac{1}{8}\zeta^2\eta + \frac{1}{8}\xi \\
&\quad - \frac{1}{8}\xi\eta^2 - \frac{1}{8}\xi\zeta\eta + \frac{1}{8}\xi\zeta\eta^2 - \frac{1}{8}\xi\zeta^2 + \frac{1}{8}\xi\zeta^2\eta + \frac{1}{8}\xi^2 - \frac{1}{8}\xi^2\eta - \frac{1}{8}\xi^2\zeta + \frac{1}{8}\xi^2\zeta\eta, \\
N_2 &= \frac{1}{4} - \frac{1}{4}\eta - \frac{1}{4}\zeta + \frac{1}{4}\zeta\eta - \frac{1}{4}\xi^2 + \frac{1}{4}\xi^2\eta + \frac{1}{4}\xi^2\zeta - \frac{1}{4}\xi^2\zeta\eta, \\
N_3 &= -\frac{1}{4} + \frac{1}{8}\eta + \frac{1}{8}\eta^2 + \frac{1}{8}\zeta - \frac{1}{8}\zeta\eta^2 + \frac{1}{8}\zeta^2 - \frac{1}{8}\zeta^2\eta \\
&\quad - \frac{1}{8}\xi + \frac{1}{8}\xi\eta^2 + \frac{1}{8}\xi\zeta\eta - \frac{1}{8}\xi\zeta\eta^2 + \frac{1}{8}\xi\zeta^2 - \frac{1}{8}\xi\zeta^2\eta + \frac{1}{8}\xi^2 - \frac{1}{8}\xi^2\eta - \frac{1}{8}\xi^2\zeta + \frac{1}{8}\xi^2\zeta\eta, \\
N_4 &= \frac{1}{4} - \frac{1}{4}\eta^2 - \frac{1}{4}\zeta + \frac{1}{4}\zeta\eta^2 - \frac{1}{4}\xi + \frac{1}{4}\xi\eta^2 + \frac{1}{4}\xi\zeta - \frac{1}{4}\xi\zeta\eta^2, \\
N_5 &= \frac{1}{4} - \frac{1}{4}\eta^2 - \frac{1}{4}\zeta + \frac{1}{4}\zeta\eta^2 + \frac{1}{4}\xi - \frac{1}{4}\xi\eta^2 - \frac{1}{4}\xi\zeta + \frac{1}{4}\xi\zeta\eta^2, \\
N_6 &= -\frac{1}{4} - \frac{1}{8}\eta + \frac{1}{8}\eta^2 + \frac{1}{8}\zeta - \frac{1}{8}\zeta\eta^2 + \frac{1}{8}\zeta^2 + \frac{1}{8}\zeta^2\eta \\
&\quad + \frac{1}{8}\xi - \frac{1}{8}\xi\eta^2 + \frac{1}{8}\xi\zeta\eta + \frac{1}{8}\xi\zeta\eta^2 - \frac{1}{8}\xi\zeta^2 - \frac{1}{8}\xi\zeta^2\eta + \frac{1}{8}\xi^2 + \frac{1}{8}\xi^2\eta - \frac{1}{8}\xi^2\zeta - \frac{1}{8}\xi^2\zeta\eta,
\end{aligned} \tag{A.1}$$

$$\begin{aligned}
N_7 &= \frac{1}{4} + \frac{1}{4}\eta - \frac{1}{4}\zeta - \frac{1}{4}\zeta\eta - \frac{1}{4}\xi^2 - \frac{1}{4}\xi^2\eta + \frac{1}{4}\xi^2\zeta + \frac{1}{4}\xi^2\zeta\eta, \\
N_8 &= -\frac{1}{4} - \frac{1}{8}\eta + \frac{1}{8}\eta^2 + \frac{1}{8}\zeta - \frac{1}{8}\zeta\eta^2 + \frac{1}{8}\zeta^2 + \frac{1}{8}\zeta^2\eta \\
&\quad - \frac{1}{8}\xi + \frac{1}{8}\xi\eta^2 - \frac{1}{8}\xi\zeta\eta - \frac{1}{8}\xi\zeta\eta^2 + \frac{1}{8}\xi\zeta^2 + \frac{1}{8}\xi\zeta^2\eta + \frac{1}{8}\xi^2 + \frac{1}{8}\xi^2\eta - \frac{1}{8}\xi^2\zeta - \frac{1}{8}\xi^2\zeta\eta, \\
N_9 &= \frac{1}{4} - \frac{1}{4}\eta - \frac{1}{4}\zeta^2 + \frac{1}{4}\zeta^2\eta - \frac{1}{4}\xi + \frac{1}{4}\xi\eta + \frac{1}{4}\xi\zeta^2 - \frac{1}{4}\xi\zeta^2\eta, \\
N_{10} &= \frac{1}{4} - \frac{1}{4}\eta - \frac{1}{4}\zeta^2 + \frac{1}{4}\zeta^2\eta + \frac{1}{4}\xi - \frac{1}{4}\xi\eta - \frac{1}{4}\xi\zeta^2 + \frac{1}{4}\xi\zeta^2\eta, \\
N_{11} &= \frac{1}{4} + \frac{1}{4}\eta - \frac{1}{4}\zeta^2 - \frac{1}{4}\zeta^2\eta - \frac{1}{4}\xi - \frac{1}{4}\xi\eta + \frac{1}{4}\xi\zeta^2 + \frac{1}{4}\xi\zeta^2\eta, \\
N_{12} &= \frac{1}{4} + \frac{1}{4}\eta - \frac{1}{4}\zeta^2 - \frac{1}{4}\zeta^2\eta + \frac{1}{4}\xi + \frac{1}{4}\xi\eta - \frac{1}{4}\xi\zeta^2 - \frac{1}{4}\xi\zeta^2\eta, \\
N_{13} &= -\frac{1}{4} + \frac{1}{8}\eta + \frac{1}{8}\eta^2 - \frac{1}{8}\zeta + \frac{1}{8}\zeta\eta^2 + \frac{1}{8}\zeta^2 - \frac{1}{8}\zeta^2\eta \\
&\quad + \frac{1}{8}\xi - \frac{1}{8}\xi\eta^2 + \frac{1}{8}\xi\zeta\eta - \frac{1}{8}\xi\zeta\eta^2 - \frac{1}{8}\xi\zeta^2 + \frac{1}{8}\xi\zeta^2\eta + \frac{1}{8}\xi^2 - \frac{1}{8}\xi^2\eta + \frac{1}{8}\xi^2\zeta - \frac{1}{8}\xi^2\zeta\eta, \\
N_{14} &= \frac{1}{4} - \frac{1}{4}\eta + \frac{1}{4}\zeta - \frac{1}{4}\zeta\eta - \frac{1}{4}\xi^2 + \frac{1}{4}\xi^2\eta - \frac{1}{4}\xi^2\zeta + \frac{1}{4}\xi^2\zeta\eta, \\
N_{15} &= -\frac{1}{4} + \frac{1}{8}\eta + \frac{1}{8}\eta^2 - \frac{1}{8}\zeta + \frac{1}{8}\zeta\eta^2 + \frac{1}{8}\zeta^2 - \frac{1}{8}\zeta^2\eta \\
&\quad - \frac{1}{8}\xi + \frac{1}{8}\xi\eta^2 - \frac{1}{8}\xi\zeta\eta + \frac{1}{8}\xi\zeta\eta^2 + \frac{1}{8}\xi\zeta^2 - \frac{1}{8}\xi\zeta^2\eta + \frac{1}{8}\xi^2 - \frac{1}{8}\xi^2\eta + \frac{1}{8}\xi^2\zeta - \frac{1}{8}\xi^2\zeta\eta, \\
N_{16} &= \frac{1}{4} - \frac{1}{4}\eta^2 + \frac{1}{4}\zeta - \frac{1}{4}\zeta\eta^2 - \frac{1}{4}\xi + \frac{1}{4}\xi\eta^2 - \frac{1}{4}\xi\zeta + \frac{1}{4}\xi\zeta\eta^2, \\
N_{17} &= \frac{1}{4} - \frac{1}{4}\eta^2 + \frac{1}{4}\zeta - \frac{1}{4}\zeta\eta^2 + \frac{1}{4}\xi - \frac{1}{4}\xi\eta^2 + \frac{1}{4}\xi\zeta - \frac{1}{4}\xi\zeta\eta^2, \\
N_{18} &= -\frac{1}{4} - \frac{1}{8}\eta + \frac{1}{8}\eta^2 - \frac{1}{8}\zeta + \frac{1}{8}\zeta\eta^2 + \frac{1}{8}\zeta^2 + \frac{1}{8}\zeta^2\eta \\
&\quad + \frac{1}{8}\xi - \frac{1}{8}\xi\eta^2 - \frac{1}{8}\xi\zeta\eta - \frac{1}{8}\xi\zeta\eta^2 - \frac{1}{8}\xi\zeta^2 - \frac{1}{8}\xi\zeta^2\eta + \frac{1}{8}\xi^2 + \frac{1}{8}\xi^2\eta + \frac{1}{8}\xi^2\zeta + \frac{1}{8}\xi^2\zeta\eta, \\
N_{19} &= \frac{1}{4} + \frac{1}{4}\eta + \frac{1}{4}\zeta + \frac{1}{4}\zeta\eta - \frac{1}{4}\xi^2 - \frac{1}{4}\xi^2\eta - \frac{1}{4}\xi^2\zeta - \frac{1}{4}\xi^2\zeta\eta, \\
N_{20} &= -\frac{1}{4} - \frac{1}{8}\eta + \frac{1}{8}\eta^2 - \frac{1}{8}\zeta + \frac{1}{8}\zeta\eta^2 + \frac{1}{8}\zeta^2 + \frac{1}{8}\zeta^2\eta \\
&\quad - \frac{1}{8}\xi + \frac{1}{8}\xi\eta^2 + \frac{1}{8}\xi\zeta\eta + \frac{1}{8}\xi\zeta\eta^2 + \frac{1}{8}\xi\zeta^2 + \frac{1}{8}\xi\zeta^2\eta + \frac{1}{8}\xi^2 + \frac{1}{8}\xi^2\eta + \frac{1}{8}\xi^2\zeta + \frac{1}{8}\xi^2\zeta\eta.
\end{aligned} \tag{A.2}$$

## **APPENDIX A: PERMISSION OF FIGURES**

Figure 4.1 and 4.2 are used by the kind permission of Aytül Adigüzel. The other images produced as part of this thesis and transferred to the publishing house's copyright have been used in the thesis book in compliance with the publishing policy regarding the reuse of the author's self-created writings and graphics, as outlined on the publisher's website.